# Stony Brook University

**Wind-driven dispersion, residence time and connectivity of Great South Bay**

A Dissertation Presented

by

**Dongming Yang**

to

The Graduate School

in Partial fulfillment of the

Requirements

for the Degree of

**Doctor of Philosophy**

in

**Marine and Atmospheric Sciences**

Stony Brook University

**December 2014**

**Stony Brook University**
The Graduate School

**Dongming Yang**

We, the dissertation committee for the above candidate for the
Doctor of Philosophy degree, hereby recommend
acceptance of this dissertation.

**Robert E. Wilson – Dissertation Advisor**
**Associate Professor, School of Marine and Atmospheric Sciences, Stony Brook University**

**Sultan Hameed - Chairperson of Defense**
**Professor, School of Marine and Atmospheric Sciences, Stony Brook University**

**Charles N. Flagg, Research Professor**
**School of Marine and Atmospheric Sciences, Stony Brook University**

**Robert J. Chant, Professor**
**Institute of Marine and Coastal Sciences, Rutgers University**

**Keith R. Thompson, Professor**
**Department of Oceanography, Dalhousie University**

**Stephan B. Munch, Associate Professor**
**Southwest Fisheries Science Center, National Marine Fisheries Service**

Charles Taber
Dean of the Graduate School

Abstract of the Dissertation

**Wind-driven dispersion, residence time and connectivity of Great South Bay**

by

**Dongming Yang**

**Doctor of Philosophy**

in

**Marine and Atmospheric Sciences**

Stony Brook University

**2014**

Horizontal dispersion process, which is controlled by current shears, determines the residence time and inner connectivity in coastal lagoons. Great South Bay (GSB), NY is a shallow coastal lagoon which has long suffered from eutrophication and harmful algal blooms and is presently the focus of an intensive ecosystem based management study including the development of an ecological model. Current and water level observations and hindcast simulations using a three-dimensional hydrodynamic model were used to examine the structure of tidal and wind-driven circulation in GSB, and the influence of this structure on horizontal dispersion. Results confirm that circulation in the interior of GSB is primarily wind-driven. Momentum diagnostics contribute to our understanding of

dynamics controlling the longitudinal and lateral circulation. At synoptic periods, the longitudinal momentum balance involves primarily barotropic pressure gradient and stress divergence; baroclinic pressure gradient and Coriolis force also contribute to the lateral momentum balance. Observations indicate that vertical structures of both longitudinal and lateral currents are consistent with simple model involving surface and bottom log layers and a linear stress profile within the interior of the water column. Longitudinal currents are highly sheared laterally, with maximum shear occurring over strong bottom slopes between the channel and shoals. Lateral currents are less organized and have direction reversed over small distance along lagoon axial. Lagrangian particle tracking algorithm was implemented based on current field from the hydrodynamic model to quantify the horizontal shear dispersion, residence times, and inner-lagoon connectivity within GSB. The largest longitudinal dispersion rate was over 60 $m^2/s$ and was associated with the interaction of laterally-sheared longitudinal currents and lateral mixing; lateral dispersion ranged from 0.1 to 1 $m^2/s$ and was mainly explained by the longitudinal shear dispersion. For dispersion in both horizontal directions, oscillatory and steady flows made comparable contribution. Results emphasize the influence of synoptic period wind forcing on the interior connectivity pattern in GSB.

# Table of Contents

List of Figures ..... vii

List of Tables ..... xiii

Chapter 1 Introduction ..... 1

1.1 Background ..... 1

1.2 Great South Bay hydrography ..... 4

1.3 Previous studies of physical oceanography of GSB ..... 6

1.4 Recent survey of vertical structure of currents in GSB ..... 7

Chapter 2 Numerical Model Description and Validation ..... 13

2.1 Description of Numerical Model Configuration ..... 13

2.2 FVCOM model initial condition and forcing ..... 16

2.3 FVCOM model validation ..... 20

2.4 Lagrangian particle tracking algorithm ..... 27

Chapter 3 Circulation Structure in GSB ..... 29

3.1 Wind-driven longitudinal circulation in central GSB ..... 30

3.2 Wind-driven lateral circulation in central GSB ..... 50

3.3 Vorticity analysis of residual circulation in GSB ..... 59

3.4 Summary ..... 70

Chapter 4 Horizontal Dispersion in Central GSB ..... 72

4.1 Particle experiments ..... 72

4.2 Quantification of particle patches dilution and spreading ..... 79

4.3 Analysis of the longitudinal dispersion rates ..... 87

4.4 Analysis of the lateral dispersion rates .....95
4.5 Summary .....99
Chapter 5 Residence time and inner-lagoon connectivity .....101
5.1 Residence time pattern of central GSB.....101
5.2 Connectivity within central GSB.....105
5.3 Summary .....114
Future Works.....116
References .....118

# List of Figures

Figure 1.1 Research area (from Google Map) .....5
Figure 1.2 Velocity record obtained from GSB#1 ADCP in July, 2012 .....7
Figure 1.3 Residual currents calculated from GSB#1 ADCP record in July, 2012 ..8
Figure 1.4 Low-pass filtered ADCP current velocities in July, 2012.....10
Figure 1.5 First and second principal components of low-pass filtered currents....10
Figure 1.6 Cross correlation between wind vector and first/second principal components .....11
Figure 1.7 First and second modes of low-pass filtered currents .....11
Figure 1.8 M2 tidal ellipses estimated from the ADCP currents.....12
Figure 2.1 Model grids setup and open boundary locations for Great South Bay ..15
Figure 2.2 FVCOM model bathymetry (mean water level) for Great South Bay ...15
Figure 2.3 FVCOM temperature (upper) and salinity (lower) initial condition.....17
Figure 2.4 Model simulated sea level elevation on open boundary nodes .....18
Figure 2.5 FVCOM river and outfalls discharge .....19
Figure 2.6 FVCOM model wind velocity (upper: east component; lower: north component).....20
Figure 2.7 SeaCat observation and USGS sites.....22
Figure 2.8 $M_2$ tidal ellipses of FVCOM model currents near the buoy and ADCP observation .....24

Figure 2.9 First (left) and second (right) modes of low-pass filtered model currents .....25
Figure 2.10 First principal components of low-pass filtered model and observation currents.....26
Figure 2.11 principal components of low-pass filtered model and observation currents.....26
Figure 2.12 Cross correlation between wind speed and first (left)/second (right) principal components of model currents.....26
Figure 3.1 Great South Bay Bathymetry and Section Locations.....32
Figure 3.2 Bathymetry of Section 1 and Stations Locations .....32
Figure 3.3 Time series of longitudinal momentum terms at station7 (upper), station 15 (middle) at section 1, and longitudinal wind speed (lower) .....33
Figure 3.4 Bathymetry of Section 2 and Station Locations.....35
Figure 3.5 Time series of longitudinal momentum terms at station7 (upper), station 15 (lower) at section 2.....36
Figure 3.6 Sea level elevation in central GSB (upper), longitudinal current velocity on section 1 (middle) and 2 (lower) at Hour 475.....41
Figure 3.7 Sea level elevation in central GSB (upper), longitudinal current velocity on section 1 (middle) and 2 (lower) at Hour 620.....43

Figure 3.8 Vertical structures of longitudinal current velocity at station 7, 16 on section 1 (a, b) and station 7 16 on section 2 (c, d) .....46
Figure 3.9 Horizontal structure of depth-averaged longitudinal velocity under westward (upper) and eastward (lower) wind forcing .....49
Figure 3.10 Horizontal structure of depth-averaged longitudinal velocity at slack wind time after eastward (upper) and westward (lower) winds .....50
Figure 3.11 Wind speed in lateral direction.....52
Figure 3.12 Time series of lateral momentum terms at station7 (upper), station 15 (lower) of section 1 .....53
Figure 3.13 series of lateral momentum terms at station7 (upper), station 15 (lower) of section 2 .....54
Figure 3.14 Lateral current velocity on section 1 (upper) and 2 (lower) at Hour 463 .....57
Figure 3.15 Lateral current velocity on section 1 (upper) and 2 (lower) at Hour 581 .....58
Figure 3.16 Horizontal structure of depth-averaged lateral velocity under northward (upper) and southward (lower) wind forcing .....59
Figure 3.17 Depth-averaged circulation (upper) during westward wind event and the vorticity (lower) .....62

Figure 3.18 Vorticity tendency generated by baroclinicity, surface wind stress, bottom stress, and total effects of the 3 terms during a westward wind event .....63
Figure 3.19 Depth-averaged circulation (upper) during eastward wind event and the vorticity (lower) .....65
Figure 3.20 Vorticity tendency generated by baroclinicity, surface wind stress, bottom stress, and total effects of the 3 terms during an eastward wind event .....66
Figure 3.21 Depth-averaged circulation (upper) during hour 437 to 648 .....68
Figure 3.22 Vorticity tendency generated by baroclinicity, surface wind stress, bottom stress, and total effects of the 3 terms during hour 437 to 648 .....70
Figure 4.1 Releasing locations of particle patches .....72
Figure 4.2 Spreading of particle patch #1.....75
Figure 4.3 Spreading of particle patch #2.....76
Figure 4.4 Spreading of particle patch #3.....76
Figure 4.5 Spreading of particle patch #4.....78
Figure 4.6 mean concentration (%) of all 4 patches as a function of time after release (start at 2 hours after release).....81
Figure 4.7 moment in lateral direction of the patches .....84
Figure 4.8 2nd moment in longitudinal direction of the patches.....86
Figure 4.9 Locations of stations.....88

Figure 4.10 Time series of vertical shear dispersion in longitudinal direction at locations 1 – 4 .....90
Figure 4.11 of oscillatory to steady lateral shear dispersion with the same shear magnitude.....93
Figure 4.12 series of vertical shear dispersion in lateral direction at locations 1 – 4 .....97
Figure 4.13 Section on which the longitudinal shear dispersion was calculated ....99
Figure 5.1 Initial positions of Lagrangian particles.....101
Figure 5.2 Residence time in central GSB (hours) .....102
Figure 5.3 Trajectories of Lagrangian particles.....103
Figure 5.4 Residence time (hours) in compartments of central GSB under tidal and realistic wind forcing .....104
Figure 5.5 time (hours) in compartments of central GSB under tidal forcing only .....105
Figure 5.6 Transition probabilities of tide-only Lagrangian particle simulation ..107
Figure 5.7 Transition probabilities of wind-driven Lagrangian particle simulation .....112
Figure 5.8 component of wind velocity during Lagrangian particle simulation ...112
Figure 5.9 Spectrum of the east component of FVCOM wind velocity.....113

Figure 5.10 Transition probabilities of wind-driven Lagrangian particle simulation (8-day time interval).....114

# List of Tables

Table 2.1 FVCOM model freshwater sources .....19

Table 2.2 Comparison of tidal constituents from FVCOM with observations.....23

Table 5.1 Transition probability (%) matrix for the tide-only Lagrangian particle simulation (indices on the rows are for original compartments and ones on the columns are for receiving compartments, compartment 9 represents the outer box where, by assumption, particles do not leave after entering) .....108

Table 5.2 Flushing time (first passage time to the ocean) in days.....109

Table 5.3 Uncertainty (%) matrix of transition probability for the tide-only Lagrangian particle simulation .....110

# Chapter 1 Introduction

## 1.1 Background

Eutrophication in coastal lagoons is caused by anthropogenic nutrient loading including discharges from water pollution control plants and riverine inputs. The efficiency of flushing in a coastal lagoon, which could be measured by residence time, controls the retainability of the nutrients, and thus eutrophication. On the other hand, larval connectivity within coastal lagoons is essential to the understanding of the population dynamics (Luettich, et. al., 1999; Cowen, et. al., 2006; Siegel, et. al., 2008). Residence time and inner-lagoon connectivity are both controlled by horizontal dispersion.

The effective horizontal dispersion coefficient in coastal lagoons/estuaries could reach the value of 100-1000 $m^2/s$ or even larger (Bowden, 1965; Zimmerman, 1986; Geyer, Chant, and Houghton, 2008), and it has been a useful topic to study mechanisms contributing to such high values. Taylor (1953) brought the concept of shear dispersion, which states that the shear in currents and the diffusion in the direction of shear give rise to an effective dispersion in the current direction. Bowden (1965) applied this concept to the ocean, and derived the horizontal dispersion induced by vertical shear for a steady state:

$$K_x = -\frac{1}{H}\int_0^H u'(z)\int_0^z \frac{1}{K_z(z)}\int_0^z u'(z)dzdzdz \quad (1.1)$$

where H is depth of the water column, u' is deviation from the depth-averaged along channel current velocity, and $K_z$ is vertical eddy viscosity. Okubo (1968) also visited shear dispersion in both vertical and lateral direction, where he assumed linear shear for both direction, and explained the shape evolution of a dye patch in unbounded and bounded seas.

In estuaries and coastal waters, the horizontal dispersion is also produced by oscillatory flows such as tidal currents and wind-driven currents. Bowden (1965) pointed out that, when the vertical mixing time is much shorter than the tidal period, i.e. $\frac{TK_z}{H^2}$ (T is the tidal period) is much bigger than 1, the effective horizontal dispersion associated with tidal current has half the size of the one with steady flow, if the amplitude of the tidal current is equal to the steady flow velocity. Zimmerman (1986) analyzed the oscillatory flows with both linear and sinusoidal profile in the vertical direction, and obtained the asymptotic behavior of the ratio between tidal current and steady flow shear dispersion: the ratio approaches 0.5 with $\frac{TK_z}{H^2}$.

Bowden (1965) also suggested that in estuaries and coastal seas, the overall horizontal dispersion was about a factor of 2 larger than the vertical shear dispersion, and the difference was primarily due to lateral shears. In his review paper, Zimmerman (1986) proposed a cascade shear-dispersion model, in which turbulence interact with vertical shear, and then with horizontal shear to produce an effective horizontal dispersion coefficient big enough to explain mixing process in many observations. In a recent dye experiment in Hudson River, Geyer, Chant and Houghton (2008) did a quantitative assessment of horizontal dispersion, in which they also emphasized the importance of both vertical and lateral shear in currents, and suggested equation (1.1) could be utilized to estimate the lateral shear dispersion, by replacing the water column depth H and vertical dispersion rate $K_z$ with width of the dye patch W and lateral dispersion rate $K_y$.

Based on the above discussion, knowledge of current structure, especially the lateral/vertical shears, is essential to understand the horizontal mixing in coastal waters. Signell et al. (1990) and Glorioso and Davies (1995) both emphasized the importance of bottom slope to the development of lateral shear for wind driven motion in a shallow basin; Winant (2004) determined that for low Ekman number (E) the axial flow was primarily laterally sheared while as E increased vertical shear developed; Jia and Li (2012) used both E and Wedderburn number (W, relative magnitude of wind driven and density driven current) to

explained the vertical/lateral shear of wind driven flow in a shallow lagoonal estuary with strong horizontal density gradients. As the research area of this work, Great South Bay (GSB) is different with conditions in the above studies: it is extremely shallow and characterized by low horizontal gradients and velocities, and we estimated that E and W to be of the order of 10 and 50, compared with 1 and 5 in Jia and Li (2012). So we expect a non-rotation homogeneous framework discussed by Mathieu et. al. (2002) in which the primary force balance is between barotropic pressure gradient and stress divergence is more relevant for GSB.

In this research, the results from numerical simulation (described in Chapter 2) has been used to analyze mechanisms controlling flow structures in GSB and to quantify the strength of lateral and vertical current shears (Chapter 3); based on the knowledge of circulation structure, the horizontal dispersion rates were analyzed quantitatively for particle tracking experiments in Chapter 4; as practical applications, distribution of residence time in GSB and connectivity among lagoon compartments were discussed in Chapter 5.

## 1.2 Great South Bay hydrography

GSB represents a series of interconnecting and very shallow coastal lagoons along the south shore of Long Island. The total length of this lagoon system is approximately 120 km and the maximum width is less than 10 km; the average

mean low water depth is approximately 2 m. The research area (Figure 1.1) consists of Hempstead Bay, South Oyster Bay, the main central Great South Bay, and Moriches Bay from west to east. The morphology of the western bays is complicated by a dendritic marsh network.

Figure 1.1 Research area (from Google Map)

GSB is a region where salt and fresh water mix. It is typical of a choked lagoon (Kjerfve and Magill, 1989) with weak tidal forcing; it communicates with the Atlantic through four relatively narrow tidal inlets: Rockway Inlet, Jones Inlet, Fire Island Inlet, and Moriches Inlet from west to east. M2 is the dominant tidal constituent in GSB, whose amplitude, however, experienced a significant reduction in the interior of the bay. GSB receives fresh water from rivers, ground water inflow and direct rainfall. Daily stream flow gauges maintained by USGS (http://nwis.waterdata.usgs.gov/nwis/sw) at 18 locations throughout the bay, including two major rivers (Carmens and Connetquot) and other small rivers and creeks, give an estimated river input rate of approximately 6.2 $m^3/s$. It should be

noted that these stations do not cover all the river discharge sites so the real river input rate is higher.

## 1.3 Previous studies of physical oceanography of GSB

Wong (1986, 1993) and Wong and Wilson (1984) described the characteristics of water level and current fluctuations within the main part of GSB and the exchange between the lagoon and coastal ocean at both tidal and sub-tidal frequencies in light of extensive observations. They discussed that diurnal and semi-diurnal tidal fluctuations attenuated very rapidly proceeding through the inlets into the interior of the lagoon. At all stations in the interior the variance at tidal frequencies was less than 20% than that for stations on the coast, and the total variance a sub-tidal frequencies, primarily at synoptic periods, exceeded the variance at tidal periods. These analyses also emphasized that the sub-tidal sea level fluctuations within the lagoon were forced by along-shore winds (along 250-070 ° T) with a simultaneous inflow or outflow through the ends of the lagoon in response to the rise of fall of coastal sea level. A secondary mode of response was a through-flow mode associated with a set-up response in the lagoon associated with local forcing on the lagoon again by along-shore/along-lagoon winds.

## 1.4 Recent survey of vertical structure of currents in GSB

As demonstrated by Bowden (1965) and Zimmerman (1986), discerning contribution from flows with different time scales is important for evaluating the magnitude of the shear dispersion as its magnitude changes with the time scale even strength of the flow keeps the same. Based on a record of flow profile during July, 2012 (Figure 1.2) from our ADCP near the GSB#1 buoy, we estimated the magnitudes of residual current, wind-driven flow and tidal current as functions of depth.

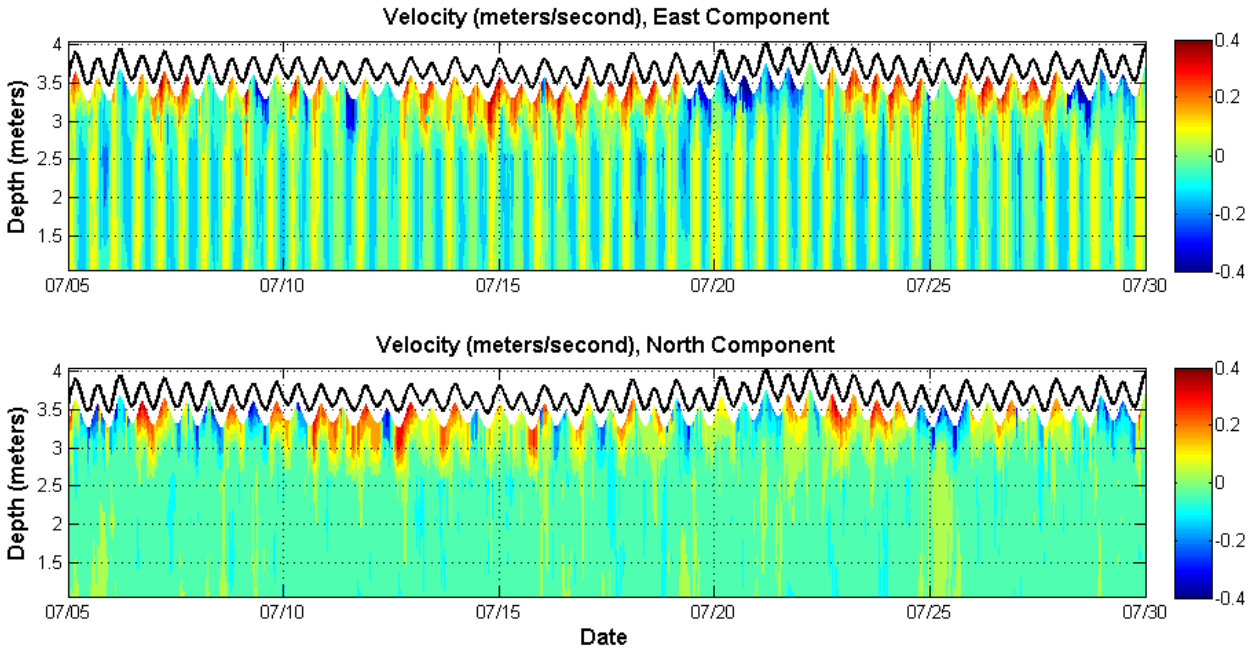


Figure 1.2 Velocity record obtained from GSB#1 ADCP in July, 2012

The residual currents in east and north directions are estimated by taking the time-average for the record, and their vertical profiles are shown in Figure 1.3. The residual current profiles in both directions show strong surface shears among the

topmost 3 bins, and almost uniform magnitudes among the other bins below. In the top 1 meter represented by the topmost 3 bins, the vertical shears are about 0.07 $sec^{-1}$ and 0.05 $sec^{-1}$ for east and north directions separately.

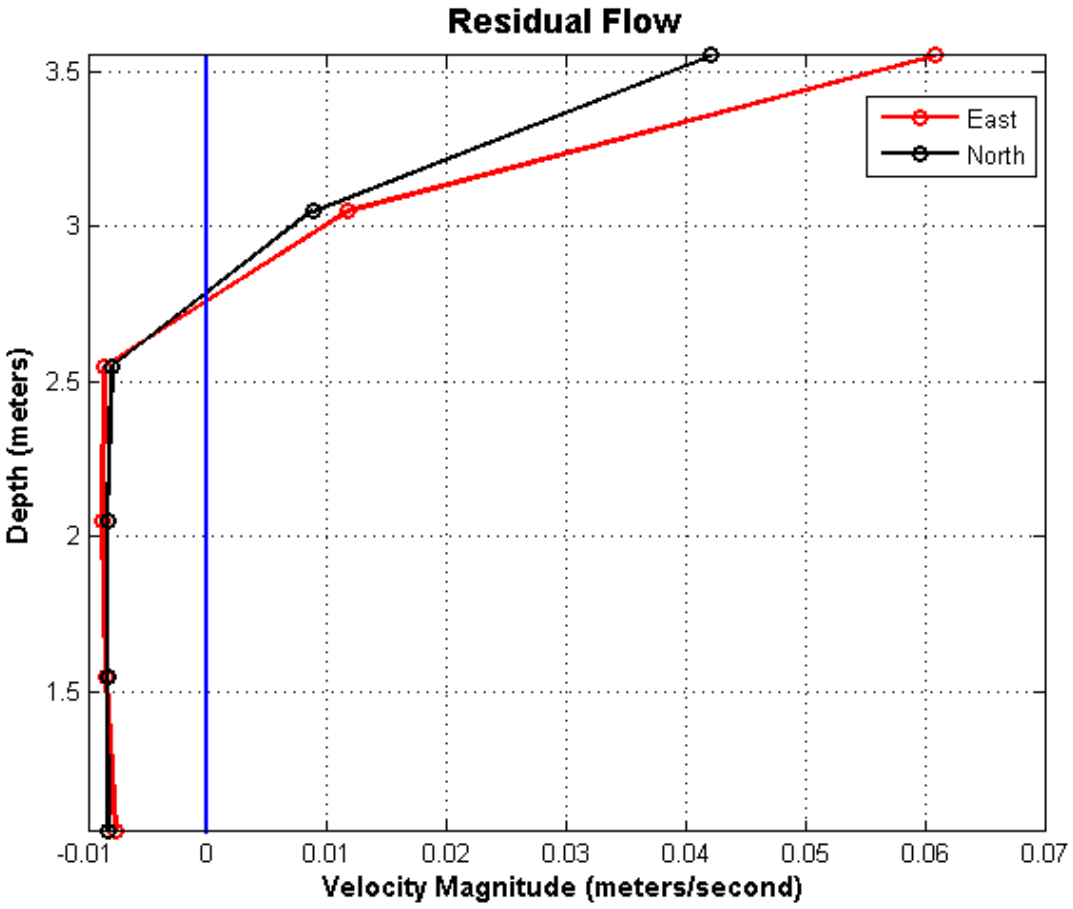


Figure 1.3 Residual currents calculated from GSB#1 ADCP record in July, 2012

The direction and magnitude of wind-driven flows in GSB are controlled by the synoptic winds with periods from 2-7 days. So to gain an insight of the characteristic vertical profile of the currents forced by wind, we firstly removed the tidal signals from the currents record by applying a low-pass filter (Figure 1.4) and then conducted an EOF analysis on the filtered velocity data (synoptic time scale).

The results show that the first and second modes of EOF account for over 96% of the total variance in the synoptic currents; the first/second principal component is highly correlated with the east-west/north-south wind vector (Figure 1.5 and 1.6). Based on the above information, the character profiles of wind-driven currents in both modes are then constructed by multiplying the eigenvectors of the first and second modes by the standard deviation of the principal components (Figure 1.7). Both modes show strong surface shears. In the first mode, surface current flows towards northeast; the velocity gradients within the top 1 meter are 0.17 $sec^{-1}$ in the east component and 0.07 $sec^{-1}$ in the north component; the currents shear below are weak, and the current turns to the southwest. In the second mode, the surface current flows to the northwest; the current shears within the surface layer are 0.04 $sec^{-1}$ in the east component and 0.11 $sec^{-1}$ in the north component; below the surface layer, the current turns very slowly towards south.

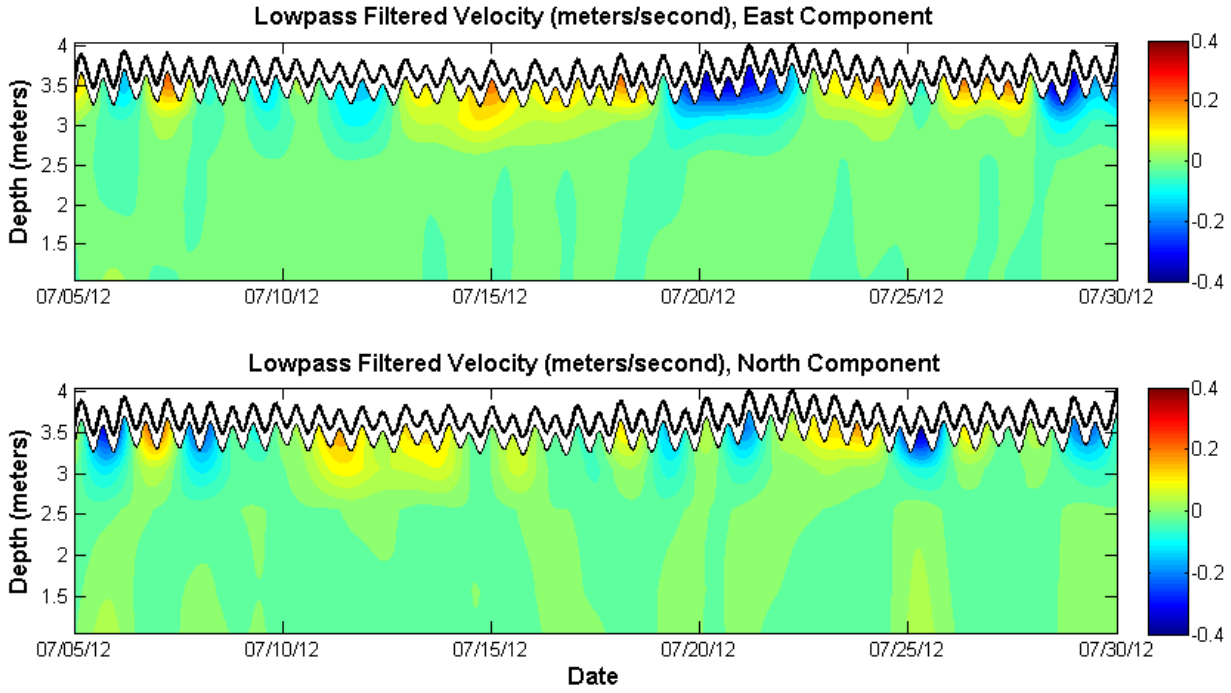


Figure 1.4 Low-pass filtered ADCP current velocities in July, 2012

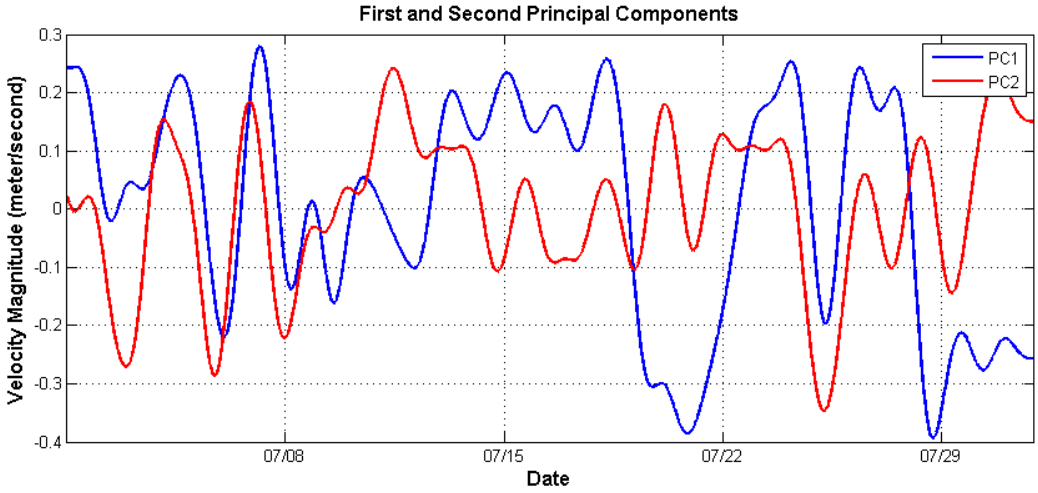


Figure 1.5 First and second principal components of low-pass filtered currents

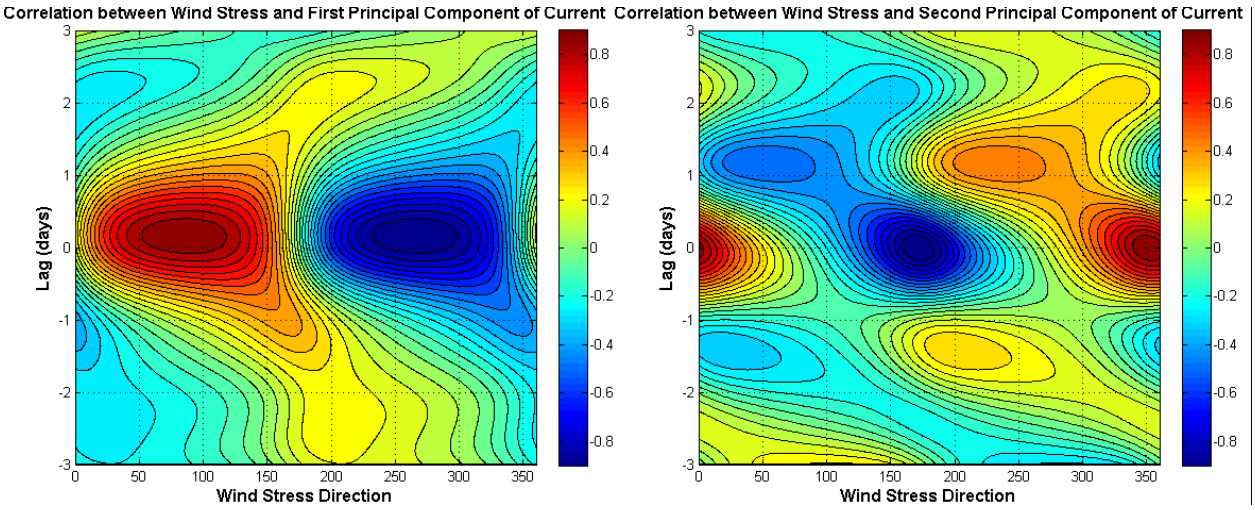


Figure 1.6 Cross correlation between wind vector and first/second principal components

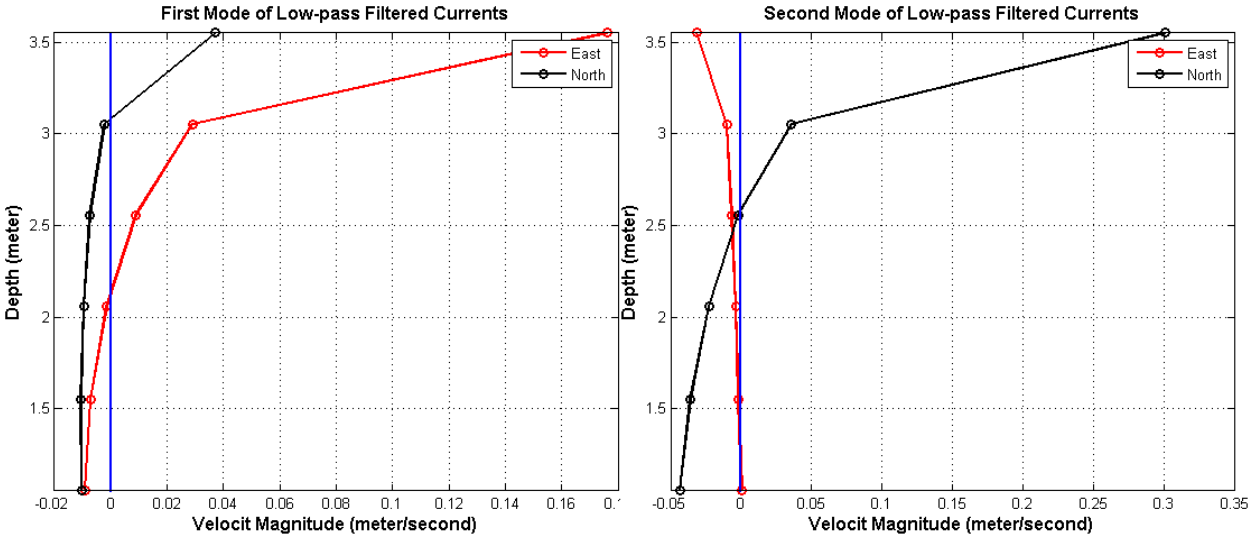


Figure 1.7 First and second modes of low-pass filtered currents

The dominant tidal constituent in GSB is M2 (Wong and Wilson, 1984), so to analyze the tidal currents, harmonic analysis is applied on to the current record, and tidal ellipses of M2 tide in each of the 6 bins (from bottom to the surface) are shown in Figure 1.8. In the 4 bins below the depth of 2.6 m (Figure 1.7), the ellipses are linearized and the inclined in the orientation of GSB; the tidal amplitude increases when it goes up to the surface, but the gradient is small. In bin

5 and bin 6, where there is not constraint of the bathymetry, the tidal ellipses tend to be more circular, the amplitude in the east-west direction is reduced, and the inclination is more east-westward instead of direction of GSB's axis.

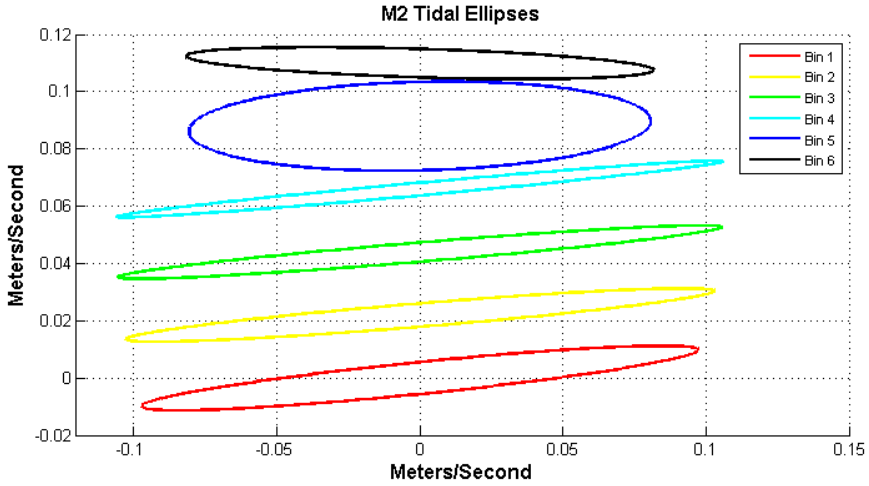


Figure 1.8 M2 tidal ellipses estimated from the ADCP currents

# Chapter 2 Numerical Model Description and Validation

## 2.1 Description of Numerical Model Configuration

The hydrodynamic numerical model used for this study is Finite Volume Coastal Ocean Model (FVCOM). FVCOM is a 3-D unstructured-grid, free-surface, primitive equation ocean model (Chen et al, 2003), which discretizes the integral form of the conservation equations within volume elements; the unstructured, arbitrary triangular grids formation allows more realistic model domain fitting to the complicated geometry of the research region. The model domain, which extends from Sandy Hook in the west to Montauk Point in the east, and offshore to approximately to the edge of the continental shelf, is shown in Figure 2.1. The grid contains 72,666 nodes and 131,434 triangular elements (Figure 2.1, elements in the lagoon are hard to discern because of the small size); horizontal resolution of element area ranges approximately from 20.3 $m^2$ in the lagoon to $31.6 \times 10^6$ $m^2$ in the coastal ocean, and 5 sigma layers are placed in the vertical. Model bathymetry was interpolated onto the grid (Figure 2.2) from a combination of NOS survey data and multi-beam data collected by Roger Flood. Some bathymetric smoothing and deepening were made to insure the model stability.

FVCOM uses a split-explicit time-stepping scheme; the time step used for this study was 0.5589 seconds for the external mode and 2.7946 seconds for the

internal mode. A second-order accurate, four-stage Runge-Kutta time stepping scheme is used for external, vertical-averaged mode; a second-order accurate upwind scheme is used for flux calculation of momentum and tracer quantities in internal mode. The horizontal diffusion coefficient was calculated by the Smagorinsky eddy parameterization method, which is proportional to the grid spacing. The vertical eddy viscosity was calculated by the Mellor and Yamada level 2.5 turbulent closure model. A logarithmic formulation for the bottom stress was used with $z_0$ ranging from 0.01 m to 0.015 m.

The model was started from rest with initial temperature and salinity field derived from observation. The open boundary condition was specified by sea surface elevation calculated based on amplitudes and phases of major tidal constituents. These data were ramped during the first 30 hours of the simulation. Temperature and salinity at the open boundary were kept constant during the simulation.

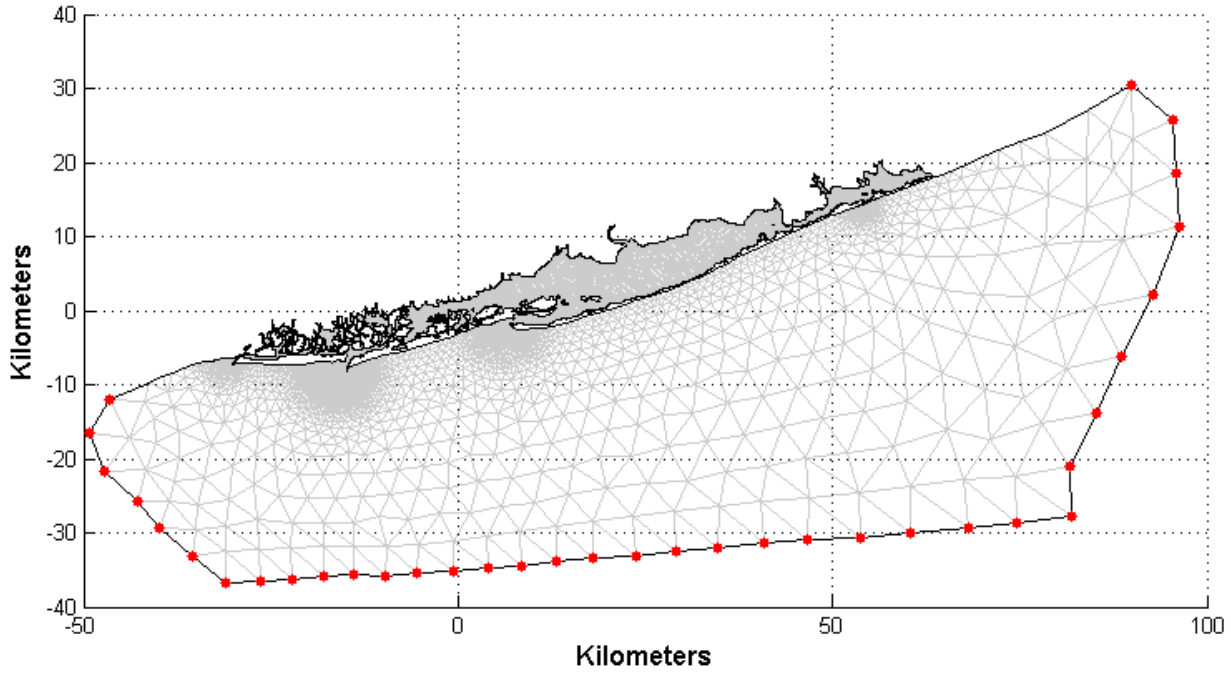


Figure 2.1 Model grids setup and open boundary locations for Great South Bay

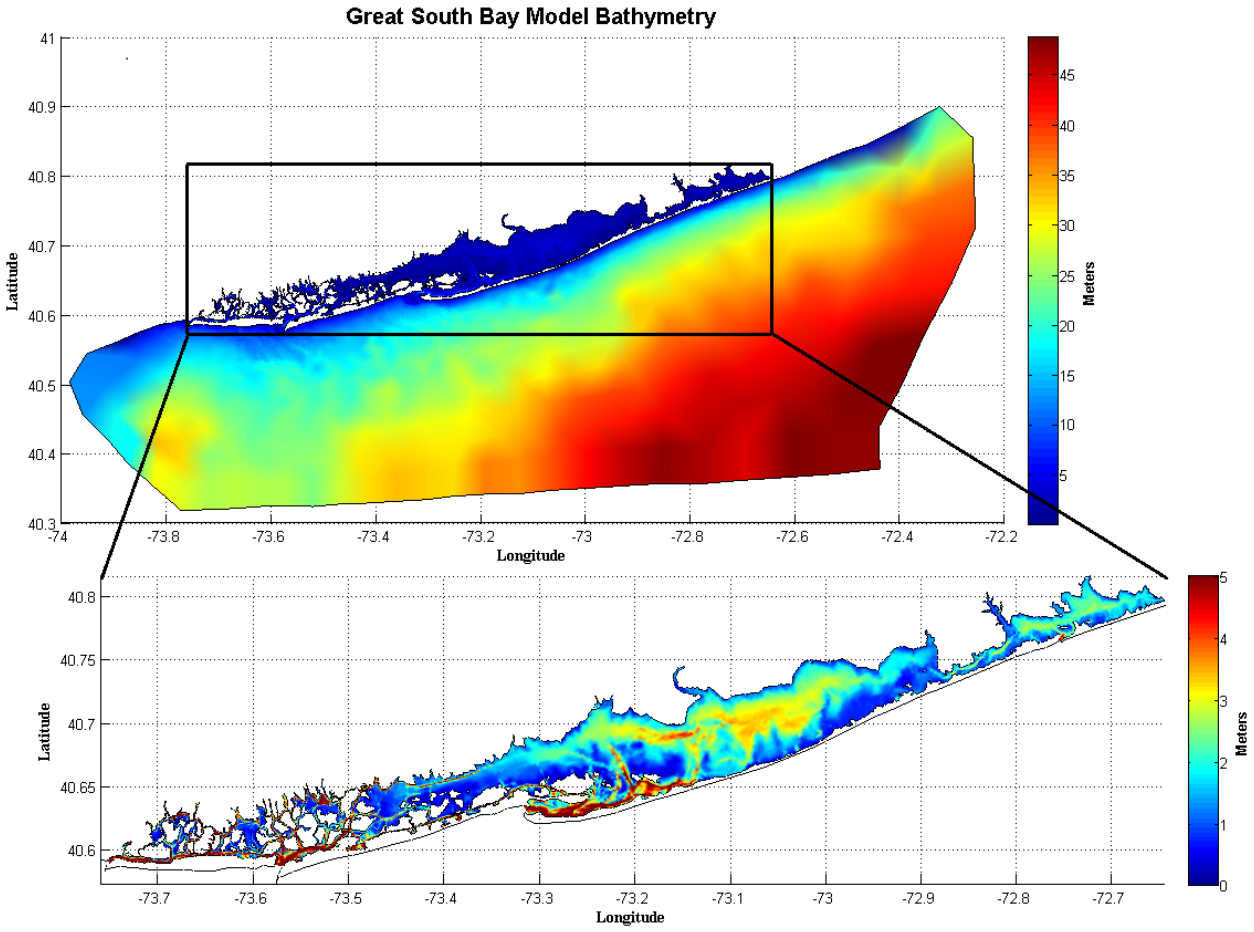


Figure 2.2 FVCOM model bathymetry (mean water level) for Great South Bay

## 2.2 FVCOM model initial condition and forcing

Initial temperatures and salinities were derived from the Suffolk County DEC observations at 21 stations in the Great South Bay and Moriches Bay. The data for these stations were simply averaged to produce climatological mean conditions. We do not have similar observations from Nassau County and so estimates of initial there were subjectively extrapolated from the Suffolk County data. In the offshore region outside the inlets the salinity and temperature were assumed uniform and set to 15.5$^{o}$C and 31.5psu approximating the mean climatological conditions just outside Fire Island Inlet which was the only coastal location with long-term observations.

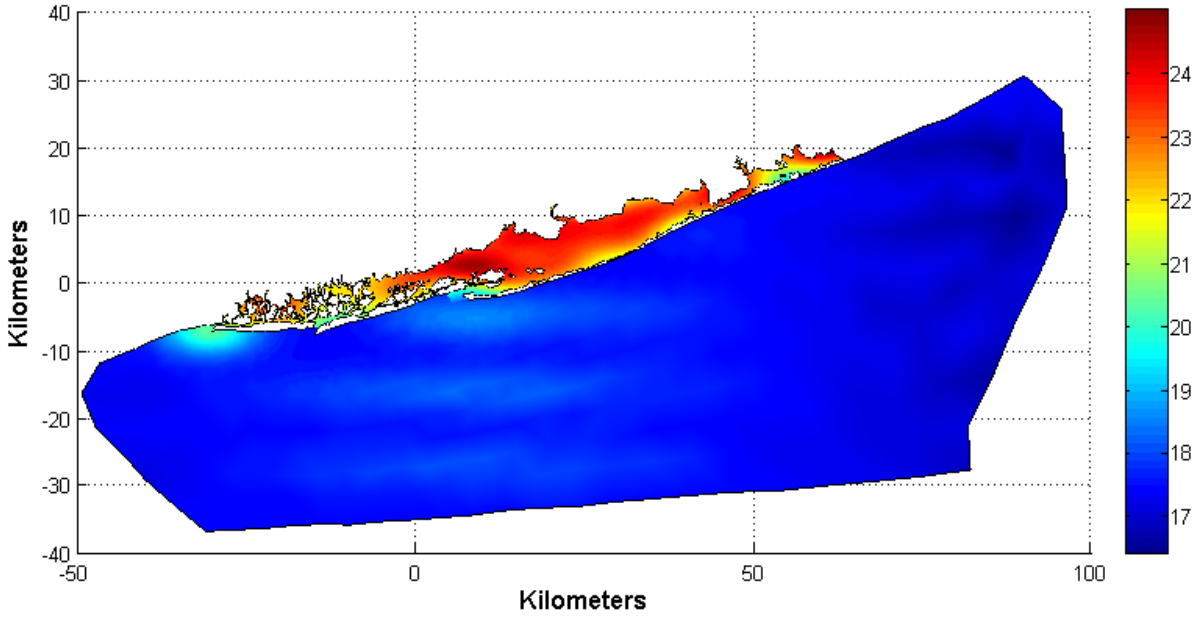

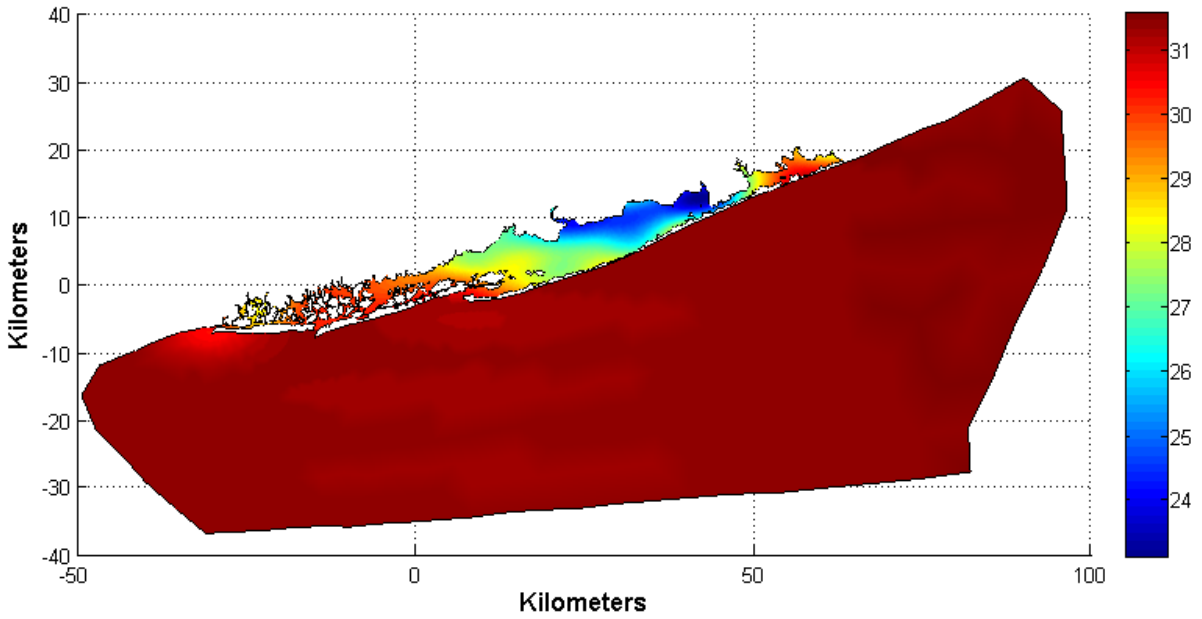


Figure 2.3 FVCOM temperature (upper) and salinity (lower) initial condition

The sea-surface elevation of the model was forced by specifying the amplitude and GMT phase for tidal constituents on the open ocean boundary nodes (Figure 2.1). Five major constituents were used: $M_2$, $S_2$, $N_2$, $K_1$, and $O_1$. Open boundary constituents were extracted from the Oregon State global tidal model (http://volkov.oce.orst.edu/tides), and the simulated elevation on multiple nodes were shown in Figure 2.4.

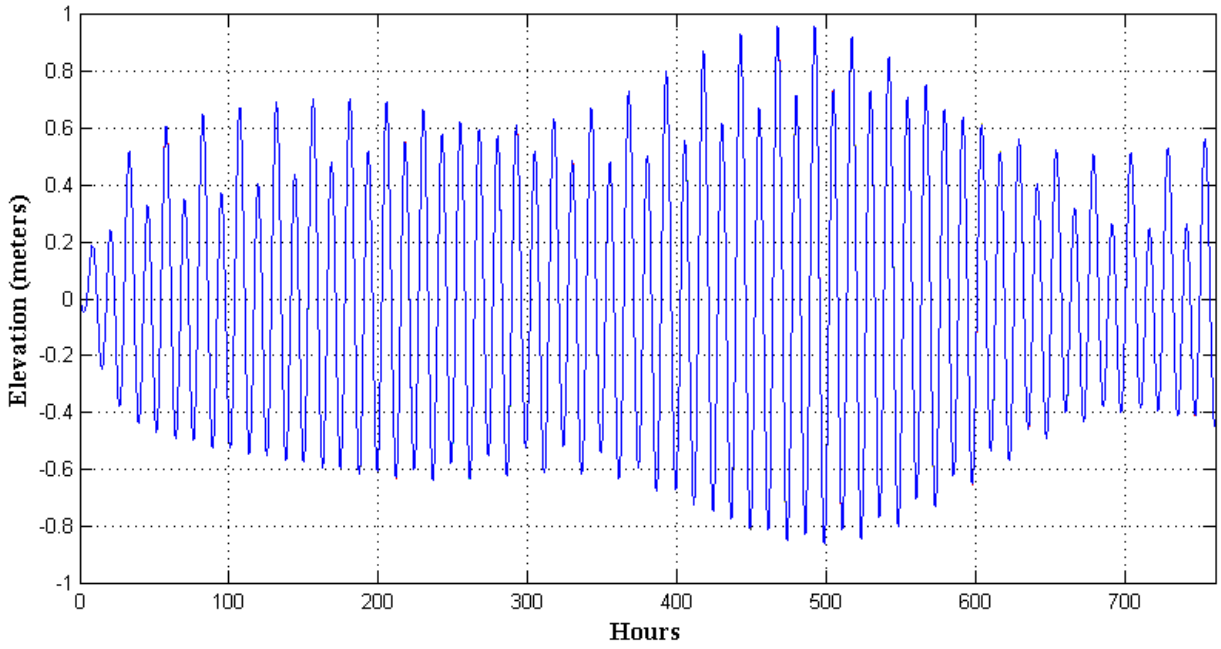


Figure 2.4 Model simulated sea level elevation on open boundary nodes

Fresh water discharge from rivers and outfalls were applied to the model as point sources (Figure 2.5). Daily streamflow data for 18 rivers (Table 2.1), creeks, and outfalls were obtained from USGS (http://nwis.waterdata.usgs.gov/usa/nwis/discharge). For those without observation and groundwater input, discharge rate was estimated from precipitation rate at watershed on Long Island and the watershed's surface area.

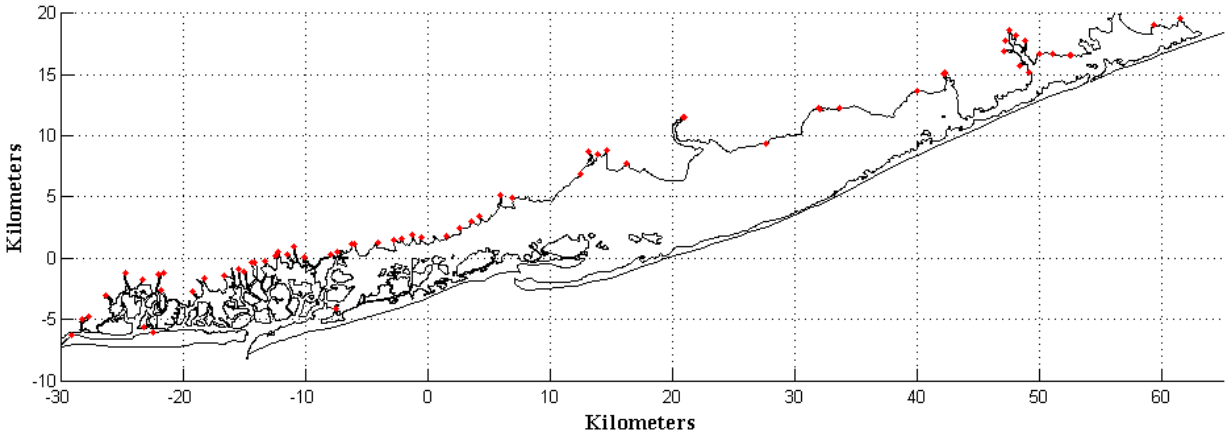


Figure 2.5 FVCOM river and outfalls discharge

| Area | Name | Observed | | Area | Name | Observed |
|---|---|---|---|---|---|---|
| Moriches Bay | Westhampton Beaver Dam Creek | | | Great South Bay | Champlin Creek | X |
| | Speonk River | | | | Crowoc Creek | |
| | Seatuck Creek | | | | Awixa Creek | |
| | Terrell River | | | | Penataquit Creek | X |
| | Orchard Neck Creek | | | | Brightwaters Canel | |
| | Senix Creek | | | | Sampawamus Creek | X |
| | Forge River | | | | Carls River | X |
| | Old Neck Creek | | | | Santapoque River | X |
| | Un-named Creek | | | | Nequntatogue Creek | |
| | Willis Creek | | | | Strongs Creek | |
| | Pouspatuck Creek | | | | Great Neck River | |
| | Lons Creek | | | | E Meadow Br/Woods Creek | X |
| | Home Creek | | | | Amityville Creek | |
| Bellport Bay | Carmans River | X | | | Narraskatuck Creek | |
| | Beaver Dam Creek | | | | Carman Creek | |
| Patchogue | Swan River | X | | S. Oyster Bay | Jones Creek | |
| | Patchogue River | X | | | Massapeaqua Creek | X |
| Nicolls Bay | Browns Creek | | | | Seaford Creek | |
| | Connetquot River | X | | | Seamus Creek | |
| Hempstead Bay | Freeport Creek | | | East Bay | Bellmore/Baltimore Creek | X |
| | Hudson Channel | | | | Baldwin Creek | |
| | Woodcleff Canal | | | | Cedar Swamp Creek | |
| | Millburn Creej | | | | Merrick Creek | |
| | Parsonage Creek | | | | Merrick Canal | |
| | Bedell Creek | | | | Mud Creek | |
| | Reed Channel | | | Outfalls | Bay Park | X |
| | Pines Brk/E. Rockaway Channel | X | | | Long Beach | X |
| | Thuxton Creek | | | | Atlantic Beach | X |
| | Macy Channel | | | | Lawrence/Bannister Bay | X |
| | Woodmere Channel | | | | Jones Beach | X |

Table 2.1 FVCOM model freshwater sources

The diurnal cycle in net surface heat flux was derived from analysis of observations by Duval (2008) of the components contributing to the net flux. Sea surface wind data was collected by buoy GSB1 (http://po.msrc.sunysb.edu/GSB/)

and the hourly east and west component of wind velocity during the period of model simulation is shown in Figure 2.6.

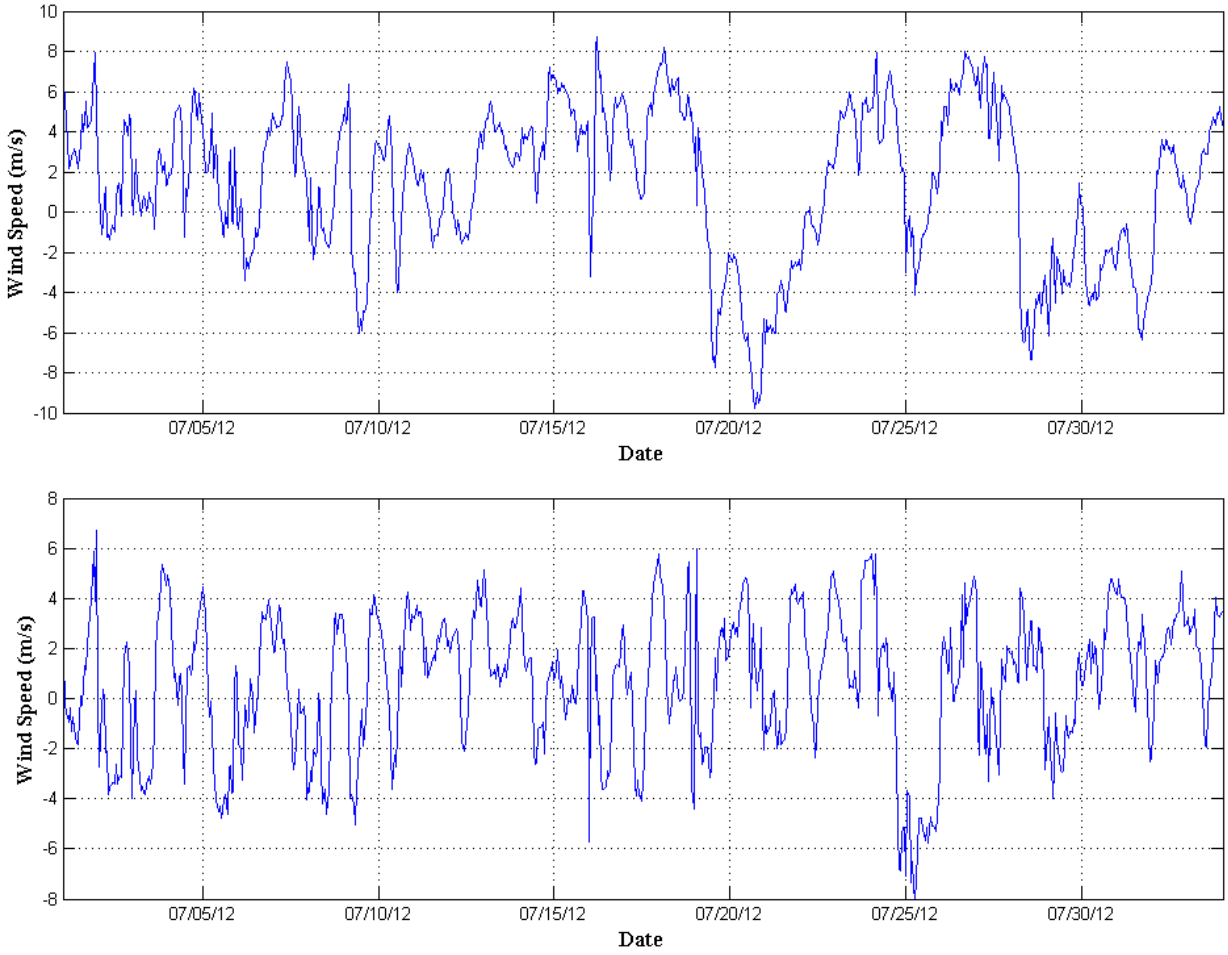


Figure 2.6 FVCOM model wind velocity (upper: east component; lower: north component)

## 2.3 FVCOM model validation

It is worth noting that this is a challenging model domain. It includes four tidal inlets whose effective cross-section and length controls tidal range in the interior. High velocity tidal flows within the inlets, especially Moriches Inlet, lead to numerical stability problems. There is a complex and dendritic network of channels and marshes which wet and dry.

In the modeling QAPP prepared for New England Interstate Water Pollution Control Commission it was emphasized that in this shallow bay, spatial variations in salinity can have only a secondary effect on the depth mean circulation. A previous validation of this model (Swanson et. al. 2013) showed that model depth-mean tidal-mean salinity agrees within 1.5 psu with annual average salinity at 12 monitoring stations occupied by Suffolk County Department of Health in GSB, and 27 monitoring stations occupied by the Town of Hempstead in the Western Bays. In this section, simulated water level and currents are compared to observations to validate the model.

To verify the tide-forced water level throughout the domain, the community harmonic analysis program T-Tide (Pawlowicz, 2002) was applied to 30-day segments of model output and observational water level data from a total of seven interior stations. Results are reported in Table 2.2. The precise positions of observational stations labeled as SeaCats are shown in Figure 2.7. The station Forge River Entrance was a temporary station occupied by SoMAS during the period 03/21/2008-04/18/2008. The positions of the USGS stations can be found on the web page (http://waterdata.usgs.gov/nwis). Considering the complexity of the morphology and bathymetry in this multi-inlet domain, and possible uncertainties in the amplitudes and phases in boundary constituents from the OSU model, results for the dominant semi-diurnal $M_2$ constituent are excellent.

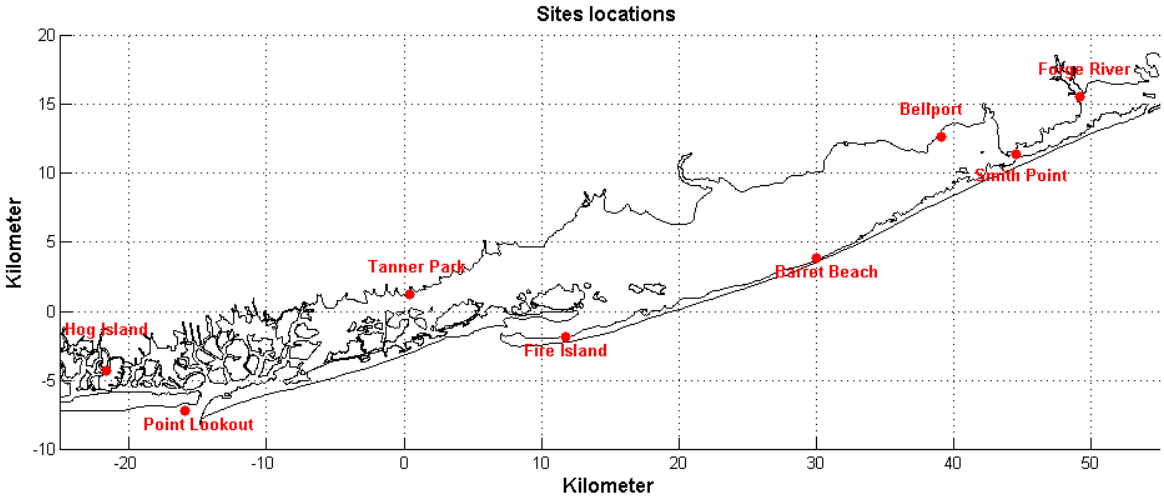


Figure 2.7 SeaCat observation and USGS sites

| **USGS Point Lookout** | | | | | | |
|---|---|---|---|---|---|---|
| Model | | | | USGS Observation | | |
| Constituent | Amplitude(M) | Phase(degree) | | Constituent | Amplitude(M) | Phase(degree) |
| M2 | 0.60 | 357.08 | | M2 | 0.59 | 0.19 |
| S2 | 0.12 | 23.00 | | S2 | 0.15 | 42.21 |
| N2 | 0.15 | 348.36 | | N2 | 0.16 | 350.78 |
| K1 | 0.08 | 180.82 | | K1 | 0.07 | 185.05 |
| O1 | 0.05 | 188.64 | | O1 | 0.03 | 200.84 |
| | | | | | | |
| **Fire Island** | | | | | | |
| Model | | | | SeaCat | | |
| Constituent | Amplitude(M) | Phase(degree) | | Constituent | Amplitude(M) | Phase(degree) |
| M2 | 0.27 | 13.29 | | M2 | 0.24 | 7.52 |
| S2 | 0.05 | 35.61 | | S2 | 0.05 | 36.38 |
| N2 | 0.06 | 3.15 | | N2 | 0.05 | 347.48 |
| K1 | 0.05 | 200.86 | | K1 | 0.05 | 185.98 |
| O1 | 0.03 | 213.14 | | O1 | 0.03 | 208.90 |
| | | | | | | |
| **Forge River** | | | | | | |
| Model | | | | Observation | | |
| Constituent | Amplitude(M) | Phase(degree) | | Constituent | Amplitude(M) | Phase(degree) |
| M2 | 0.26 | 41.48 | | M2 | 0.25 | 29.27 |
| S2 | 0.04 | 77.52 | | S2 | 0.06 | 52.67 |
| N2 | 0.05 | 41.14 | | N2 | 0.05 | 27.02 |
| K1 | 0.04 | 220.49 | | K1 | 0.05 | 177.12 |
| O1 | 0.04 | 230.38 | | O1 | 0.02 | 207.09 |
| | | | | | | |
| **USGS Hog Island** | | | | | | |
| Model | | | | USGS Observation | | |
| Constituent | Amplitude(M) | Phase(degree) | | Constituent | Amplitude(M) | Phase(degree) |
| M2 | 0.55 | 17.67 | | M2 | 0.63 | 10.47 |
| S2 | 0.10 | 49.50 | | S2 | 0.13 | 58.12 |
| N2 | 0.12 | 13.55 | | N2 | 0.15 | 5.53 |
| K1 | 0.08 | 196.36 | | K1 | 0.09 | 193.06 |
| O1 | 0.05 | 203.15 | | O1 | 0.04 | 196.63 |
| | | | | | | |
| **Barret Beach** | | | | | | |
| Model | | | | SeaCat | | |
| Constituent | Amplitude(M) | Phase(degree) | | Constituent | Amplitude(M) | Phase(degree) |
| M2 | 0.14 | 111.22 | | M2 | 0.16 | 96.78 |
| S2 | 0.02 | 143.98 | | S2 | 0.02 | 125.75 |
| N2 | 0.02 | 96.08 | | N2 | 0.03 | 82.18 |
| K1 | 0.02 | 263.55 | | K1 | 0.04 | 255.60 |
| O1 | 0.02 | 275.97 | | O1 | 0.02 | 256.26 |
| | | | | | | |
| **Tanner Park** | | | | | | |
| Model | | | | SeaCat | | |
| Constituent | Amplitude(M) | Phase(degree) | | Constituent | Amplitude(M) | Phase(degree) |
| M2 | 0.21 | 69.88 | | M2 | 0.20 | 60.12 |
| S2 | 0.04 | 99.38 | | S2 | 0.03 | 95.07 |
| N2 | 0.04 | 66.48 | | N2 | 0.03 | 43.25 |
| K1 | 0.04 | 241.94 | | K1 | 0.05 | 224.13 |
| O1 | 0.03 | 252.44 | | O1 | 0.03 | 242.26 |
| | | | | | | |
| **Bellport** | | | | | | |
| Model | | | | SeaCat | | |
| Constituent | Amplitude(M) | Phase(degree) | | Constituent | Amplitude(M) | Phase(degree) |
| M2 | 0.15 | 115.29 | | M2 | 0.17 | 99.84 |
| S2 | 0.02 | 148.63 | | S2 | 0.03 | 129.10 |
| N2 | 0.03 | 99.89 | | N2 | 0.04 | 67.41 |
| K1 | 0.03 | 292.39 | | K1 | 0.04 | 226.24 |
| O1 | 0.02 | 278.42 | | O1 | 0.02 | 276.74 |

Table 2.2 Comparison of tidal constituents from FVCOM with observations

The model skill in tidal currents was also assessed by comparing the $M_2$ tidal ellipses of model currents near the buoy to the one of ADCP observation. Both ellipses were calculated from the depth-averaged currents, and the result is shown in figure 2.8. The model and observation tides have similar orientation and minor axes, while the model results overestimated the major axes by approximately 0.015 m/s. The overall model skill in tidal currents is good.

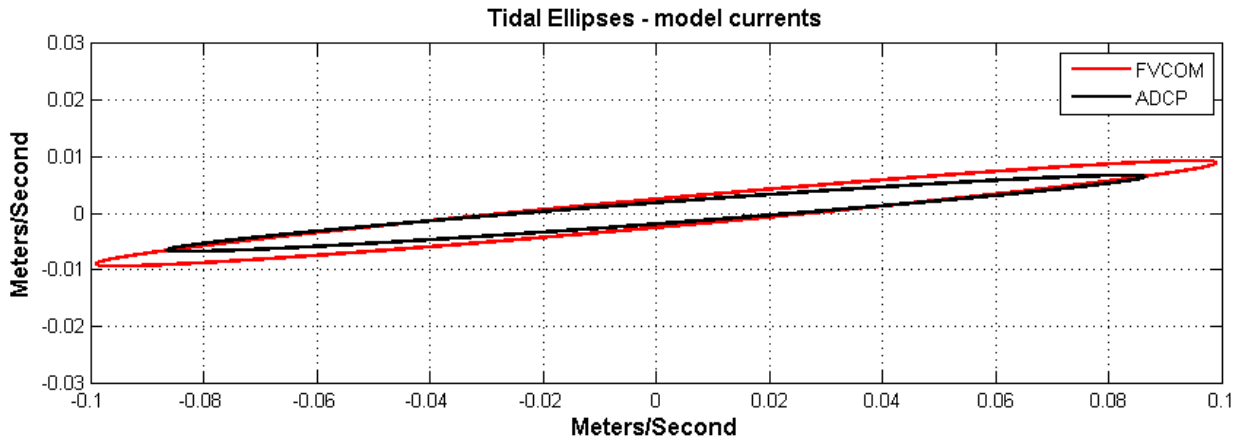


Figure 2.8 $M_2$ tidal ellipses of FVCOM model currents near the buoy and ADCP observation

The model skill in simulating wind-driven processes is tested by applying EOF analysis on the low-pass filtered (34 hours cutoff period) model currents close to the position of buoy GSB#1 and comparing the results with the observed currents by ADCP. Similar to the observed currents, the model currents are dominated by the first two modes (account for approximately 92% together). Pattern of the first mode (Figure 2.9 left) shows currents in the lagoon axial direction with strong shear at the surface; the second mode (Figure 2.9 right) shows currents in the lateral direction which are also sheared in the surface layer.

Both first and second principal components of the model currents are similar to the observed results (Figure 2.10, Figure 2.11), and the correlation coefficients are 0.8310 and 0.8521 separately. In terms of cross-correlation with the wind speeds (Figure 2.12), the first mode is highly correlated with the longitudinal winds (80° from the north) and the second mode is highly correlated with the lateral winds (350° from the north). The correlation coefficients are both higher than 0.9, and the correlation patterns are similar to the observed results. Thus based on the comparisons of current patterns, principal components, and the responses to local wind forcing, the model's skill in simulating wind-driven processes is robust.

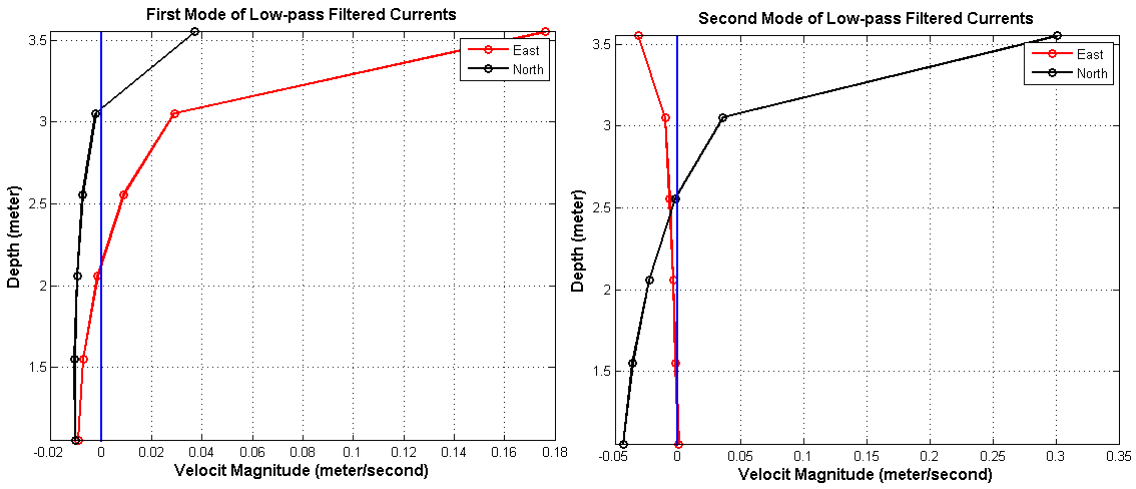


Figure 2.9 First (left) and second (right) modes of low-pass filtered model currents

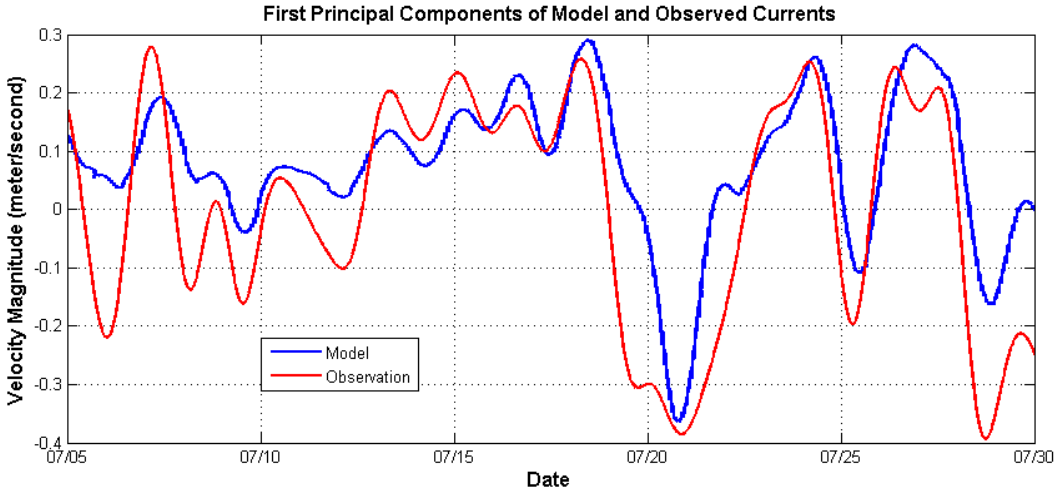


Figure 2.10 First principal components of low-pass filtered model and observation currents

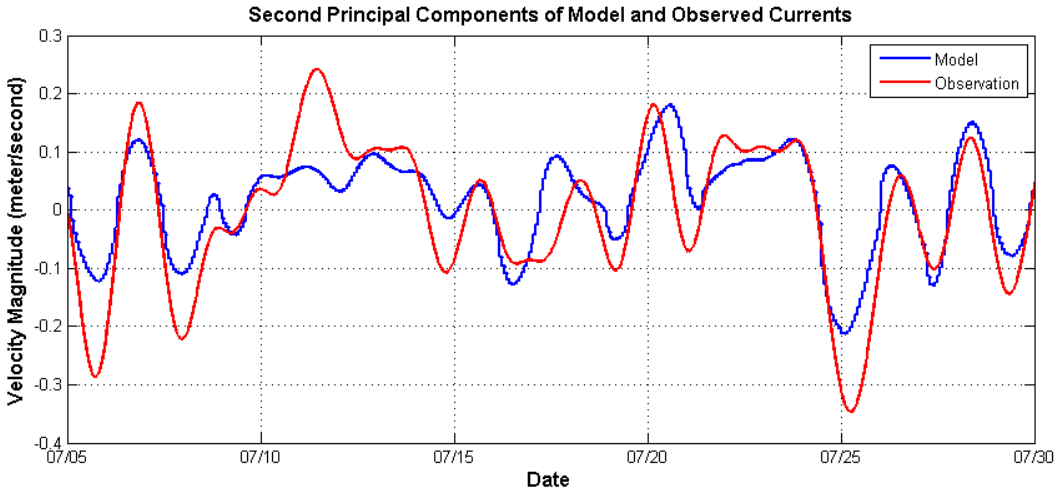


Figure 2.11 principal components of low-pass filtered model and observation currents

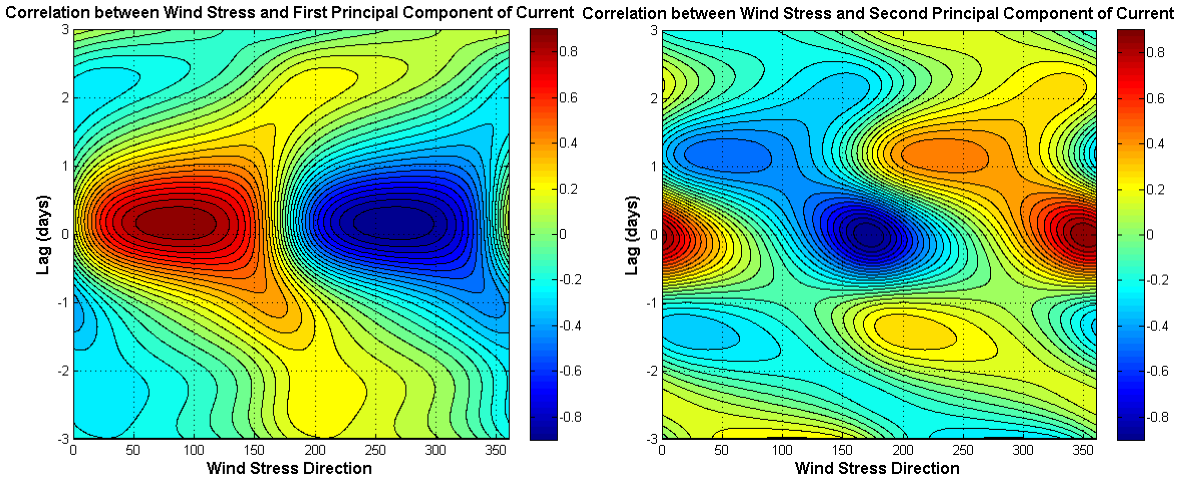


Figure 2.12 Cross correlation between wind speed and first (left)/second (right) principal components of model currents

## 2.4 Lagrangian particle tracking algorithm

The movement of the parcels will be simulated by the combined influence of both advection and turbulent motion.

The advection will be calculated by a 4$^{th}$ order Runge-Kutta scheme in space and time. This scheme solves the 3-dimension current velocity at the parcel location by using an iterative process that incorporates velocities at several times to provide the most robust estimate of the parcel movement. Current velocities obtained from the Runge-Kutta scheme are multiplied by the time interval to get the displacement of the parcel in each direction, and displacements are then added to the original position of the parcel to estimate the new position of the parcel:

$$\vec{x}_{n+1} = \vec{x}_n + \vec{U}_{R-K}\Delta t$$

Besides the advective motion determined by the model's current flow, the turbulent motion at scales smaller than the grid resolution will be calculate in the simulation. To estimate the small-scale motion, it is necessary to add a random component to reproduce the turbulent diffusion. A random displacement model proposed by Visser (1997) will be adopted in the parcel model to simulate sub-grid scale turbulent movement in vertical direction:

$$z_{n+1} = z_n + K'(z_n)\Delta t + R\{\frac{2}{r}K[z_n + \frac{1}{2}K'(z_n)\Delta t]\Delta t\}^{1/2}$$

where $z_n$ is the initial parcel location, K is the vertical diffusivity, $\Delta t$ is the time interval for the random displacement model, $K'(z_n) = \partial K / \partial z$ evaluated at $z_n$, and R is a random number generator with uniform distribution from -1 to 1. Compared with the random walk models, the random displacement model incorporates the 2nd item on the right hand side as an 'advective' component induced by the vertical gradient of diffusivity. As suggested by Visser (1997), this nonrandom component will offset the numerical artificial accumulation of parcels around areas with low diffusivity.

In the horizontal direction with relatively homogeneous diffusivity, $K_h$, we can assume $K_h$'(x,y)=0, so the nonrandom component vanish, and the random displacement model becomes random walk model:

$$x_{n+1} = x_n + R[\frac{2}{r} K_h(x_n)\Delta t]^{1/2}$$

In a report discussing residence time (Aikman, et. al., 2004), residence time calculated with Lagrangian particle method was compared with results from other methods (i.e., tracer patch method and residual current method). The results from those methods tend to be similar with each other, and the Lagrangian method is the most computing-efficient.

# Chapter 3 Circulation Structure in GSB

The transport and effective horizontal mixing processes in coastal area are controlled by current structures (Bowden, 1965; Okubo, 1968; Zimmerman, 1985), therefore the circulation dynamics were studied first as a basis for discussions related to the mixing/fate of the particles in GSB.

According to Wong (1986, 1993) and Wong and Wilson (1984), tidal energy attenuates very rapidly proceeding through the inlets into the interior GSB and has weaker influence on the lagoon circulation than the synoptic-period winds. Also for the vertical shear in the tidal currents is negligible, thus the dynamics study in GSB is focused on the synoptic-period wind-driven currents. In the longitudinal direction, a typical two-layer vertical shear develops in an idealized rectangular, flat-bottom basin under steady wind forcing; in basins with lateral-varying bathymetry, laterally sheared currents are generated with down-wind currents above shallower areas and up-wind currents in the deeper channel (Csanady, 1973; Signell, 1990; Glorioso and Davies, 1995). While as a realistic case, the reaction of GSB water to the wind is controlled by interactions between the wind stress and complicated bathymetry, therefore the flow structure is more complicated than the two-layer or three layer one. In addition, as shown by EOF analysis of the observed currents records, circulation in the lateral direction is also important, but it is more difficult to find a general solution for it.

In this chapter, with the assistance of numerical simulations the momentum balance and vertical/horizontal structure of longitudinal currents in GSB were analyzed in section 3.1; in section 3.2, momentum balance and structures of lateral currents were discussed; vertical vorticity of currents was analyzed in section 3.3.

## 3.1 Wind-driven longitudinal circulation in central GSB

### 3.1.1 Wind-driven longitudinal momentum balance in central GSB

The momentum equation in the longitudinal direction is written as:

$$\frac{\partial u}{\partial t} = -(u\frac{\partial u}{\partial x} + v\frac{\partial u}{\partial y} + w\frac{\partial u}{\partial z}) - g\frac{\partial \eta}{\partial x} - \frac{g}{\rho}\int_z^\eta \frac{\partial \rho}{\partial x}dz + \frac{1}{\rho}\frac{\partial \tau_{xz}}{\partial z} + fv \qquad (3.1)$$

in which the vertical direction points upward with zero point at the un-disturbed sea level. In (3.1), the local acceleration of velocity (left hand side term) is due to non-linear advection, barotropic pressure gradient induced by sea level slope in longitudinal direction, baroclinic pressure gradient produced by density gradient in longitudinal direction, vertical stress divergence, and Coriolis force on the right hand side.

The depth-averaged form of equation (3.1) is:

$$\frac{\partial \bar{u}}{\partial t} = -\frac{1}{H+\eta}\int_{-H}^{\eta}(u\frac{\partial u}{\partial x} + v\frac{\partial u}{\partial y} + w\frac{\partial u}{\partial z})dz - g\frac{\partial \eta}{\partial x} - \frac{1}{H+\eta}\int_{-H}^{\eta}(\frac{g}{\rho}\int_z^\eta \frac{\partial \rho}{\partial x}dz)dz + \frac{\tau_{sx}}{\rho(H+\eta)} - \frac{\tau_{bx}}{\rho(H+\eta)} + f\bar{v} \qquad (3.2)$$

in which $\bar{u}$ and $\bar{v}$ are depth-averaged velocity in longitudinal and lateral directions, H is the undisturbed water depth, and $\eta$ is the sea surface elevation; vertical stress term is represented by longitudinal surface and bottom stresses in this form.

In order to examine the synoptic time scale longitudinal momentum balance in central GSB, time series of depth-averaged and low-pass filtered momentum terms on a typical transection (S1, Figure 3.1, and Figure 3.2) were calculated, and the results for two stations – station 7 in the middle deep channel and station 15 on the shoal south side are shown in Figure 3.3. At both stations, the Coriolis effect, baroclinic pressure gradient, and local acceleration were small and negligible compared to the other terms. In the deep channel, barotropic pressure gradient was the largest term, and balanced mainly by the sum of surface and bottom stress divergence, which almost always had the same sign and similar magnitude, with bottom stress term slightly smaller; the advection term was sometimes big enough to be noticed but negligible most of the time. On the southern shoal, due to smaller depth, the longitudinal wind (Figure 3.3) with the same magnitude produced larger depth-averaged surface stress divergence; compared to the deep channel counterpart, the bottom stress at station 15 had similar direction and magnitude, indicating the bottom current was in the same direction as the one at station 7 but with smaller magnitude; the barotropic pressure gradient was also magnified to balance the enhanced surface stress term; advection term in shallow water became

more importance, and it had similar magnitude as bottom stress, but both of them were much smaller than barotropic pressure gradient and surface stress.

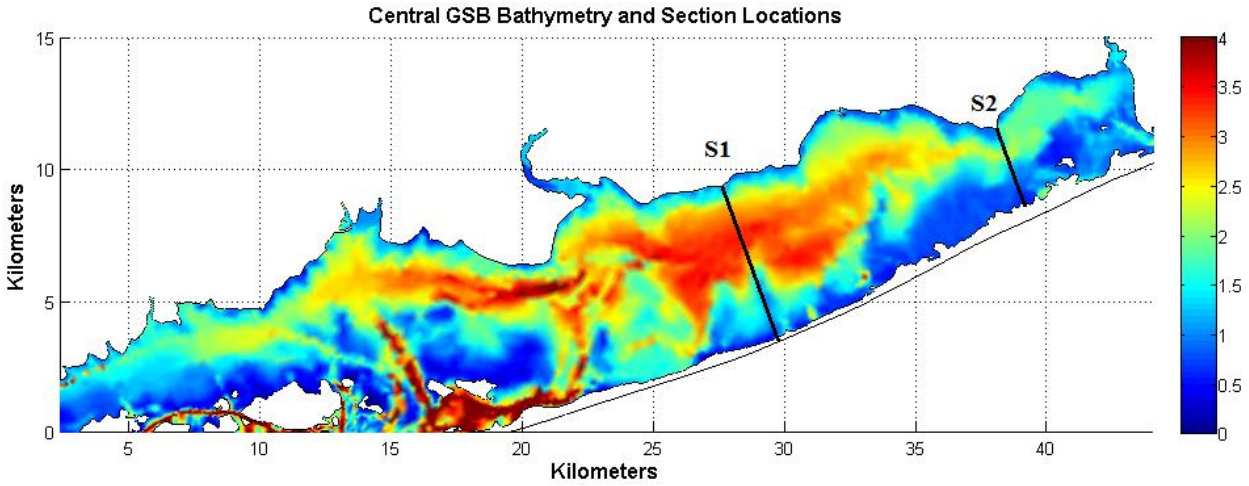


Figure 3.1 Great South Bay Bathymetry and Section Locations

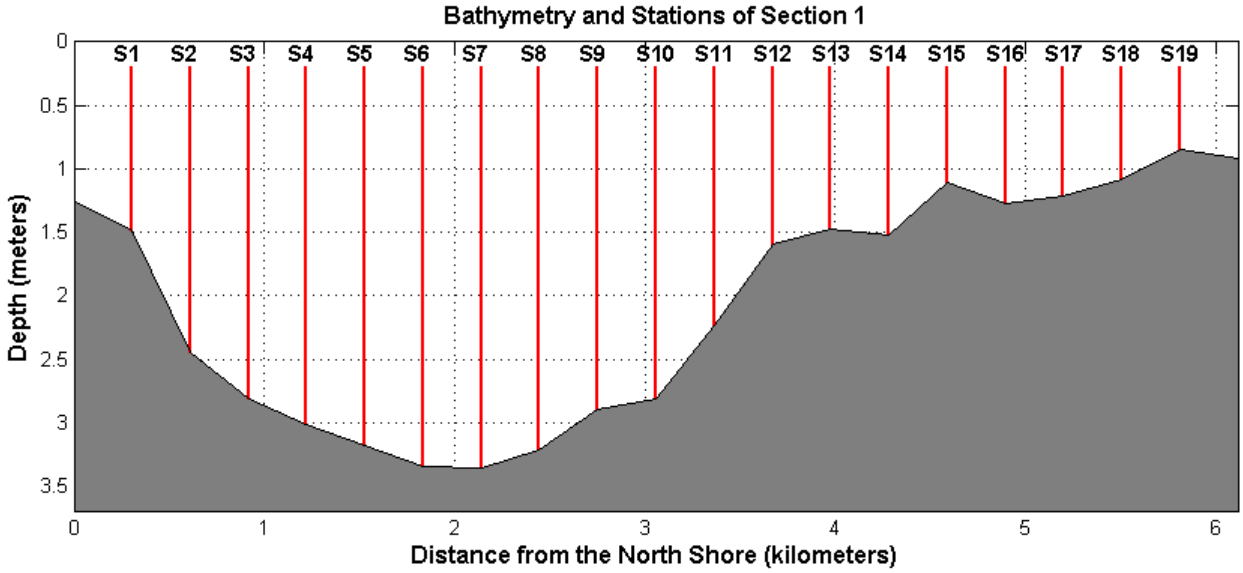


Figure 3.2 Bathymetry of Section 1 and Stations Locations

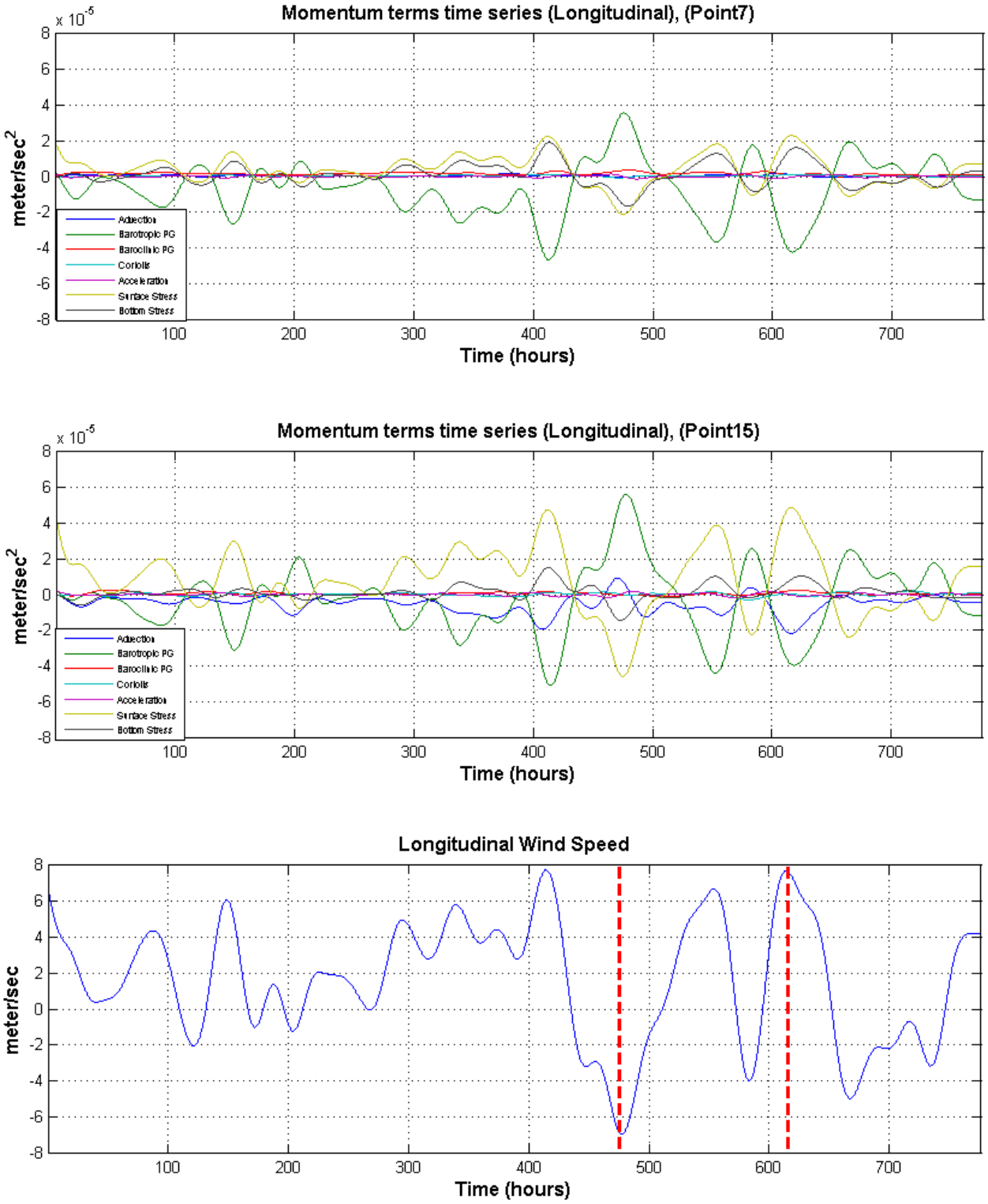


Figure 3.3 Time series of longitudinal momentum terms at station7 (upper), station 15 (middle) at section 1, and longitudinal wind speed (lower)

Another section (S2, Figure 3.1 and Figure 3.4) was selected near Bellport Bay to the east of S1. This section is shorter in lateral direction and has generally smaller depth than S1, with a channel narrower than 1 km closer to the north shore. As on section 1, the momentum balance at two typical stations: S7 in the channel (about 2.2 meters deep) and S16 on the shallower southern flank (about 0.8 meter deep) at this section were used to examine the mechanism controlling the circulation in nearby area (Figure 3.5). Due to the shallower water depth of this section, the magnitudes of momentum terms at both stations were larger than their counterparts at section 1, but the momentum balances were similar. In the deep channel, barotropic pressure gradient was balanced by the sum of surface and bottom stress. Over the shoal barotropic pressure gradient increased a little while surface stress term increased significantly, and the bottoms stress had opposite direction to the surface stress so their difference balanced with barotropic pressure gradient.

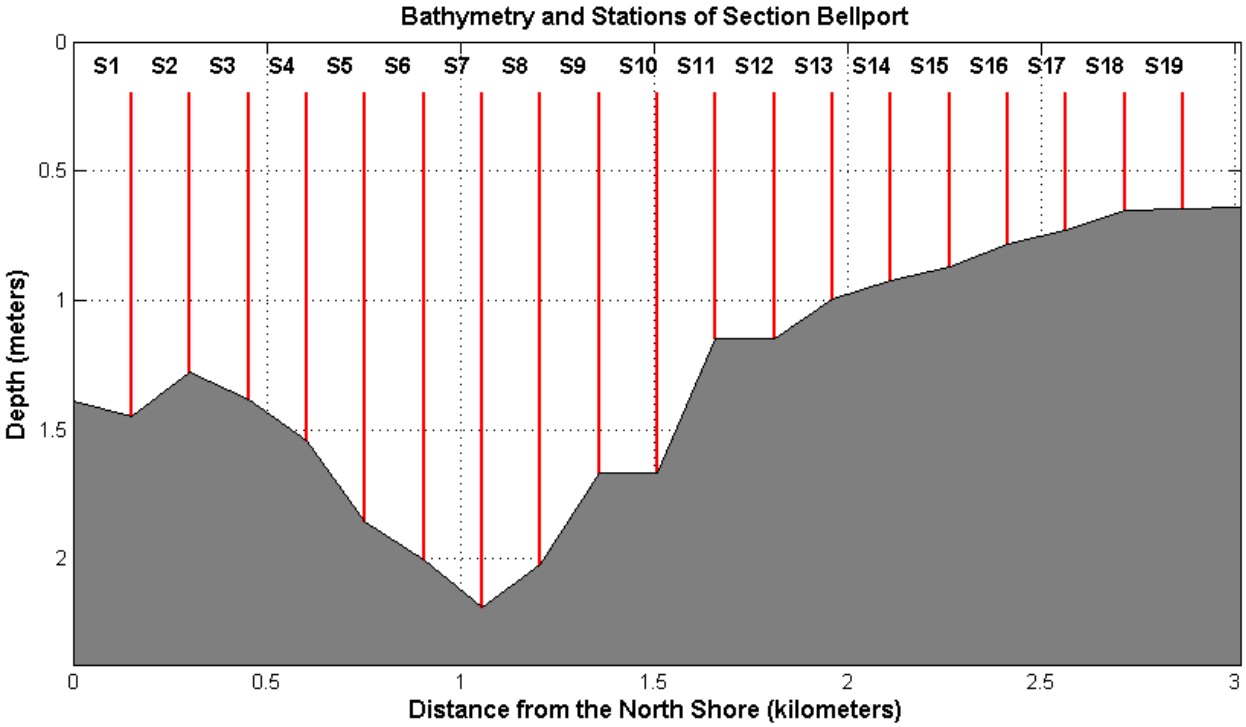


Figure 3.4 Bathymetry of Section 2 and Station Locations

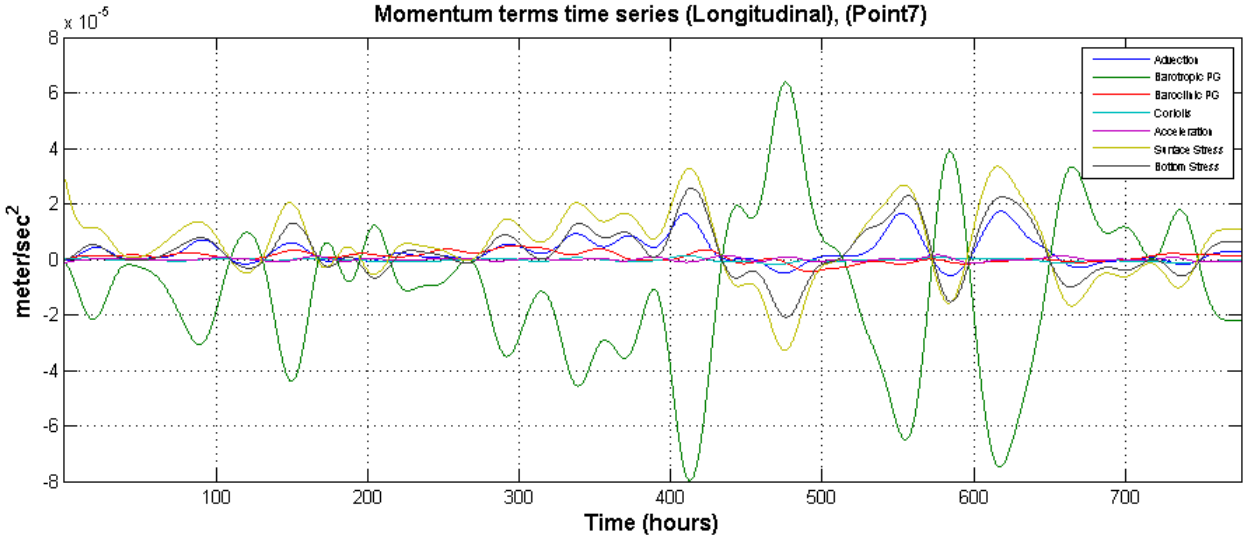

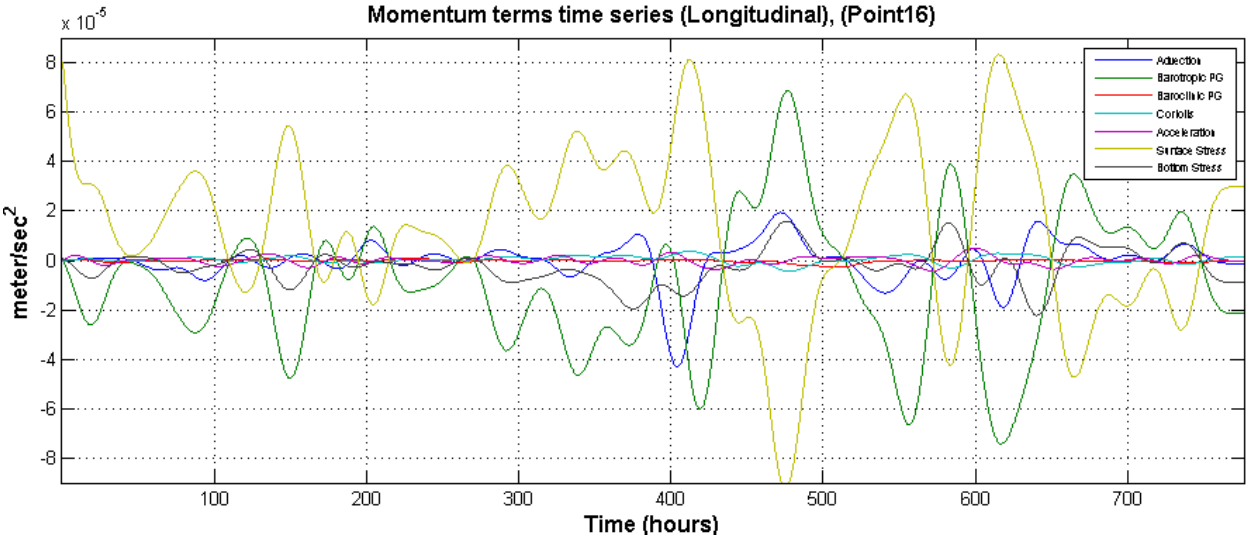


Figure 3.5 Time series of longitudinal momentum terms at station7 (upper), station 15 (lower) at section 2

To summarize, the wind-driven longitudinal circulation in central GSB was controlled by the balance between barotropic pressure gradient and sum of surface and bottom stress; baroclinicity, Coriolis and local acceleration were negligible; in shallower area the nonlinear advection was significant during some time but small enough to be neglect for most of the time.

### 3.1.2 Vertical structure of wind-driven longitudinal circulation in central GSB

As discussed in Chapter 1, the vertical structure of wind-driven circulation in central GSB has a surface downwind flow and an upwind countercurrent at depth, and has log layers at both surface and bottom. In the study of wind-driven countercurrent flow, Wu and Tsanis (1995) proposed an analytical solution for the vertical profile of current featured with surface and bottom log layers:

$$u(z) = Au_{*s}\ln(1+\frac{z}{z_s}) + Bu_{*s}\ln(1-\frac{z}{z_b+h}) + C \quad \text{(3.3: Wu and Tsanis, 1995)}$$

where z is specific vertical position and increases upward, h is the water depth at given location, $z_s$ and $z_b$ are the characteristic lengths at surface (z=h) and bottom (z=0) where velocities are zero, $u_{*s} = \sqrt{\tau_s(surface\_stress)/\rho}$ is the surface shear velocity, A, B, and C are coefficients to be determined. This general formula was utilized in this research of vertical structure of longitudinal circulation in central GSB. To determine the coefficients three conditions were used here: (1) shear stress at the surface is induced by wind stress; (2) velocity is zero at bottom; (3) the depth averaged velocity equals to U. For condition (1), eddy viscosity $k_z$ is required, and a cubic polynomial profile of eddy viscosity proposed by Signell (1990) was applied:

$$k_z(z) = -\kappa u_{*s}(z-h) + \frac{\kappa(u_{*b}-2u_{*s})}{h}(z-h)^2 + \frac{\kappa(u_{*b}-u_{*s})}{h^2}(z-h)^3 \quad \text{(3.4: revised from Signell, 1990)}$$

where $\kappa$=0.4 is the von Karman's constant, $u_{*b}$ is the bottom shear velocity. With the above conditions and eddy viscosity profile, the values of A, B, and C at given location with water depth h and depth-averaged velocity are written as:

$$A = \frac{u_{*_s} q_2}{\kappa z_{sh}[1-(\beta-2)z_{sh}-(\beta-1)z_{sh}^2][\frac{q_2}{1+z_{sh}}+\frac{q_1}{z_{bh}}]} + \frac{U}{z_{bh}} \cdot \frac{1}{[\frac{q_2}{1+z_{sh}}+\frac{q_1}{z_{bh}}]} \quad (3.5)$$

$$B = -\frac{u_{*_s} q_1}{\kappa z_{sh}[1-(\beta-2)z_{sh}-(\beta-1)z_{sh}^2][\frac{q_2}{1+z_{sh}}+\frac{q_1}{z_{bh}}]} + \frac{U \cdot z_{bh}}{q_1(z_{sh}+1)+q_2 \cdot z_{bh}} \quad (3.6)$$

$$C=0 \quad (3.7)$$

in which

$$q_1 = (1+z_{sh})\ln(1+\frac{1}{z_{sh}})-1 \quad (3.8)$$

$$q_2 = z_{bh}\ln(1+\frac{1}{z_{bh}})-1 \quad (3.9)$$

where $z_{sh} = z_s / h$ and $z_{bh} = z_b / h$.

Based on (3.3) and (3.5)-(3.8), vertical profile of longitudinal current at given locations could be calculated if the water depth, surface and bottom shear velocity (or stress), and depth-averaged current velocity are provided. In this study, all the above information was obtained from FVCOM simulation results.

At approximately hour 475(Figure 3.3 lower) when the longitudinal wind speed had maximal magnitude (7 m/s) toward the west, water in central GSB set up against the western end (Figure 3.6, upper) to form an eastward sea level gradient

acting against the westward wind forcing. It was noticed that sea level on the northern side of the lagoon was higher than the one on the southern side, and this might be due to the outward transport of water through Fire Island Inlet from the southern part at the same time when more water was piled up in the northern part. The longitudinal velocity on section 1 mainly had three layers across the lateral direction: two downwind layers above shoals on the north and south dominated by surface wind stress and one layer in the middle channel with upwind flow within most part of water column dominated by barotropic pressure gradient due to water setup. The vertical shear of the longitudinal currents was stronger above flat bottoms in the middle channel and southern shoal: velocity varied from -0.05m/s to +0.08m/s over top 0.6 meters and from +0.08m/s to zero over bottom 0.5 meters in the middle; on the southern side, velocity varied from -0.3m/s to -0.1m/s over the 1 meter water column. On the other hand, the vertical shear was much weaker above sloping bottoms, but the lateral shear became significant in those areas: velocity varied by 0.24m/s from 0.5 to 1.5 kilometers and by 0.28 from 2.5 to 4.5 kilometers. In general, this result agreed with previous analytical studies of the influence of bottom slope on wind-driven current structure (Csanady, 1973; Signell, 1990; Wong, 1994; Mathieu, 2002). On section 2 close to Bellport Bay (Figure 3.6 lower), two downwind layers on northern and southern shoals were also observed with velocity variations of approximately 0.2m/s over 1meter water column in the

southern one; similar to section 1, lateral shear of the current over sloping bottom was also substantial: velocity difference of 0.1m/s is observed across a lateral distance of 0.75 kilometers on both sides; unlike results on section 1, however, a large proportion of the water column above deeper middle channel moved downwind and the depth averaged velocity was also slightly downwind, and this could be explained by the westward jet coming from Smith Point channel.

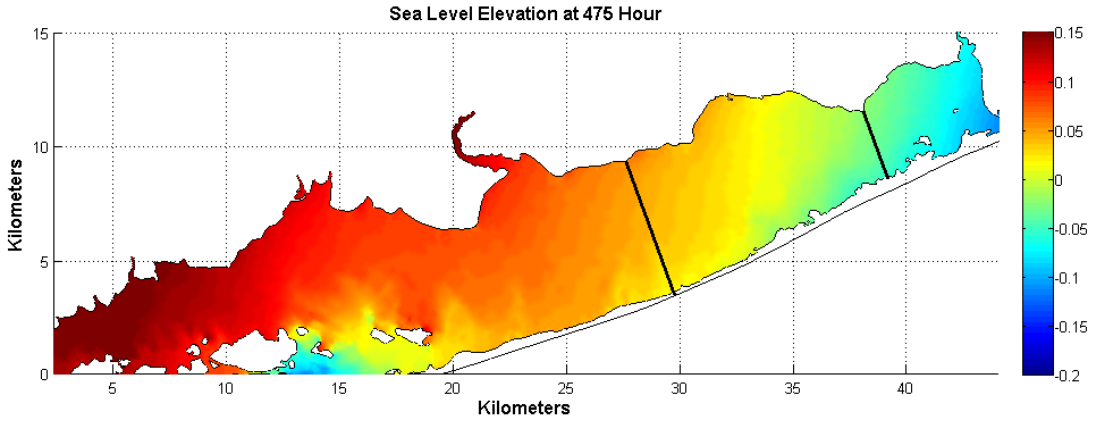

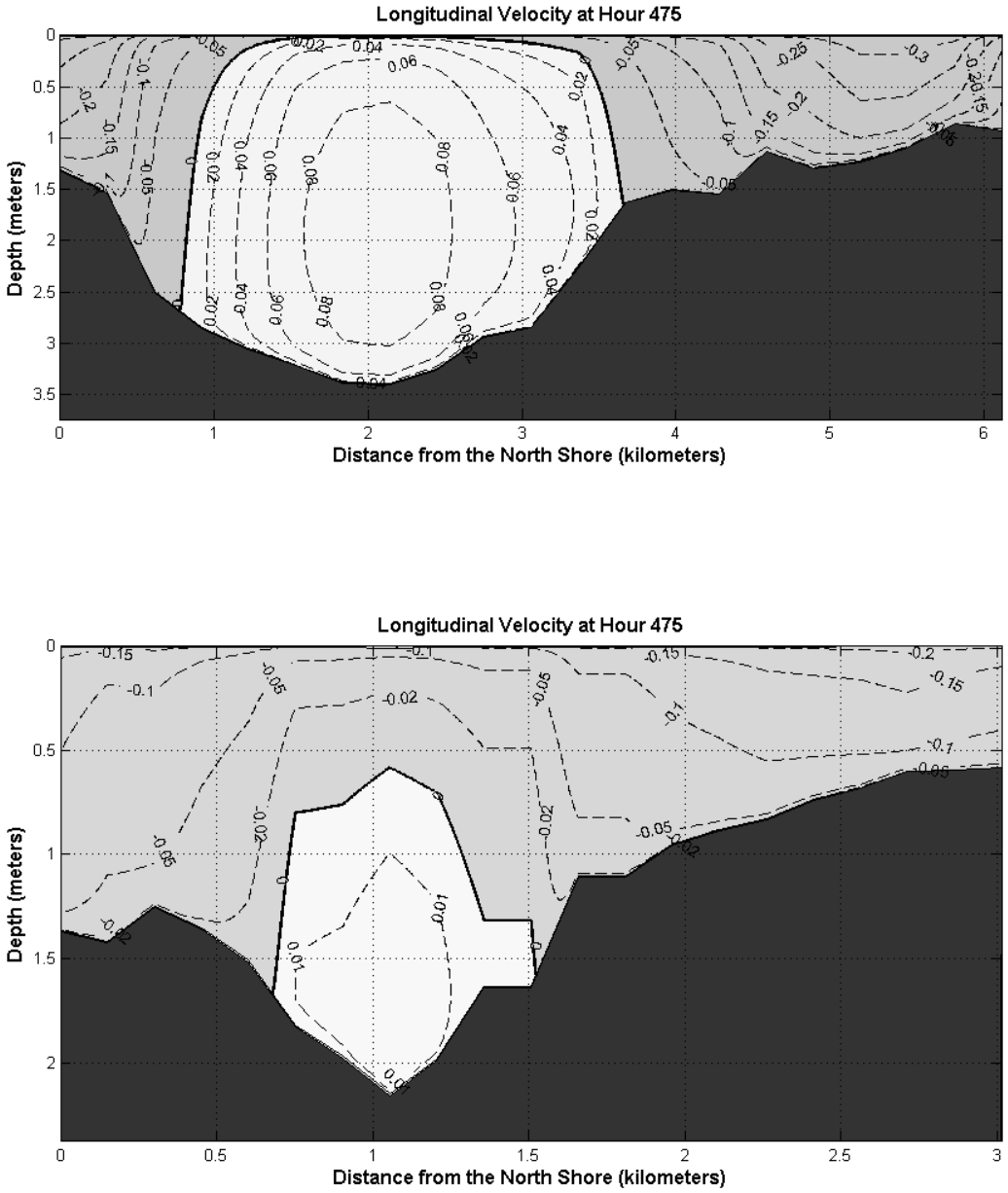


Figure 3.6 Sea level elevation in central GSB (upper), longitudinal current velocity on section 1 (middle) and 2 (lower) at Hour 475

When the longitudinal wind reached its positive maximum at hour 620, water in central GSB was set up against the eastern end of the lagoon and developed a negative longitudinal sea level gradient opposing the wind stress

(Figure 3.7, upper). Longitudinal circulation on section 1 (Figure 3.7, middle) had similar structure with the one under westward wind: upwind (westward) current in middle channel and downwind (eastward) current on shoals. Velocity had a vertical variation of 0.11m/s within the top 0.3 meters over middle channel and one of 0.25m /s over the 1 meter water column on southern flank; over sloping bottom the lateral velocity variation reached 0.2m/s across less than 1.5 kilometers. Circulation structure on section 2 under eastward wind forcing differed from the one under westward wind significantly, and without channel jet from Smith Point, it was more similar to the circulation on section 1. The magnitude of vertical current shear on section 2 was similar to the one on section 1, while the lateral shear on sloping bottom was larger (0.28 over 1 kilometer) due to smaller cross-section distance.

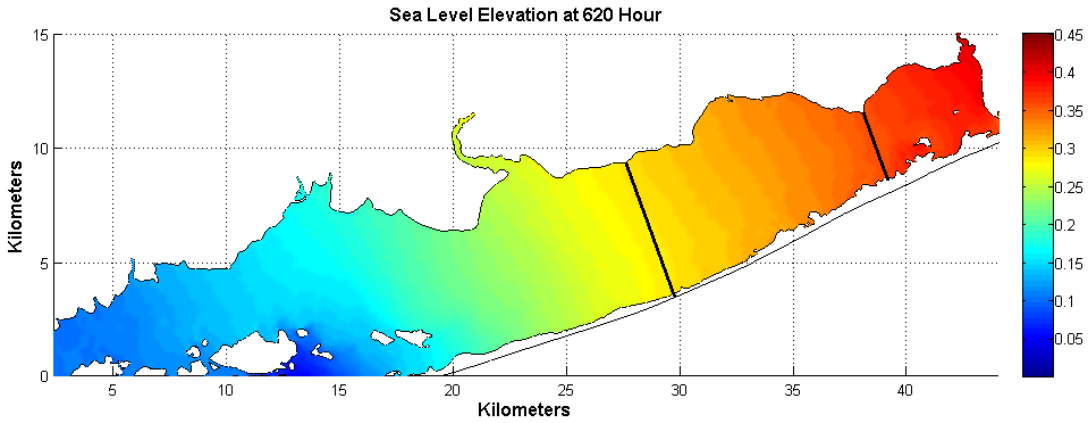

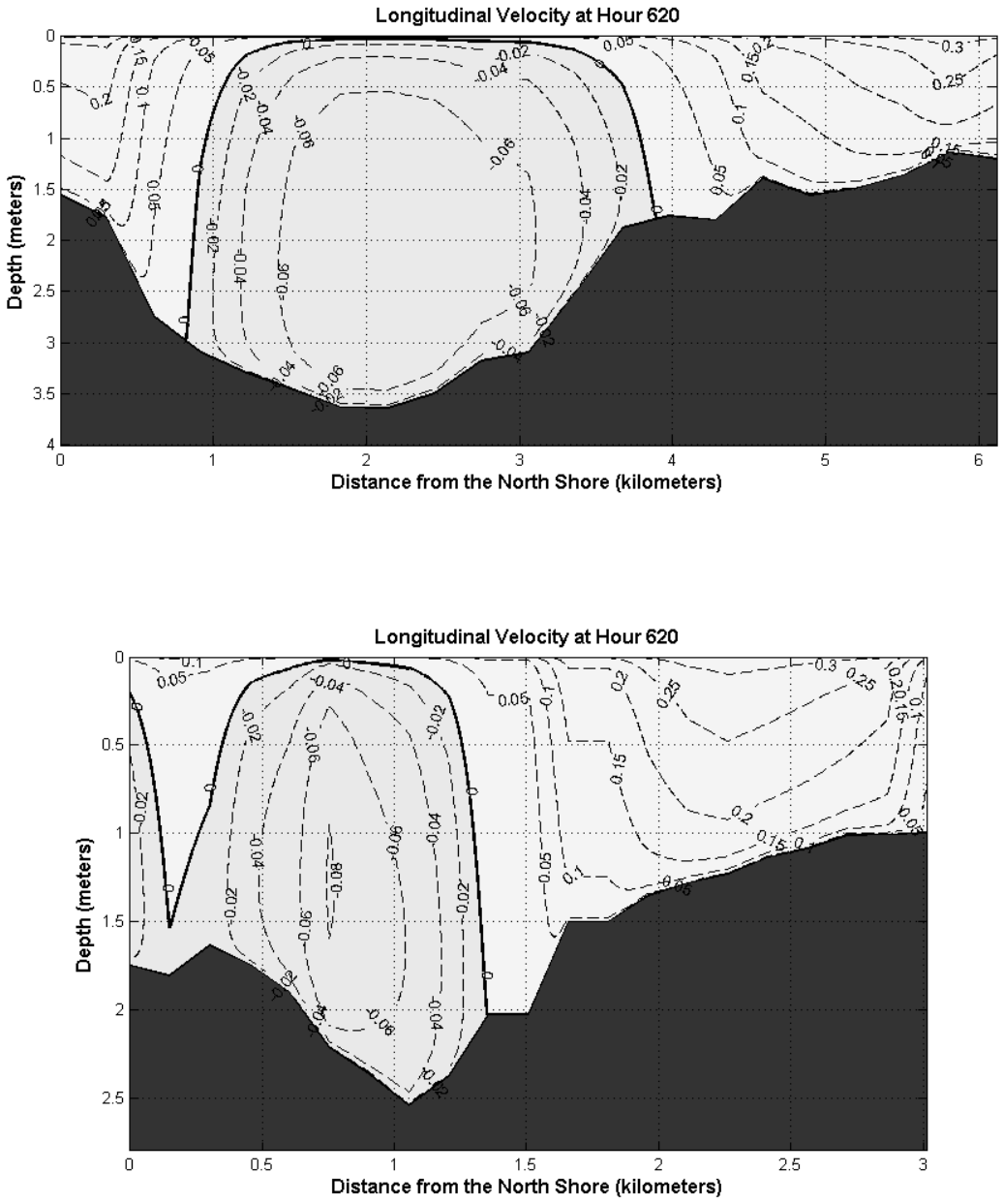


Figure 3.7 Sea level elevation in central GSB (upper), longitudinal current velocity on section 1 (middle) and 2 (lower) at Hour 620

To further demonstrate the character of wind-driven longitudinal circulation in central GSB, the vertical structures through the 30-day simulation for the four typical locations are shown. At deep channel on the middle bay section 1 (Figure

3.8a), a thin top layer (less than 5% of the water column) was driven by surface stress to move downwind, but the velocity varied rapidly over this layer and became upwind within most part of the water column where it kept relatively uniform before reaching the bottom log layer. It is also clear that magnitudes of the velocity and velocity shear were highly correlated to the wind forcing, and when there was no major wind event, the currents in both up- and downwind directions were weak. In shallower areas on both sections (Figure 3.8b, d), the whole water column was occupied by downwind flow and the velocity magnitude decreased from surface to bottom with relatively larger gradient in both log layers. The responses to wind forcing of these shallower stations were more obvious than those in deep channel due to the larger magnitude of surface stress term in the momentum balance which is inversely proportional to the water depth. The vertical structure of longitudinal currents at channel station 7 on section 2 (Figure 3.8c) was similar to the one on section 1 except that around hour 475, instead of an eastward current within major part of water column under the influence of westward storm, the section 2 station showed a downwind flow in over 30% of water column near surface and a relatively weak upwind flow in rest part, which together produce a downwind depth-average flow. This could be explained by the jet from Smith Point channel generated by the extreme westward wind.

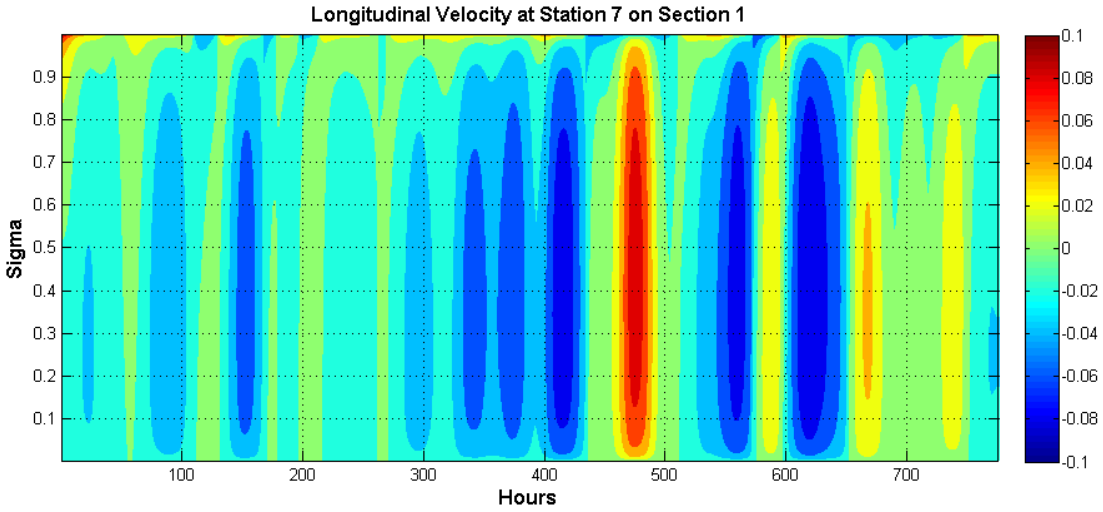
Longitudinal Velocity at Station 7 on Section 1
Sigma
Hours
0.9
0.8
0.7
0.6
0.5
0.4
0.3
0.2
0.1
100
200
300
400
500
600
700
0.1
0.08
0.06
0.04
0.02
0
-0.02
-0.04
-0.06
-0.08
-0.1

(a)

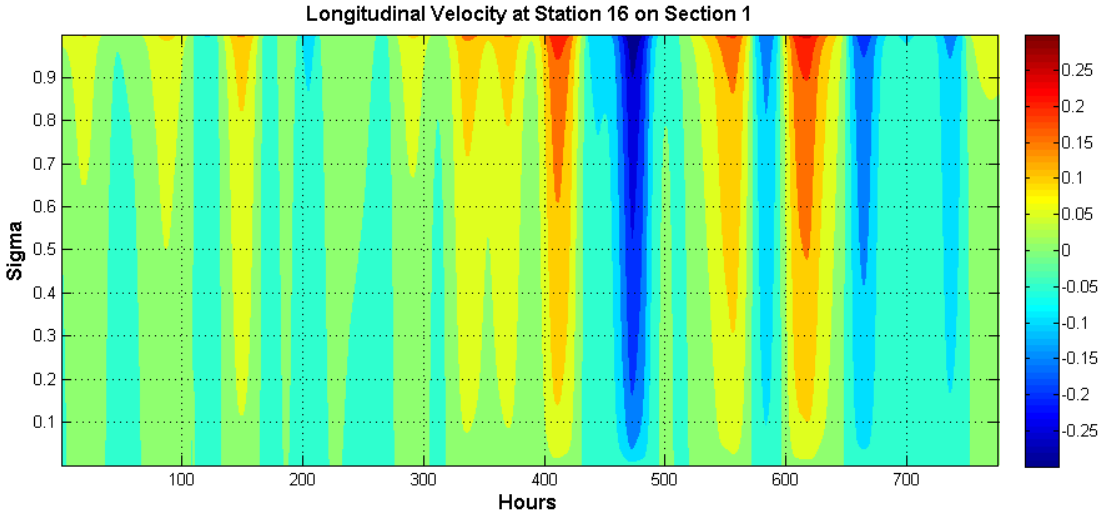
Longitudinal Velocity at Station 16 on Section 1
Sigma
Hours
0.9
0.8
0.7
0.6
0.5
0.4
0.3
0.2
0.1
100
200
300
400
500
600
700
0.25
0.2
0.15
0.1
0.05
0
-0.05
-0.1
-0.15
-0.2
-0.25

(b)

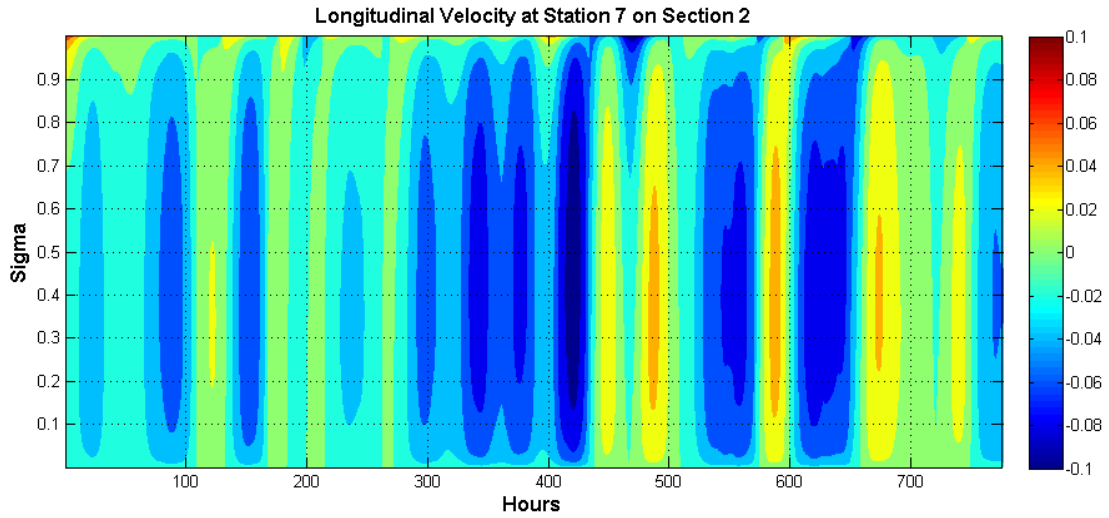


(c)

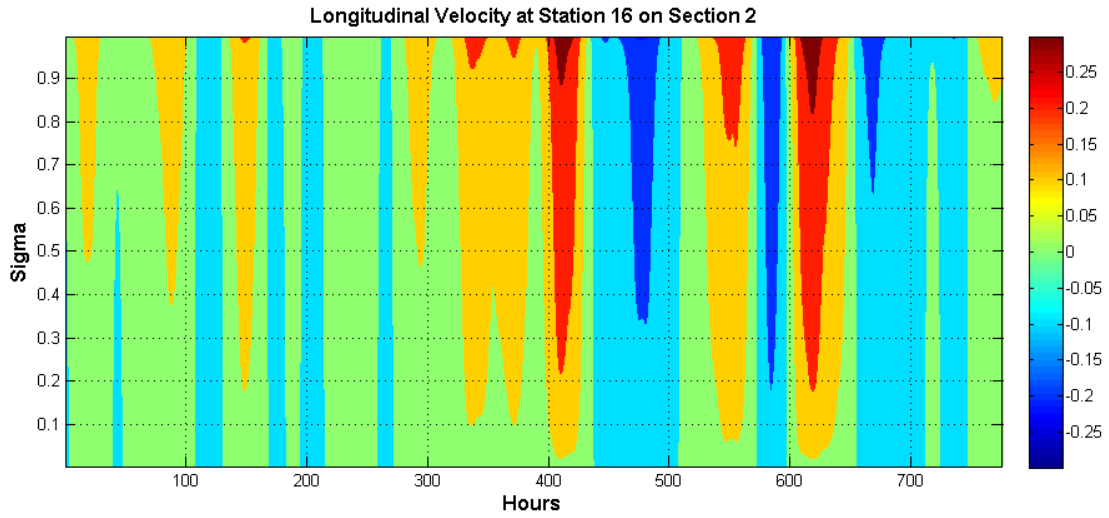


(d)

Figure 3.8 Vertical structures of longitudinal current velocity at station 7, 16 on section 1 (a, b) and station 7 16 on section 2 (c, d)

Section 1 and 2 are two typical sections in central GSB and their responses to wind forcing in different directions characterized the wind-driven longitudinal circulation structure in most area of the lagoon. Without the influence of narrow channel jet, current would be downwind on shallow flanks and upwind over deeper middle area; current sheared vertically above relatively flat bottoms and the shear

occurs primarily within surface and bottom log layers; while in water column on sloping bottoms, vertical current shear diminished but lateral shear became important. The jet from Smith Point generated by extreme wind event around hour 475 modified circulation structure on section 2 and produced an overall downwind flow in middle channel but this case did not happen during the other wind events.

### 3.1.3 Horizontal structure of wind-driven longitudinal circulation in central GSB

Horizontal shear dispersion in longitudinal direction generated by interaction of lateral sheared current and lateral dispersion could be one order higher than vertical shear dispersion (Zimmerman 1986) and its rate could be estimated by the similar method as in vertical shear dispersion calculation with known horizontal structure of depth-averaged longitudinal current (Geyer, Chant, and Houghton, 2008). As briefly mentioned previously, wind driven longitudinal currents were organized by bathymetry characters on two typical cross-sections in central GSB. In this section, wind-driven depth-averaged longitudinal velocity will be analyzed at the spatial scale of the entire central bay.

During the largest westward wind event at around hour475, strong westward currents (0.2 – 0.3 m/s) were observed at most of the southern side where water depth is small (less than 1 meter) except for channels beginning from Fire Island Inlet (15 kilometer and 20 kilometer on x axis) and some part of northern side with

relatively broader shoal. In deep channel in the middle of the bay, weaker (velocity smaller than 0.1 m/s) but wider eastward flow extended through the whole central bay. In middle Bellport Bay a stripe of westward flow was found which originated from a jet through Smith Point channel, and although this flow was countered by the middle channel flow from west of Bellport Bay it still produced a weak westward flow at middle of Section 2 (Figure 3.1, Figure 3.6 lower) where eastward velocity was expected. When eastward wind reached its maximum at approximately hour 620, the longitudinal velocity field had similar structure to previous one with opposite direction. At times when longitudinal winds velocities were zero longitudinal currents became weaker and less organized, but some fingerprints still remained from the closest wind event before. At hour 435 after an eastward storm (Figure 3.10 upper), currents in middle deeper areas got unstructured except channels in Bellport Bay and in the western part north of Fire Island Inlet which are relatively narrow; while most of northern/southern shoals still remained occupied by weak eastward currents. When the longitudinal wind gets slack after a westward event around hour 596 (Figure 3.10 lower), the current structure was similar to the one still forced by the wind (Figure 3-9 upper) except for the much smaller magnitude (smaller than 0.1 m/s). To summarize, the reaction of central GSB to longitudinal winds in either (east- or westward) directions was mainly controlled by the bathymetry: water was transported downwind in areas

with smaller depth and upwind in middle channels; magnitudes of the depth-averaged velocity remained relatively uniform within water columns above flat bottom, while beyond slopes strong lateral shear occurred; during period with weaker or slack winds the current structure still remained similar to the one during the previous one wind event with reduced strength and organization due to inertial of the water but would be dominated by the following wind event.

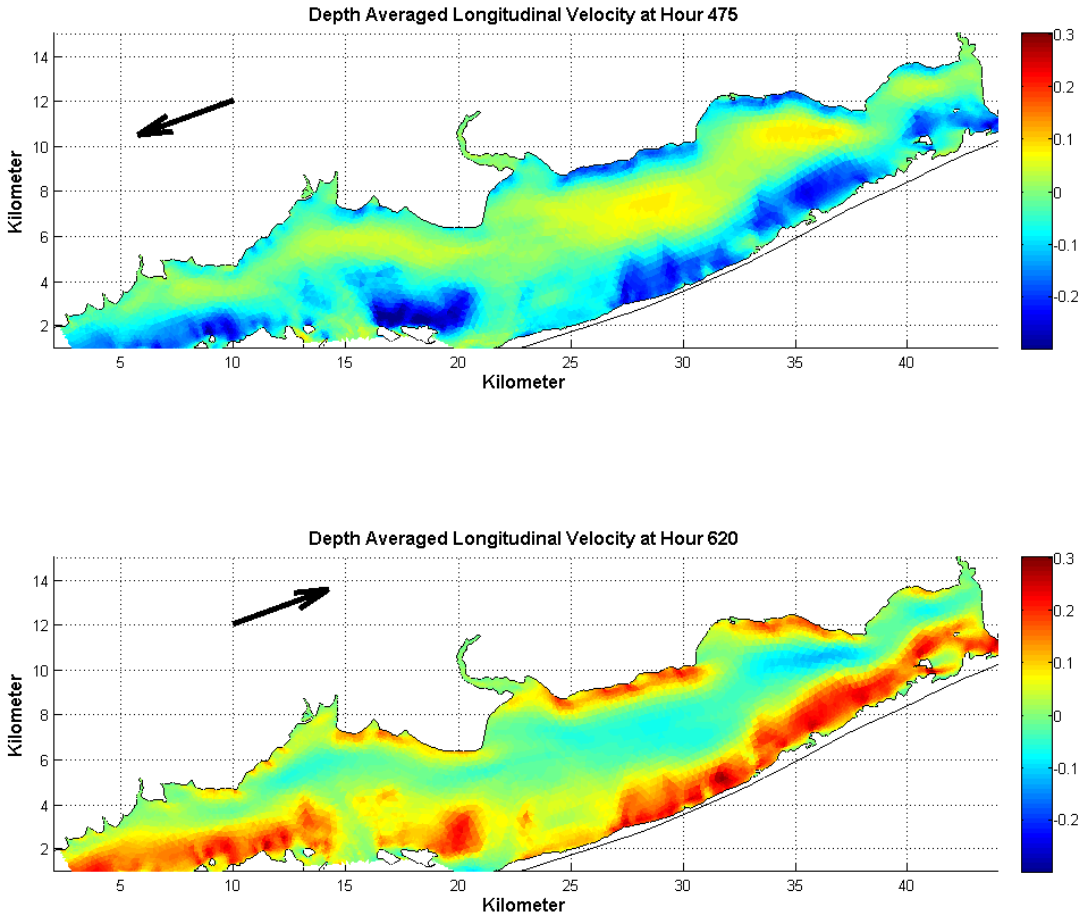


Figure 3.9 Horizontal structure of depth-averaged longitudinal velocity under westward (upper) and eastward (lower) wind forcing

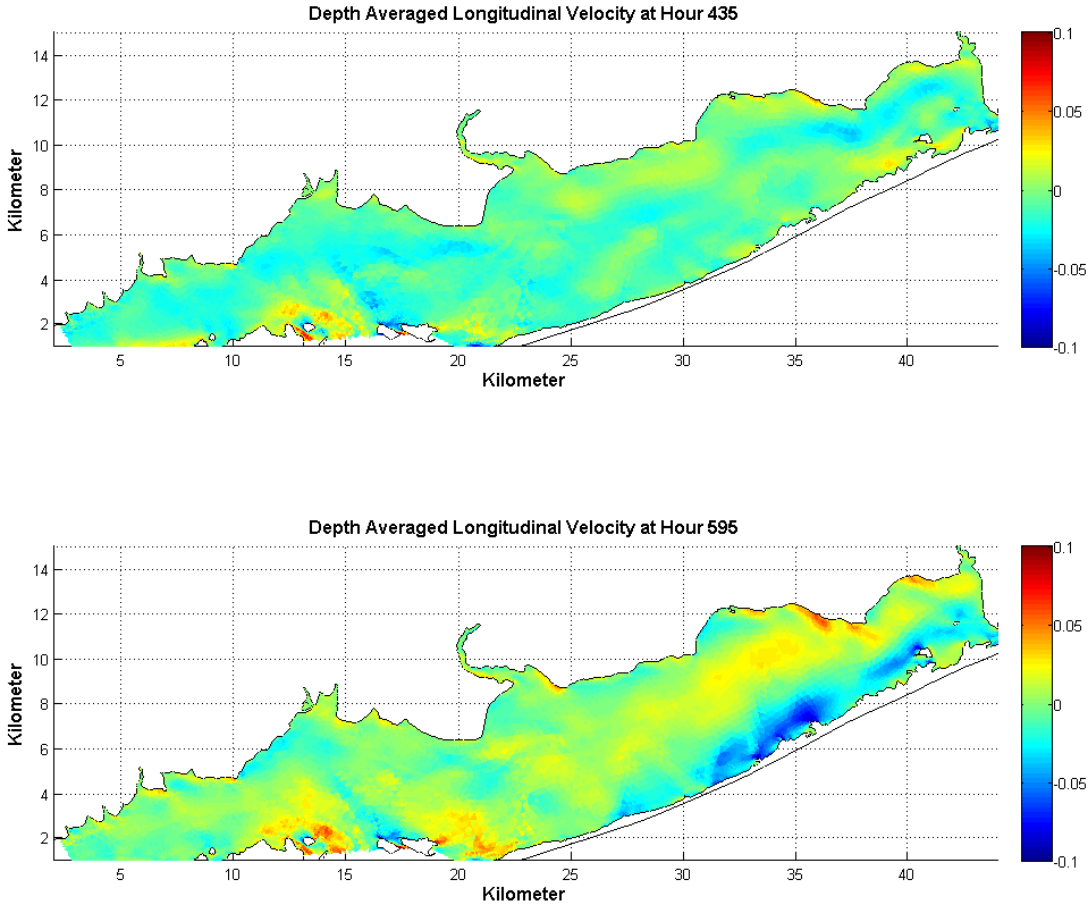


Figure 3.10 Horizontal structure of depth-averaged longitudinal velocity at slack wind time after eastward (upper) and westward (lower) winds

## 3.2 Wind-driven lateral circulation in central GSB

### 3.2.1 Wind-driven lateral momentum balance in central GSB

Similar to equation (3.2), the momentum balance in lateral direction is written as:

$$\frac{1}{H+\eta}\frac{\partial \bar{v}}{\partial t} = -\frac{1}{H+\eta}\int_{-H}^{\eta}(u\frac{\partial v}{\partial x}+v\frac{\partial v}{\partial y}+w\frac{\partial v}{\partial z})dz - g\frac{\partial \eta}{\partial x} - \int_{-H}^{\eta}(\frac{g}{\rho}\int_{z}^{\eta}\frac{\partial \rho}{\partial y}dz)dz + \frac{\tau_{sy}}{\rho(H+\eta)} - \frac{\tau_{by}}{\rho(H+\eta)} - f\bar{u} \quad (3.10)$$

where $\tau_{sy}$ and $\tau_{by}$ are lateral surface and bottom stress normalized by local water depth.

The same cross-sections were selected as in the longitudinal analysis (Figure 3.1, 3.2 and 3.4), and to analyze dynamic processes controlling the lateral circulation in central GSB, time series of momentum terms in lateral direction were calculated based on FVCOM results. On section 1 near the middle channel (Figure 3.12 upper) the most significant terms were still barotropic pressure gradient and surface stress, but another two terms became more important than in the longitudinal case and not negligible: northward baroclinic pressure gradient generated by positive salinity gradient from north to south in the lagoon and Coriolis term produced by longitudinal currents with larger magnitude. The overall magnitudes of lateral momentum terms were smaller than those of longitudinal ones and the momentum balance was more complicated: barotropic pressure gradient balanced with sum of baroclinic pressure gradient plus Coriolis terms most part of the time instead of surface plus bottom stress terms. On the southern shoal (Figure 3.12 lower), magnitude of surface stress terms was magnified due to reduced water depth and so was the barotropic pressure gradient term, and the major momentum balance was similar to its longitudinal counterpart (i.e. between barotropic pressure gradient and surface stress). Coriolis term in this station had larger magnitude than the one in deep channel due to stronger longitudinal currents

but it was still weaker compared with the previous two terms. Lateral salinity gradient was weaker around this station so baroclinic pressure gradient term became weaker than the deep channel one.

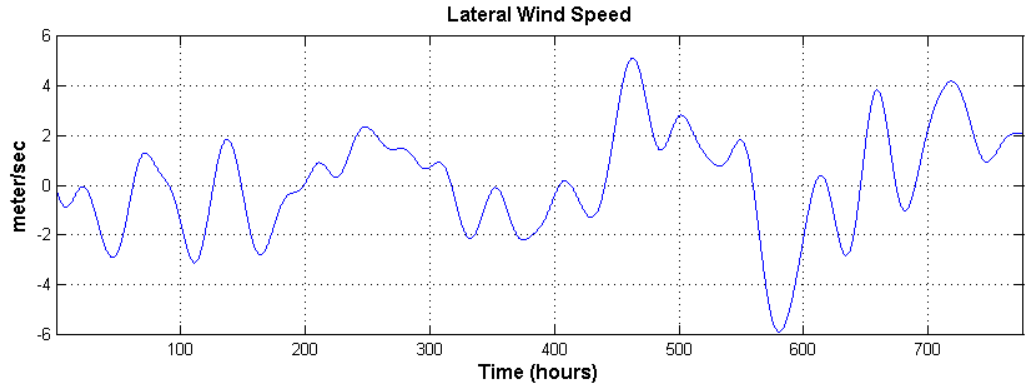


Figure 3.11 Wind speed in lateral direction

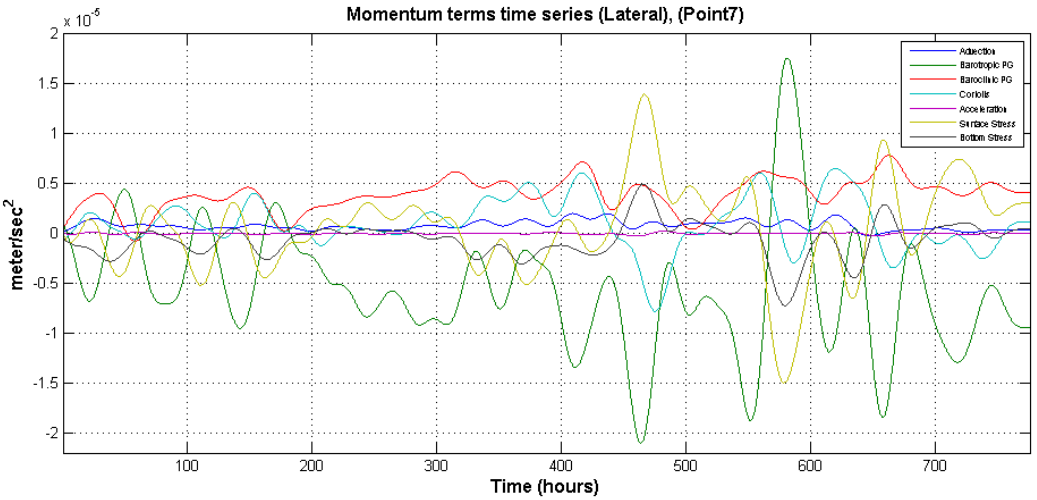

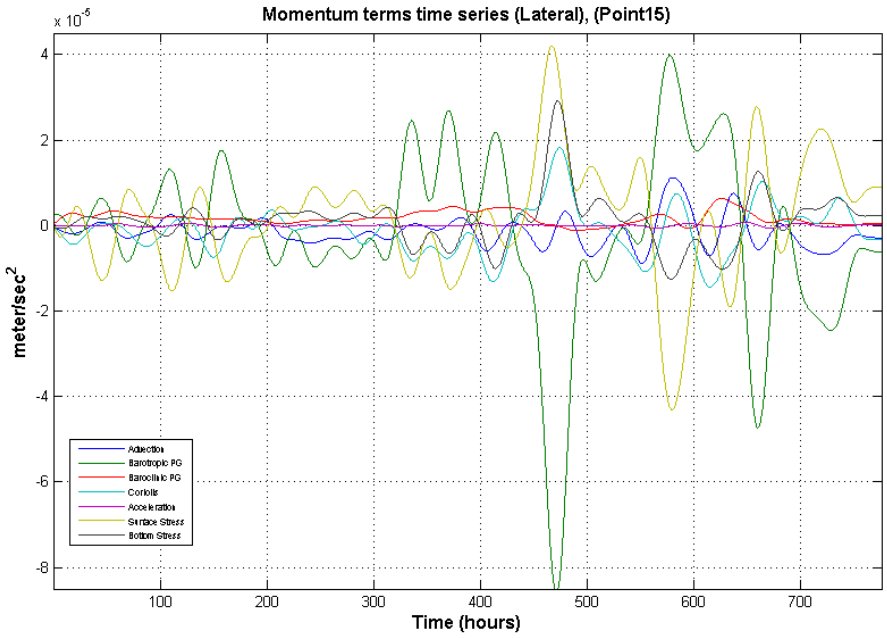


Figure 3.12 Time series of lateral momentum terms at station7 (upper), station 15 (lower) of section 1

At the middle station on section 2 (Figure 3.13 upper) the momentum balance was very similar to the one on section 1: barotropic pressure gradient balanced with Coriolis and baroclinic pressure gradient terms during most of the simulation except when the surface stress term in lateral direction reached its maximum (Figure 3.11) in both positive (northward) and negative (southward) directions. The southern shoal station on section 2 (Figure 3.13 lower) also had similar momentum balance to its section 1 counterpart which was between barotropic pressure gradient and surface stress terms. Both stations on section 2 had stronger momentum terms than those on station 1 due to reduced water depth.

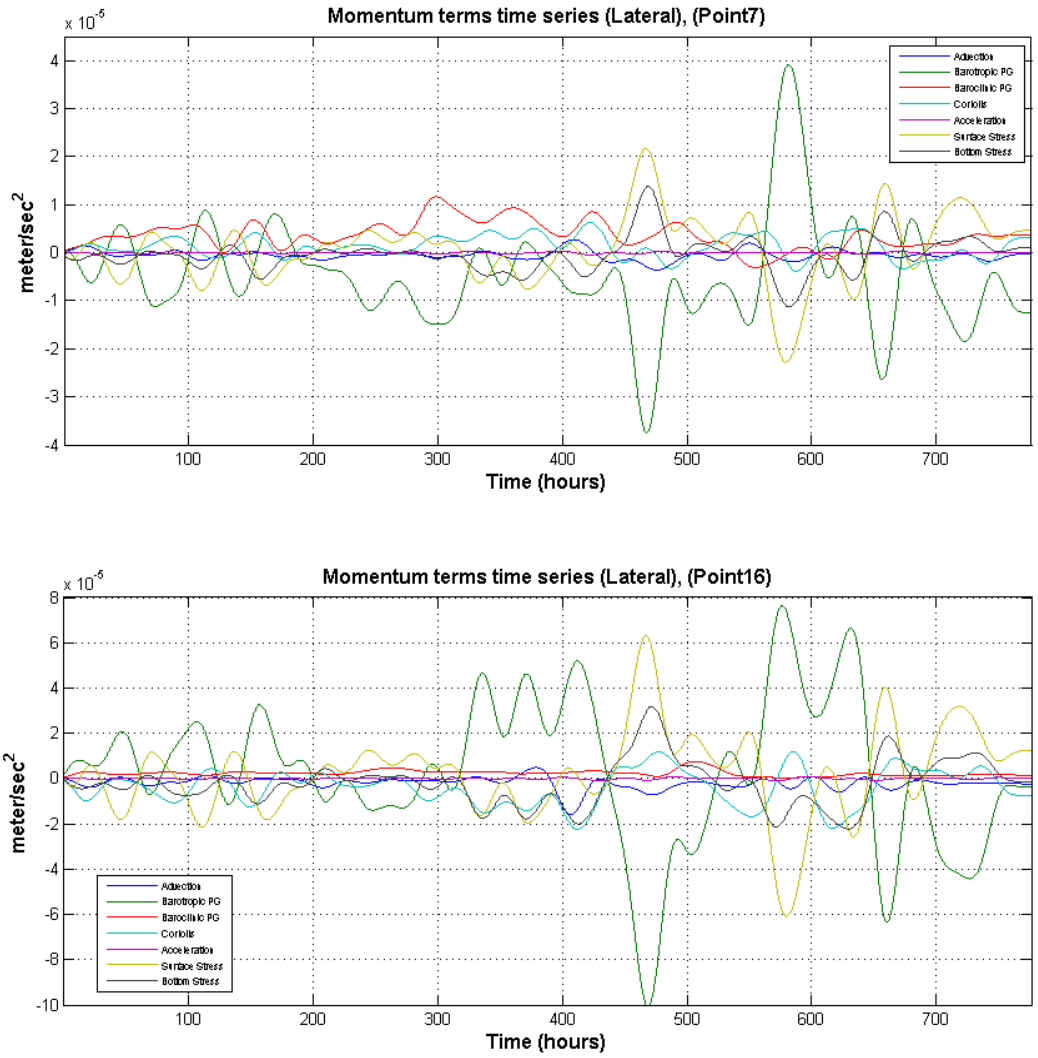


Figure 3.13 series of lateral momentum terms at station7 (upper), station 15 (lower) of section 2

Based on results from the two typical sections, dynamic processes controlled lateral circulation in central GSB in the following two typical patterns: in middle channel areas where large salinity gradient in lateral direction was caused by the encounter of fresh water from Long Island and saltier water from the southern inlets, baroclinic pressure gradient term became important and had similar magnitude as barotropic pressure gradient, thus in these area the sum of baroclinic

pressure gradient and Coriolis terms balanced barotropic pressure gradient term when wind forcing was weak; on southern shoals salinity gradient decreased substantially while surface stress term was larger due to the reduced water depth so that the lateral momentum balance was between barotropic pressure gradient and surface stress terms, similar to the longitudinal one.

### 3.2.2 Vertical and horizontal structures of wind-driven lateral circulation in central GSB

Momentum balance of circulation in shallow water was between barotropic pressure gradient and surface stress terms, and the local acceleration is small. For circulation structure in middle deeper areas, on the other hand, although the Coriolis effect and baroclinic pressure gradient cannot be ignored, the ADCP observation (Figure 1.7) suggested the vertical structure of lateral velocity was similar with the one of longitudinal velocity except for smaller magnitude. Thus equations (3.3, 3.5 – 3.8) would still form a proper model for the vertical structure of lateral circulation in central GSB.

At hour 463 with the maximal northward wind (Figure 3.11) the lateral circulation patterns (Figure 3.14) on both sections 1 and 2 were in a two-layer form: a downwind northward surface flow and an upwind southward bottom flow. On section 1 the vertical shear of lateral velocity was uniform in most locations, and from the surface to about 2.5 meter depth, the velocity varied from 3 cm/s to -1.5

cm/s. On section 2 the lateral velocity had a larger vertical gradient: it varied from 3 cm/s to -3 cm/s within 0.5 meters.

The lateral circulation at hour 581 (Figure 3.15) under the maximal southward wind event also had an approximately two-layer structure on both sections, and with reversed directions in both layers.

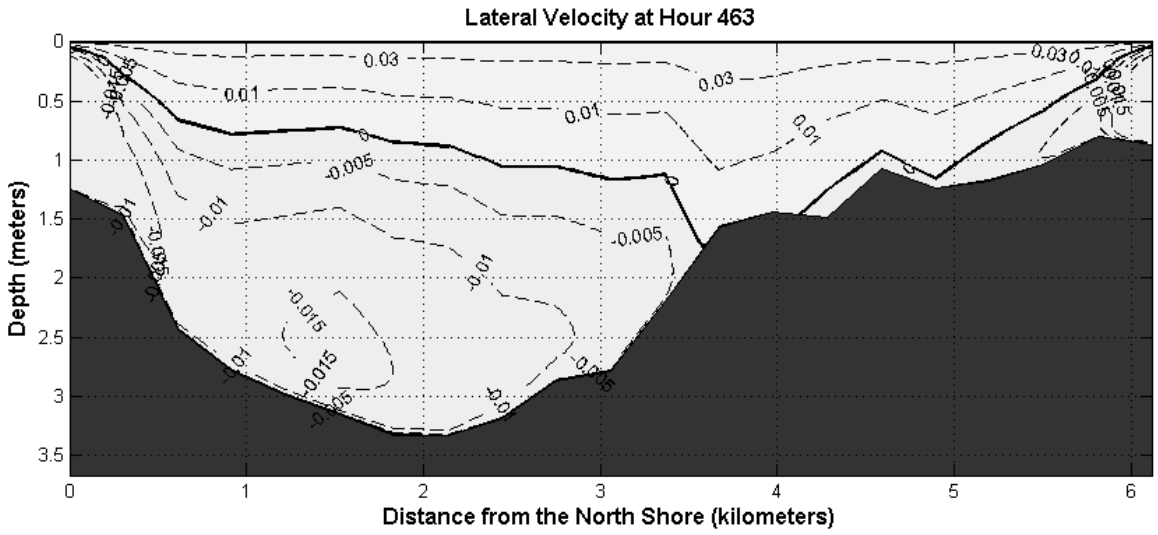

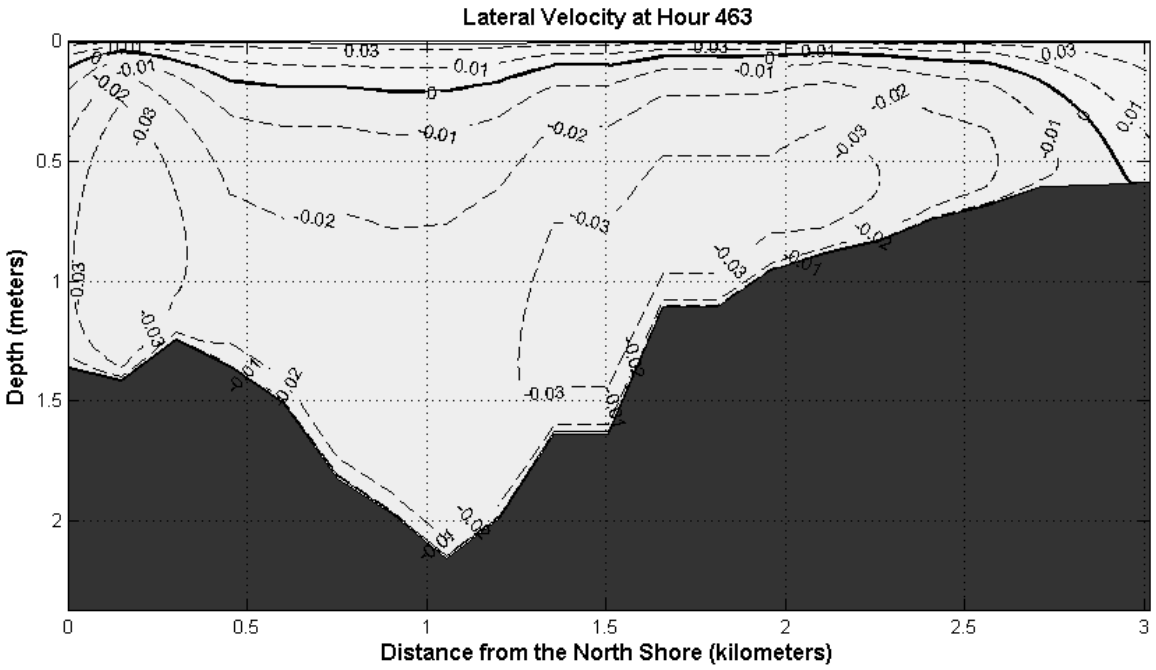


Figure 3.14 Lateral current velocity on section 1 (upper) and 2 (lower) at Hour 463

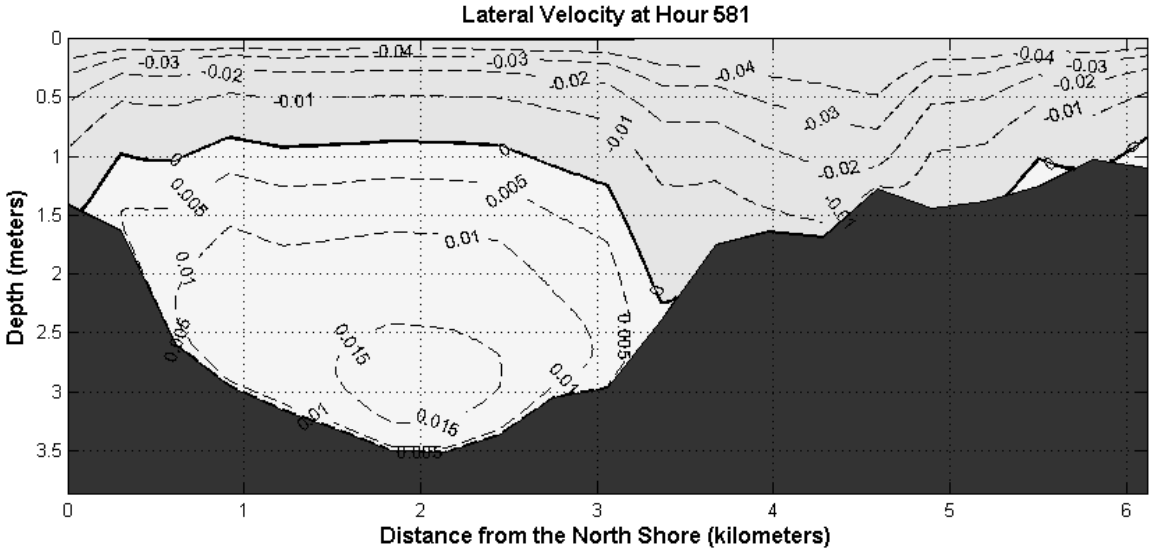

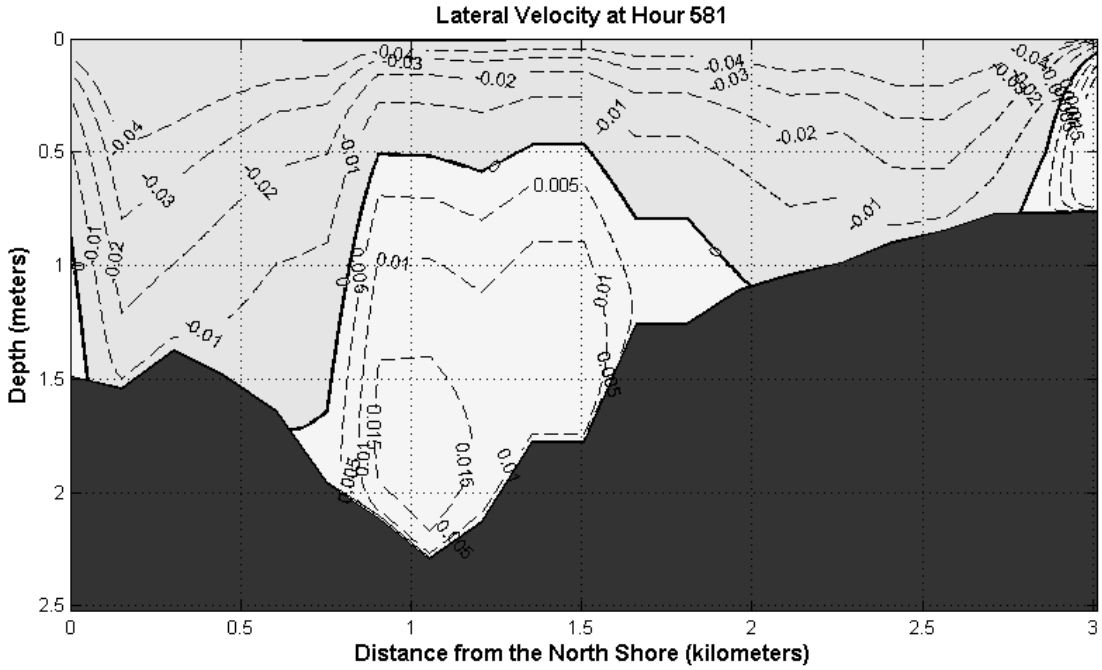


Figure 3.15 Lateral current velocity on section 1 (upper) and 2 (lower) at Hour 581

Horizontal structure of depth-averaged lateral current velocity at maximal northward (hour 463) and southward (hour 581) wind events are shown in Figure 3.16. Unlike the longitudinal currents (Figure 3.9), the lateral currents were less organized and multiple small-scale structures existed along the longitudinal direction. But when comparing the structures under the two distinct wind conditions, it was observed that they were generally opposite with each other, that is, at the same location, current direction reversed with the wind direction. Thus the synoptic-scale currents in lateral direction were determined by the interaction of wind forcing and location bathymetry characters.

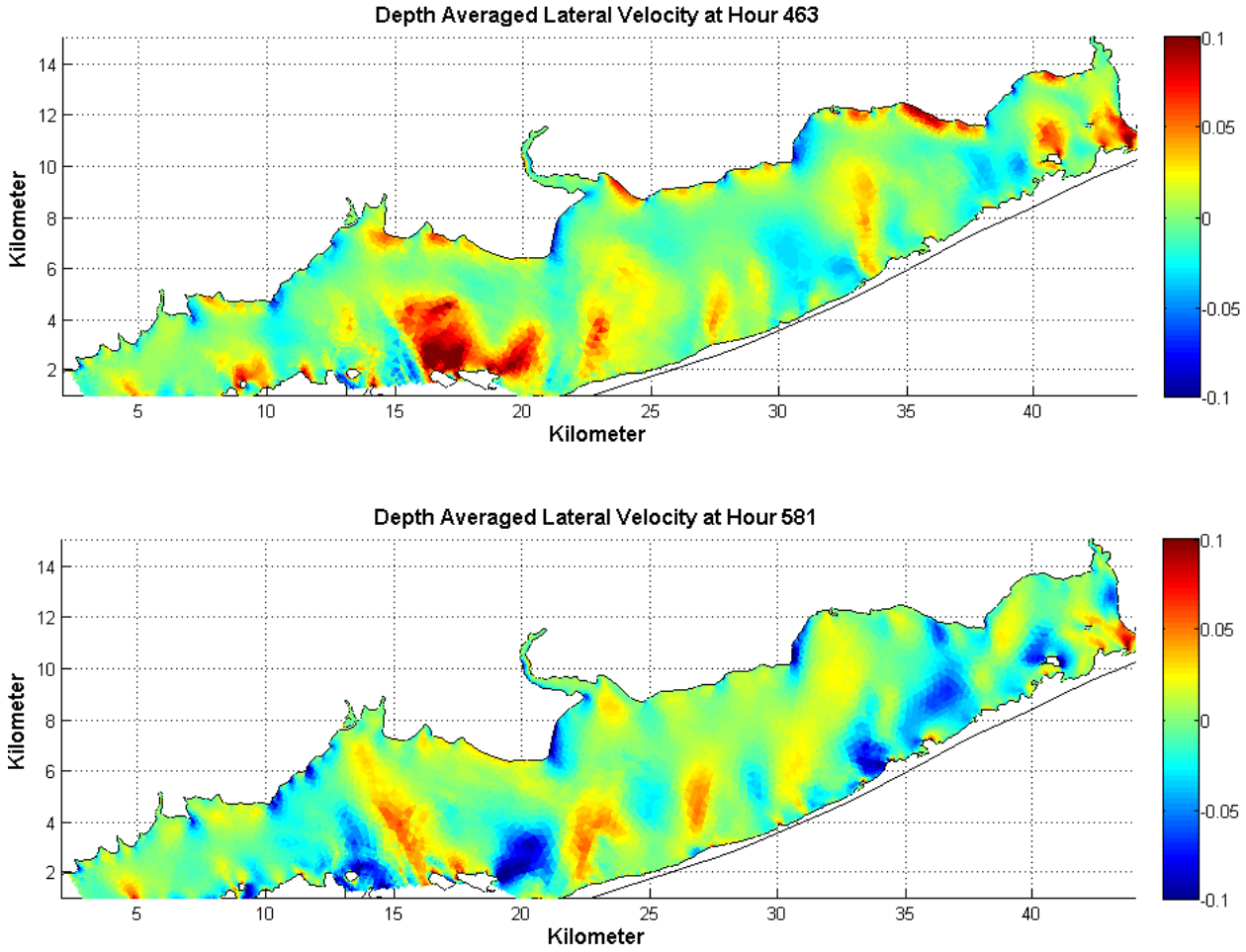


Figure 3.16 Horizontal structure of depth-averaged lateral velocity under northward (upper) and southward (lower) wind forcing

## 3.3 Vorticity analysis of residual circulation in GSB

Vertical vorticity analysis was applied on the depth-averaged velocities at the synoptic scale:

$$\frac{\partial \varsigma}{\partial t} = \frac{g}{2\rho}\nabla\rho\times\nabla H + \{\frac{\partial}{\partial x}(\frac{\tau_s^y}{\rho H}) - \frac{\partial}{\partial y}(\frac{\tau_s^x}{\rho H})\} - \{\frac{\partial}{\partial x}(\frac{\tau_b^y}{\rho H}) - \frac{\partial}{\partial y}(\frac{\tau_b^x}{\rho H})\} + f\cdot\nabla\vec{u} \quad (1)$$

where the vorticity tendency on the left hand side is generated by baroclinicity (interaction between density gradient and bathymetry), surface wind stress curl,

bottom stress curl, and the Coriolis effect on the right hand side. Divergence of the velocities was small so the Coriolis effect was ignored in the analysis, and all the other terms were calculated for different wind scenarios.

During a westward wind event (hour 437 to 516, figure 3.3), the residual depth-averaged circulation was downwind to the west in shallower northern and southern shoals and upwind to the east in the middle deep channel (figure 3.17 upper), and this circulation pattern produced a vertical vorticity pattern positive in the northern part and negative in the southern part of the central GSB (figure 3.17 middle). The depth-averaged salinity during this time period (figure 3.17 lower) illustrated the circulation pattern with lower salinity on the shoal areas and relatively higher salinity in the middle caused by the inlet water intrusion (from Fire Island Inlet to about 30 km area). Close to the northern boundary, the relatively strong positive vorticity was mainly caused by the lateral shear of currents in this area, and in areas to the south of the mid-line of the lagoon, the large negative vorticity was associated with the anti-cyclones. Analysis of equation (1) based on the numerical simulation results revealed that during westward wind, the surface wind stress curl was the single dominant contributor to the vorticity of velocity (figure 3.18), due to the lateral gradient in water depth, the westward wind generated a wind stress curl that was generally positive on the northern part of GSB and negative on the southern part. Baroclinicity term had an

order approximately 1/5 as the surface wind stress curl, while the bottom stress was more than two orders smaller, so the sum of these three terms had the characters mainly from the surface wind stress curl, and this total effect had similar pattern as the residual depth-averaged velocity curl field during the same time period, thus the circulation structure could be explained by the influence of wind forcing.

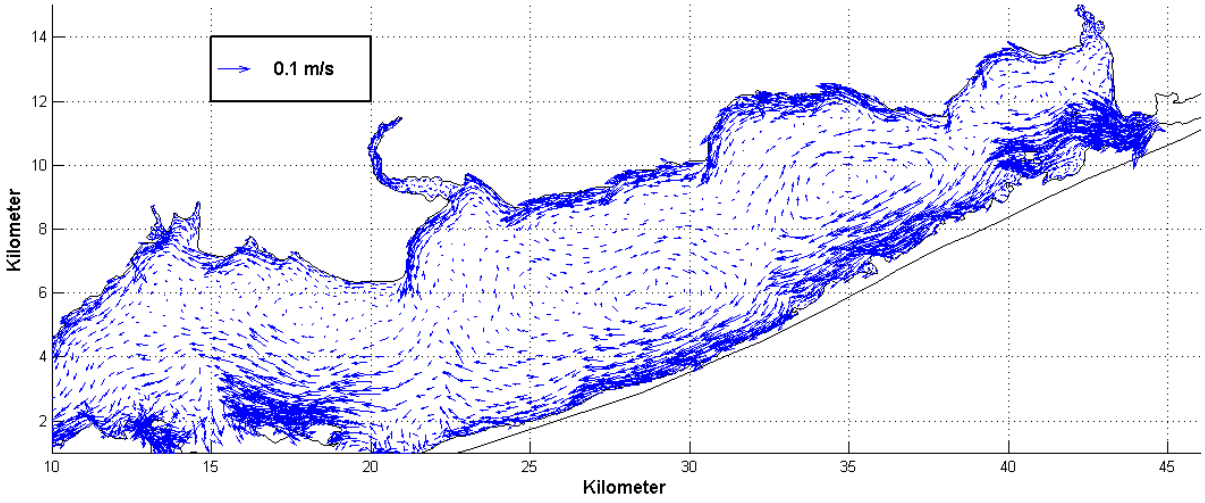


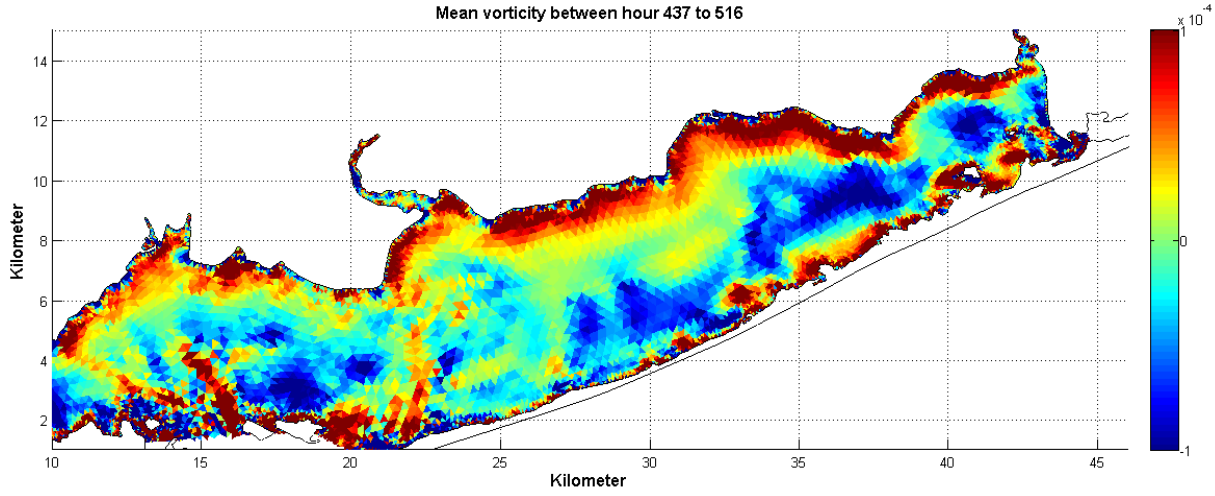

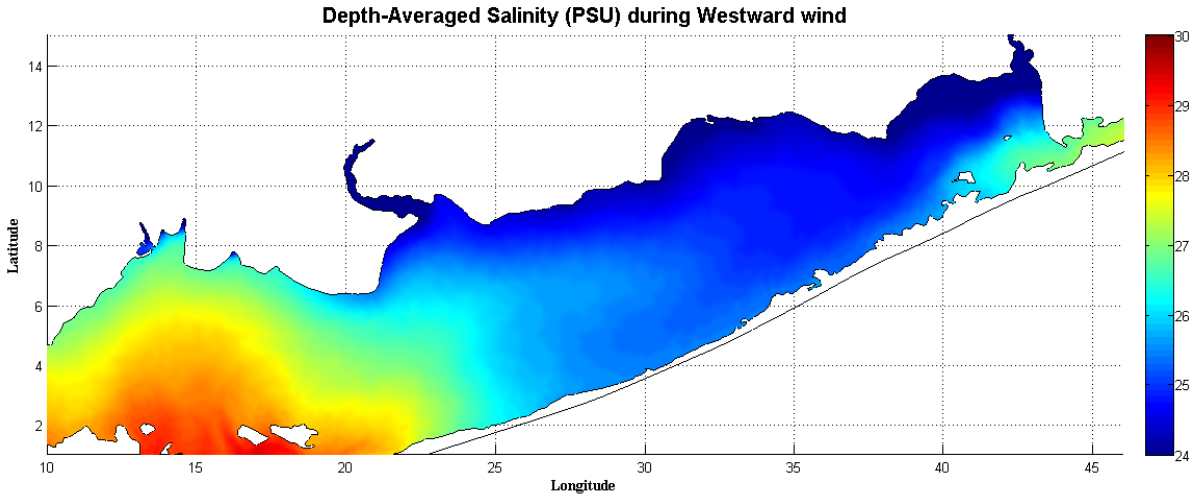


Figure 3.17 Depth-averaged circulation (upper) during westward wind event and the vorticity (lower)

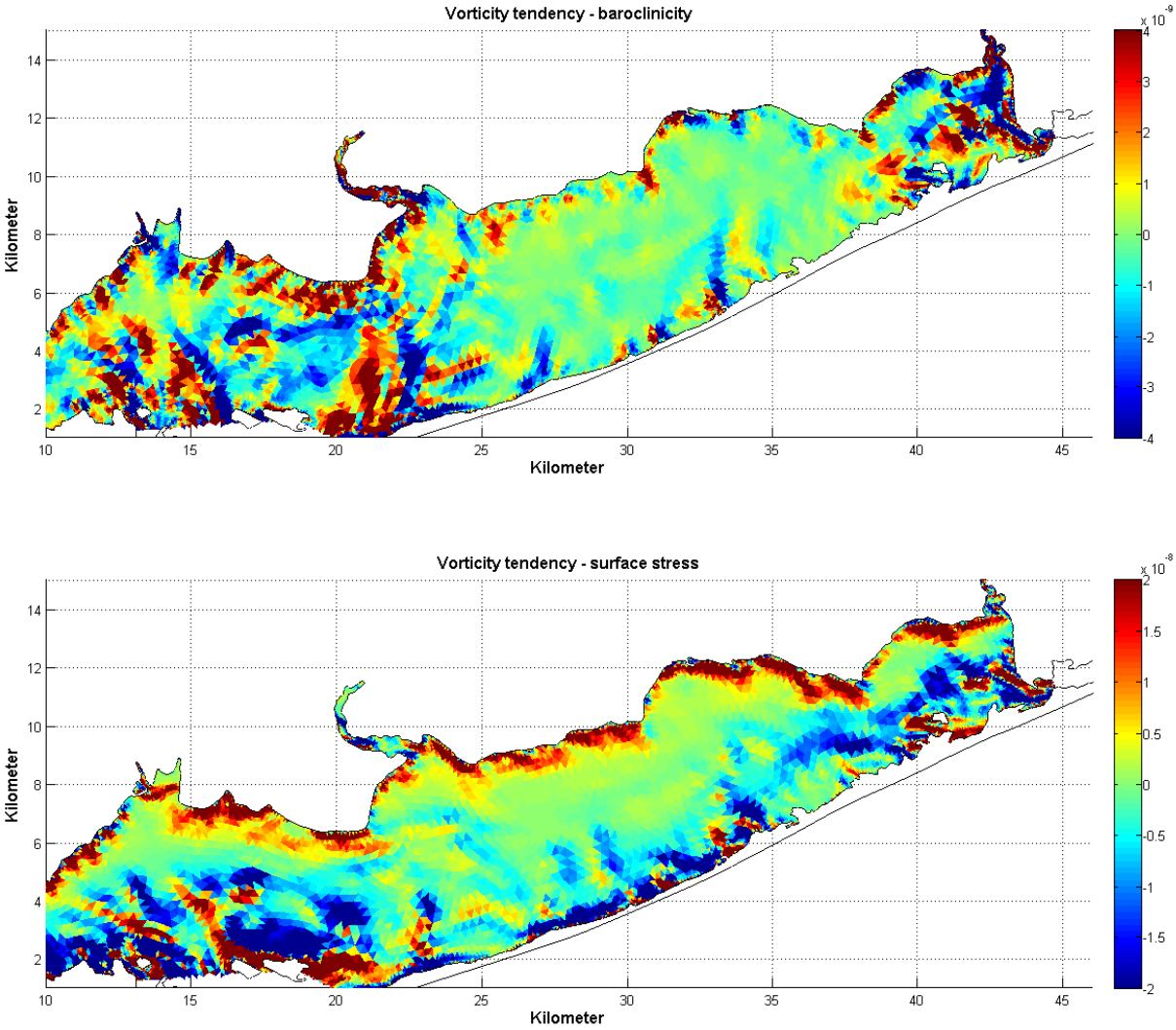

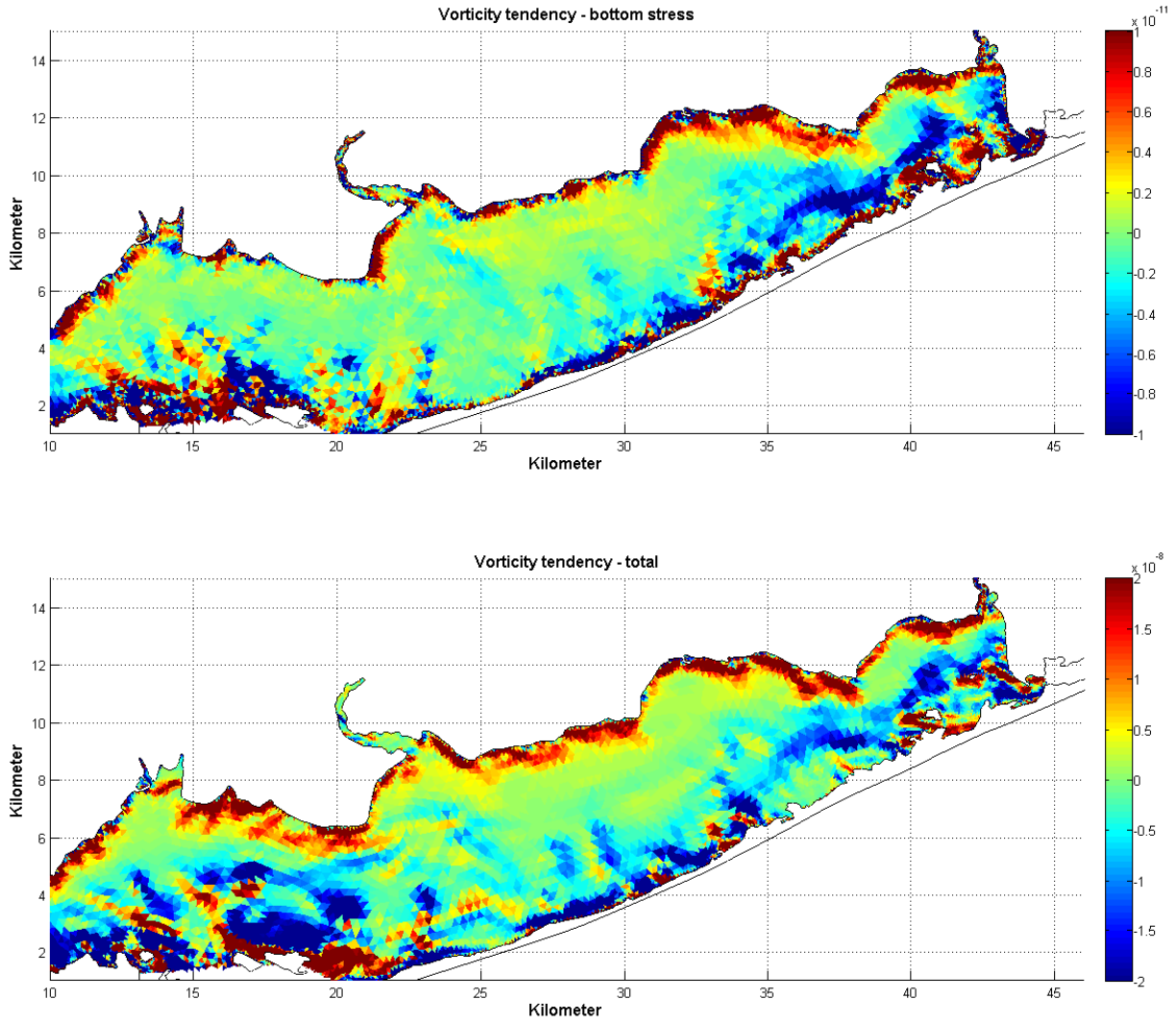


Figure 3.18 Vorticity tendency generated by baroclinicity, surface wind stress, bottom stress, and total effects of the 3 terms during a westward wind event

During an eastward wind event (hour 516 to 577), the residual depth-averaged circulation had a similar pattern as the previous one but with opposite direction (figure 3.19 upper), thus the associated vertical vorticity was generally negative in the northern part and positive in the southern part of the lagoon (figure 3.19 middle). The higher value of depth-averaged salinity on the southern shoal verified the eastward downwind flow in this area, and the low salinity on the

northern shoal was caused by the eastward transport of freshwater from Long Island (figure 3.19 lower). Also similar to the previous case, the vorticity tendency generated by the surface wind curl was much larger than the other two terms in magnitude and the total effect of all the three term had similar pattern as the one produced by the surface wind and also as the depth-averaged velocity curl field (figure 3.20), thus the circulation during the eastward wind event could also explained by the wind forcing.

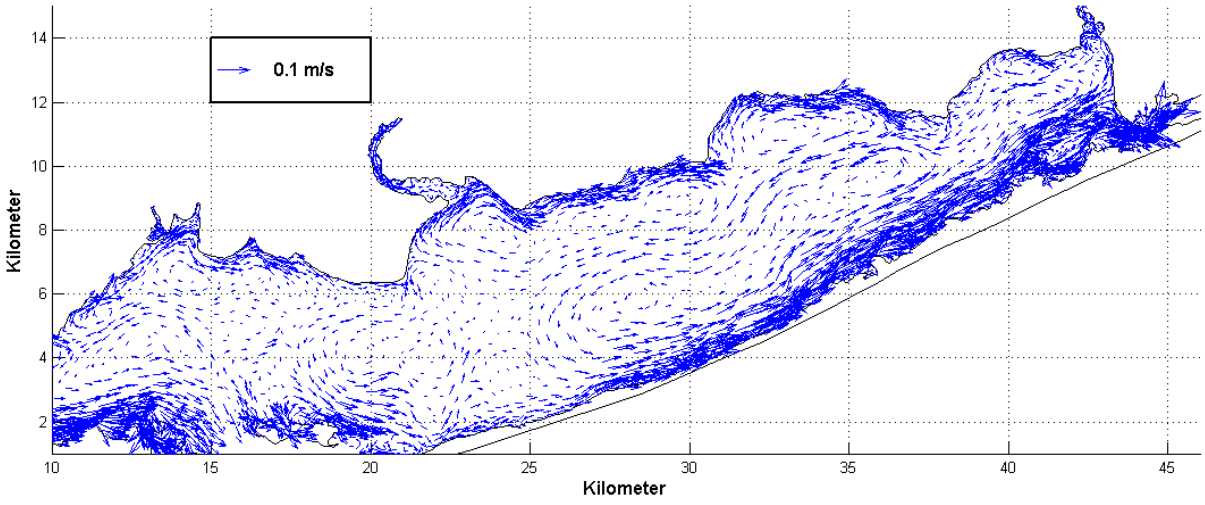

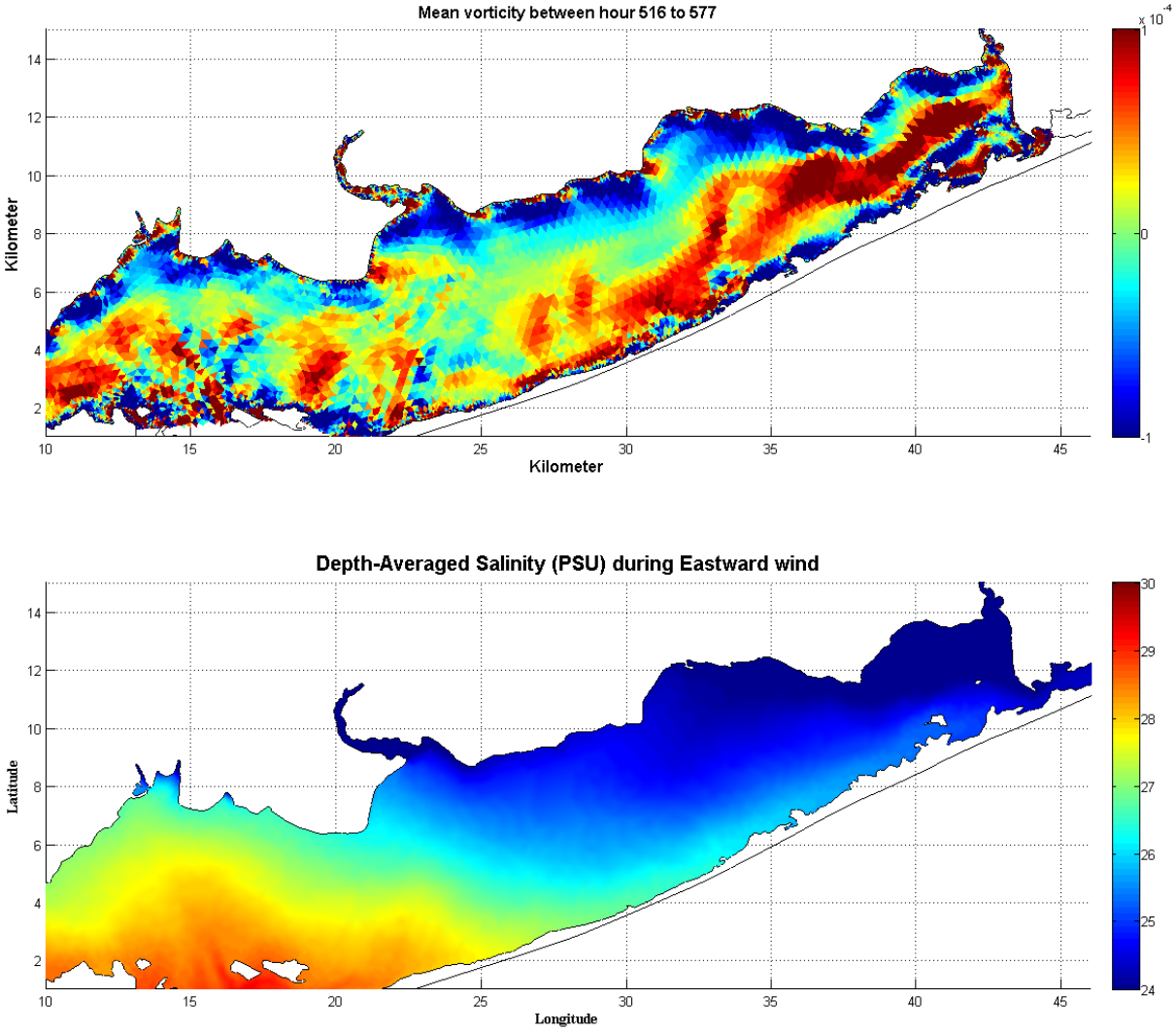


Figure 3.19 Depth-averaged circulation (upper) during eastward wind event and the vorticity (lower)

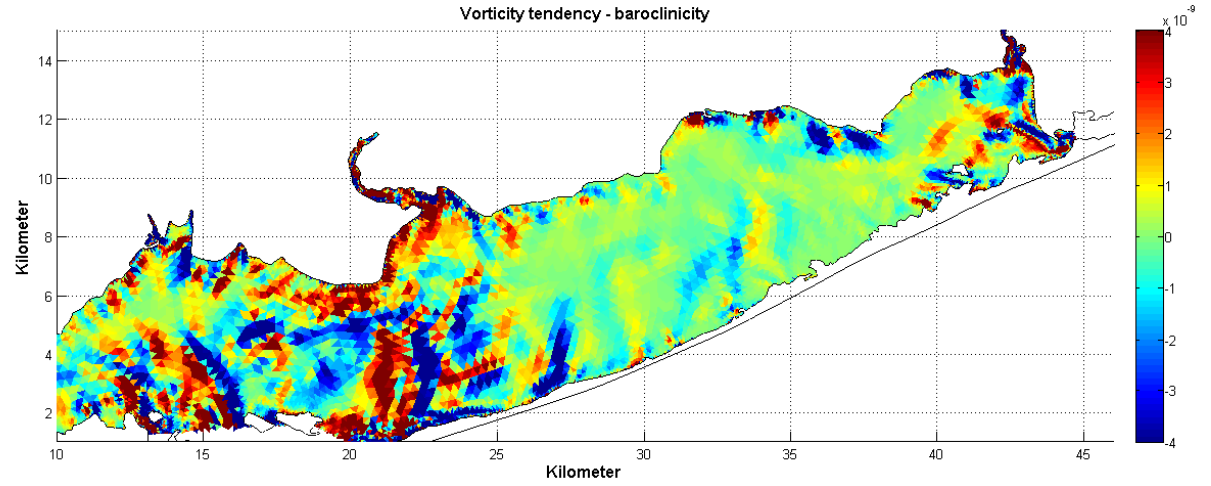

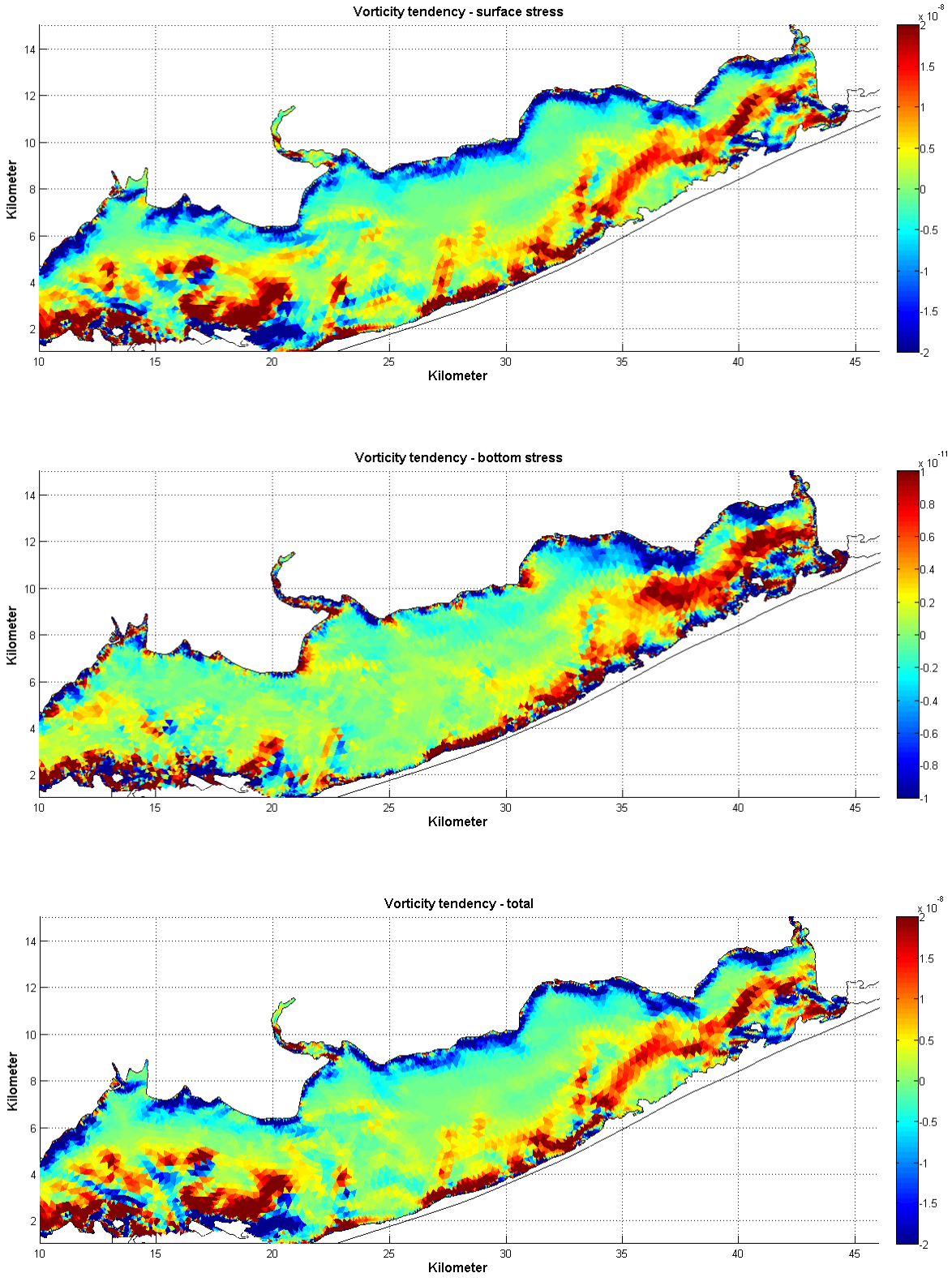


Figure 3.20 Vorticity tendency generated by baroclinicity, surface wind stress, bottom stress, and total effects of the 3 terms during an eastward wind event

When considering a longer period including equal number of eastward and westward wind events, such as hour 437 to 648 during which two eastward and westward wind occurs (figure 3.3), the residual depth-averaged circulation became weaker and the associated vorticity field got not only weaker but less organized than the cases with single-direction winds (figure 3.21). Analysis of terms in equation (1) based on the numerical simulation (figure 3.22) showed that although the surface wind stress curl had characters similar to the eastward wind case due to the eastward time-averaged wind forcing, the magnitude was 1 order smaller than the ones in the wind cases because of the existence of winds in opposite directions. Baroclinicity term had similar magnitude as in previous cases; it was comparable to the wind stress curl in the eastern half of the lagoon (east to kilometer 30) and was stronger than the wind stress term in the western half. The bottom stress term was still weak enough to be ignored, thus the total effect of all the 3 terms was determined by both wind forcing and baroclinicity. When comparing the total vorticity tendency to the velocity curl, the patterns were similar to each other in the eastern part, but were different in other areas. Given the relatively small magnitude of total vorticity tendency, its contribution was not significant enough to be seen from the residual velocity curl field and the existing velocity curl pattern at the beginning of the period (hour 437) might be more important.

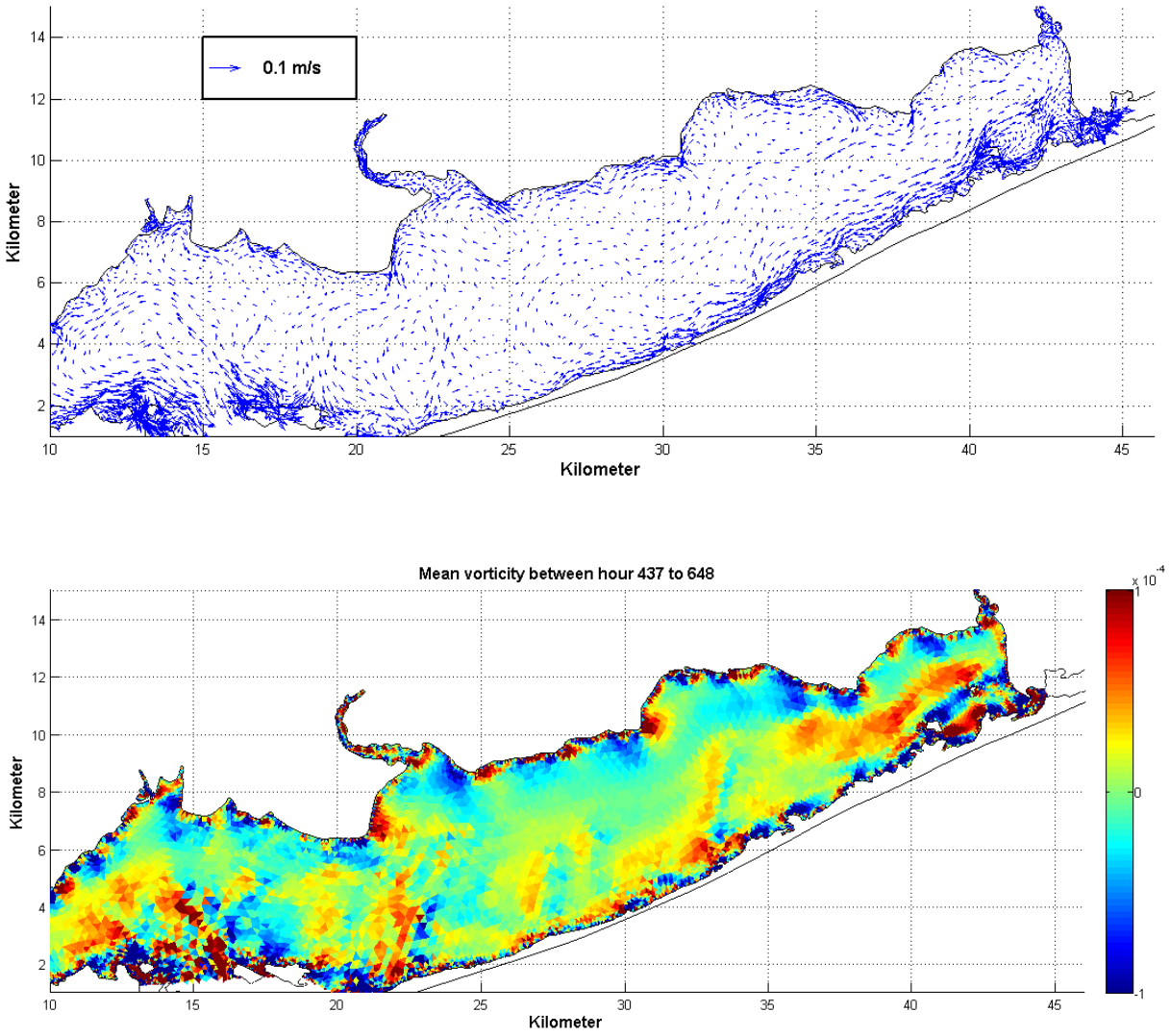


Figure 3.21 Depth-averaged circulation (upper) during hour 437 to 648

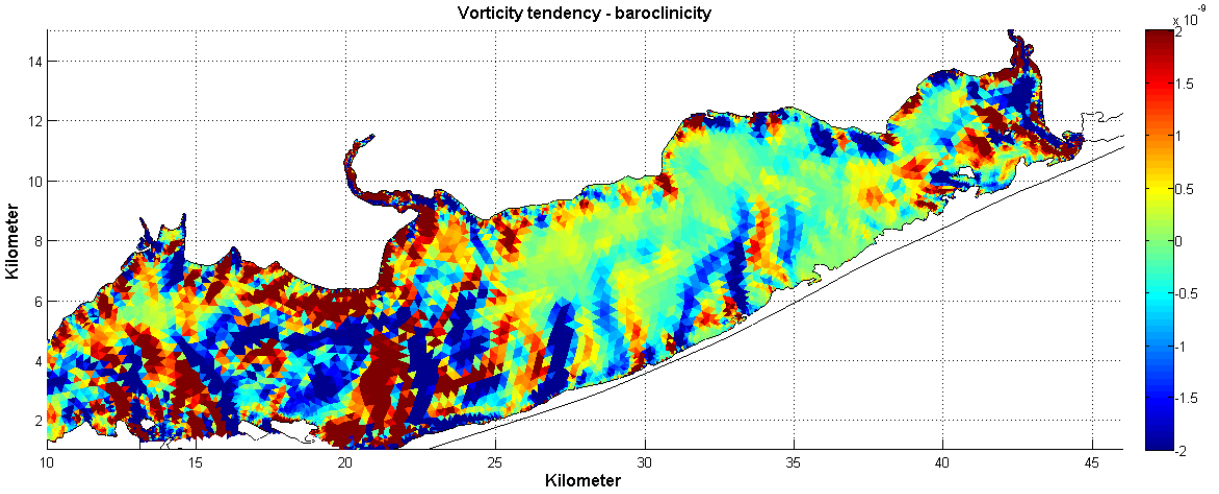
Vorticity tendency - baroclinicity
Kilometer
Kilometer
x 10^-9

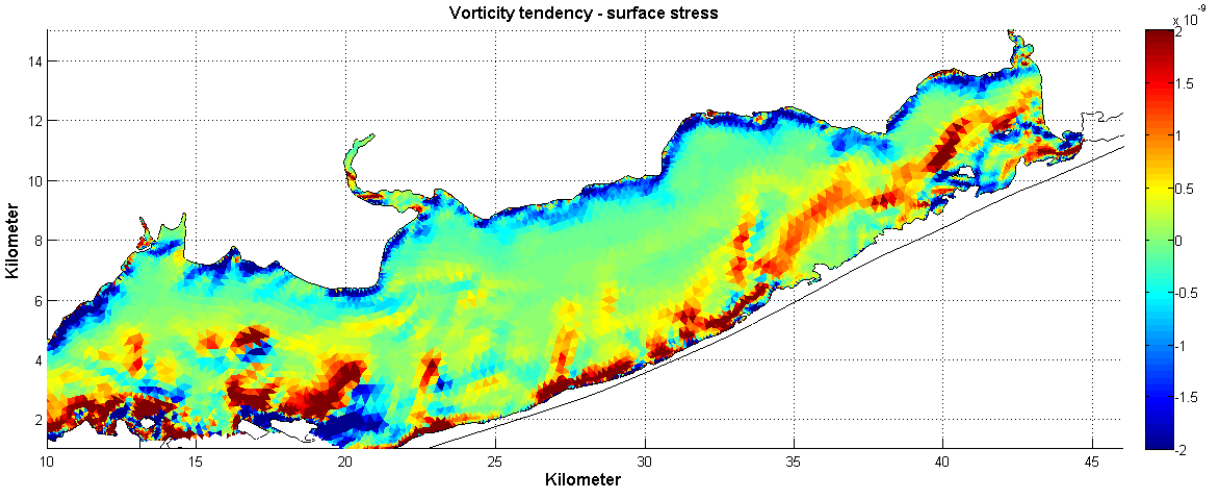
Vorticity tendency - surface stress
Kilometer
Kilometer
x 10^-9

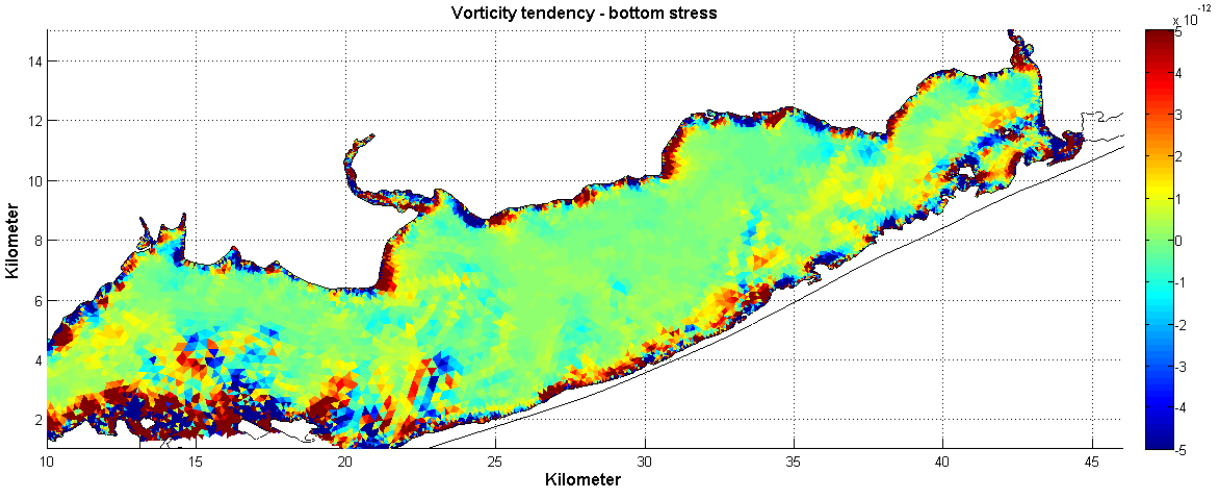
Vorticity tendency - bottom stress
Kilometer
Kilometer
x 10^-12

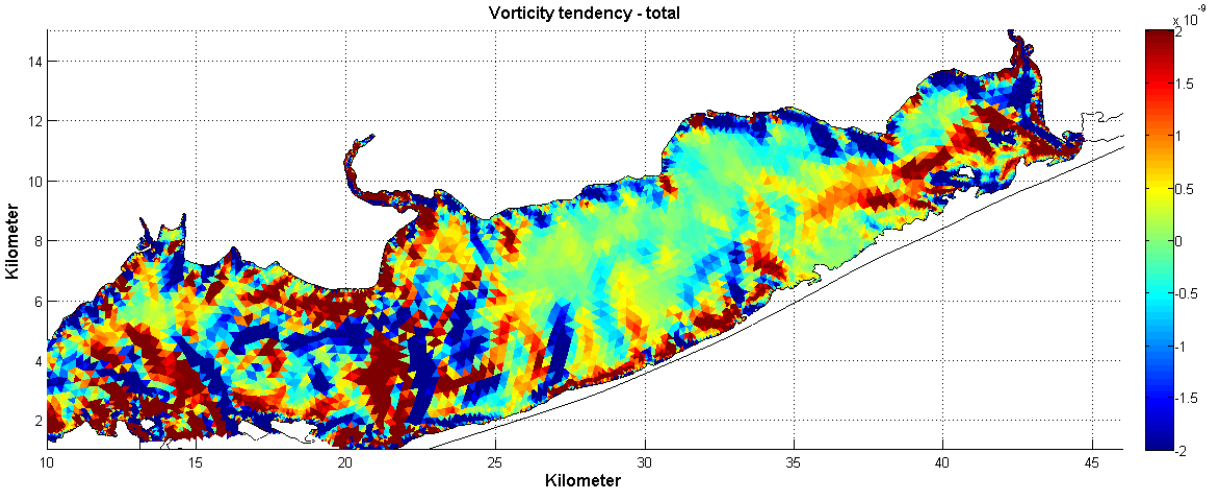


Figure 3.22 Vorticity tendency generated by baroclinicity, surface wind stress, bottom stress, and total effects of the 3 terms during hour 437 to 648

## 3.4 Summary

Results from FVCOM simulation were used to analyze the structure of circulation at both synoptic and long-term residual time scales within GSB. Circulation in the interior of GSB is primarily wind-driven. Dynamics controlling the longitudinal and lateral circulation were examined by momentum diagnostics. At synoptic periods, the longitudinal momentum balance involved primarily barotropic pressure gradient and stress divergence; baroclinic pressure gradient and Coriolis force also contributed to the lateral momentum balance. Vertical current structures in both longitudinal and lateral directions were studied by simple model involving surface and bottom log layers and a linear stress profile within the interior of the water column. Longitudinal currents were highly sheared laterally with maximum shear occurring over strong bottom slopes between the channel and

shoals. Lateral currents were less organized and the direction reversed over short distance along the longitudinal direction. Vorticity analysis also shows that the surface wind stress (barotropic pressure gradient) controls the circulation pattern in GSB during wind events at both eastward and westward directions. For longer period when the time-averaged wind is weak, baroclinicity term has similar magnitude as the wind stress, and the residual circulation pattern is determined by both the total vorticity tendency and the initial state.

# Chapter 4 Horizontal Dispersion in Central GSB

## 4.1 Particle experiments

By using the Lagrangian particle tracking model, four patches of particles were released to different locations in central GSB (Figure 4.1). Each patch covered an area of 300 m by 300m in a 10 m by 10 m resolution at all the 5 sigma layers of FVCOM, so the total amount of particles in each patch was 4500. Start time for all simulations was hour 435 which is at the beginning of a northwestward wind event (Figure 3.3 and 3.11); the end time was around hour 652 and this time period of 217 hours contained two eastward and two westward wind events.

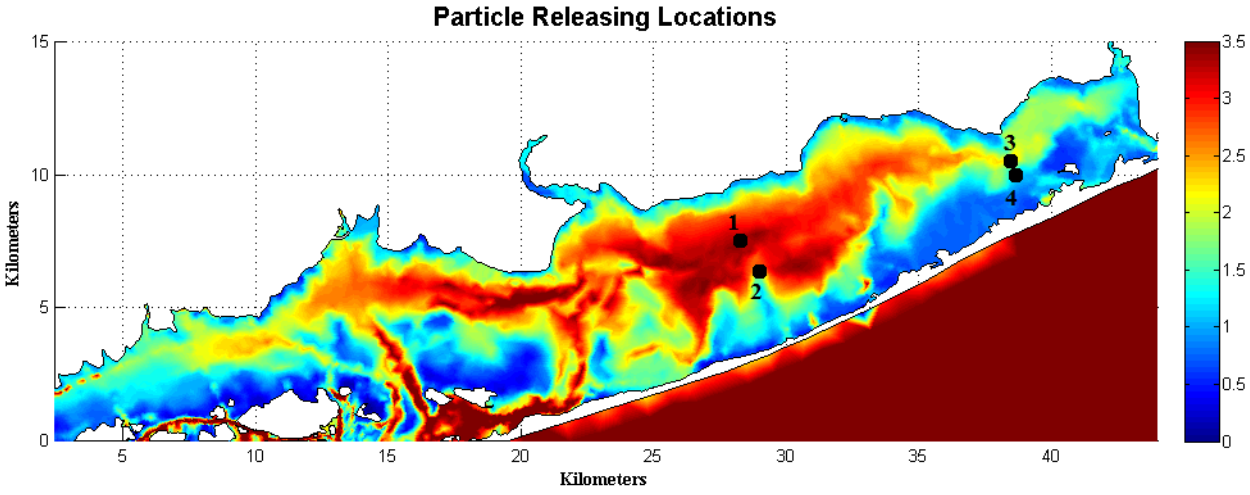


Figure 4.1 Releasing locations of particle patches

The first particle patch (Figure 4.2) spread fast in longitudinal direction during the first 12 hours after release and the length grew to over 4 km in this direction; while in the lateral direction the patch's size increased only slightly.

After another 24 hours (36 hours after release), length of the patch almost kept unchanged in longitudinal direction but expanded to about 1.5 km in lateral direction for the major body of the patch; more noticeable was that the eastern end of the patch was stretched towards south and made its overall lateral coverage to approximately 3 km. During the following day (to 60 hours after release), the patch kept being stretched in both longitudinal and lateral directions, but little lateral mixing occurred at the same time so the patch was still in the shape of narrow belt. Process of horizontal dispersion became more significant from 60 to 108 hours after release, and during this time areas covered by the patch increased quickly although the longitudinal and lateral lengths does not change much. Afterwards (displayed by snapshots at 156 and 204 hours after release), size of the expanded patch grew relatively slowly but steadily in longitudinal direction and finally got restricted in lateral direction by the lagoon's bathymetry.

The second patch (Figure 4.3) was released approximately 1 km south to the first one, and different from the deep and flat bottom around the first release, this one had an initial position above a sloping bottom where the currents shear considerably in the lateral direction (Chapter 3). During the first 12 hours after release, the patch developed to about 3 km in longitudinal direction and 1 km in lateral direction. In the following 24 hours the patch's east and west ends extended in different directions laterally, and were driven by the sheared longitudinal

currents to form a distorted shape with unchanged longitudinal length and increased lateral length. The patch was stretched in both directions and after 60 hours since the release, the patch formed a belt-like shape similar to the first patch at the same time, so during the remaining simulation, the spread of patch 2 followed a pattern similar to the one of patch 1.

Patch 3 (Figure 4.4) was released in the middle deep channel on section 2 near Bellport Bay, approximately 10 km away from the first 2 patches on section 1. Despite the long distance and the fact that the overall water depth around section 2 was shallower than the one near section 1, the third patch developed in similar pattern to patch 1 and 2: spreading in longitudinal direction during the first 12 hours, followed by stretching of both ends in lateral direction before the steady horizontal dispersion in both longitudinal and lateral directions.

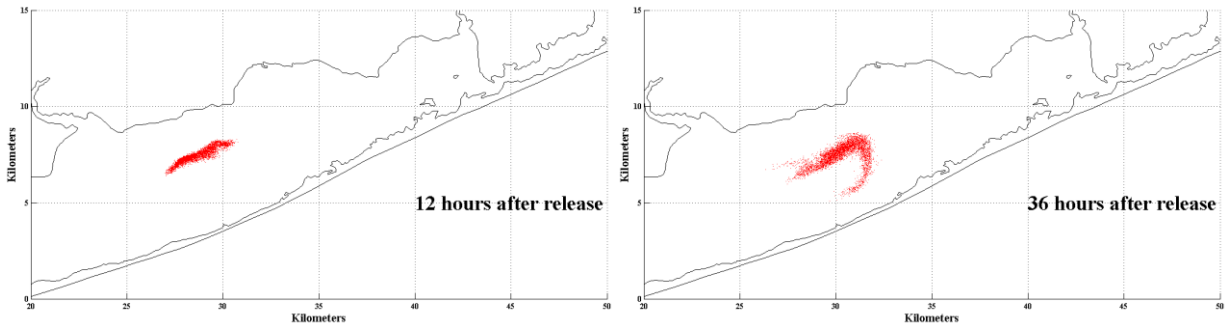

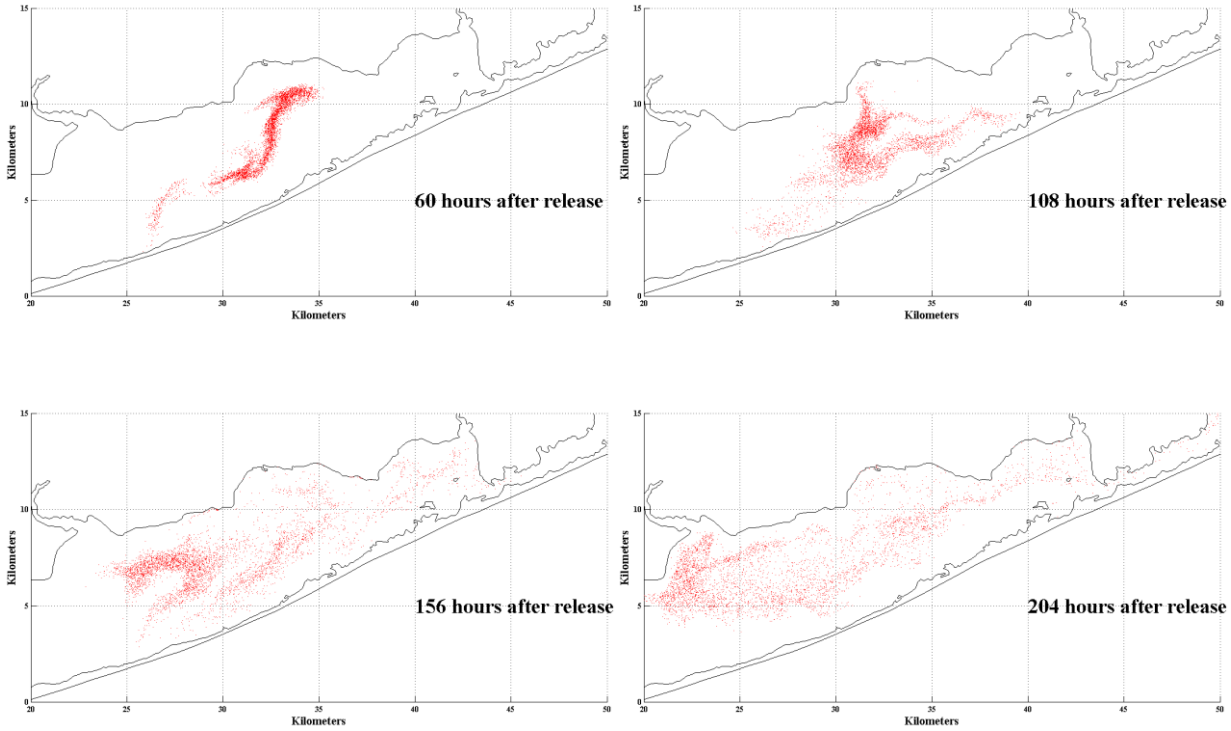


Figure 4.2 Spreading of particle patch #1

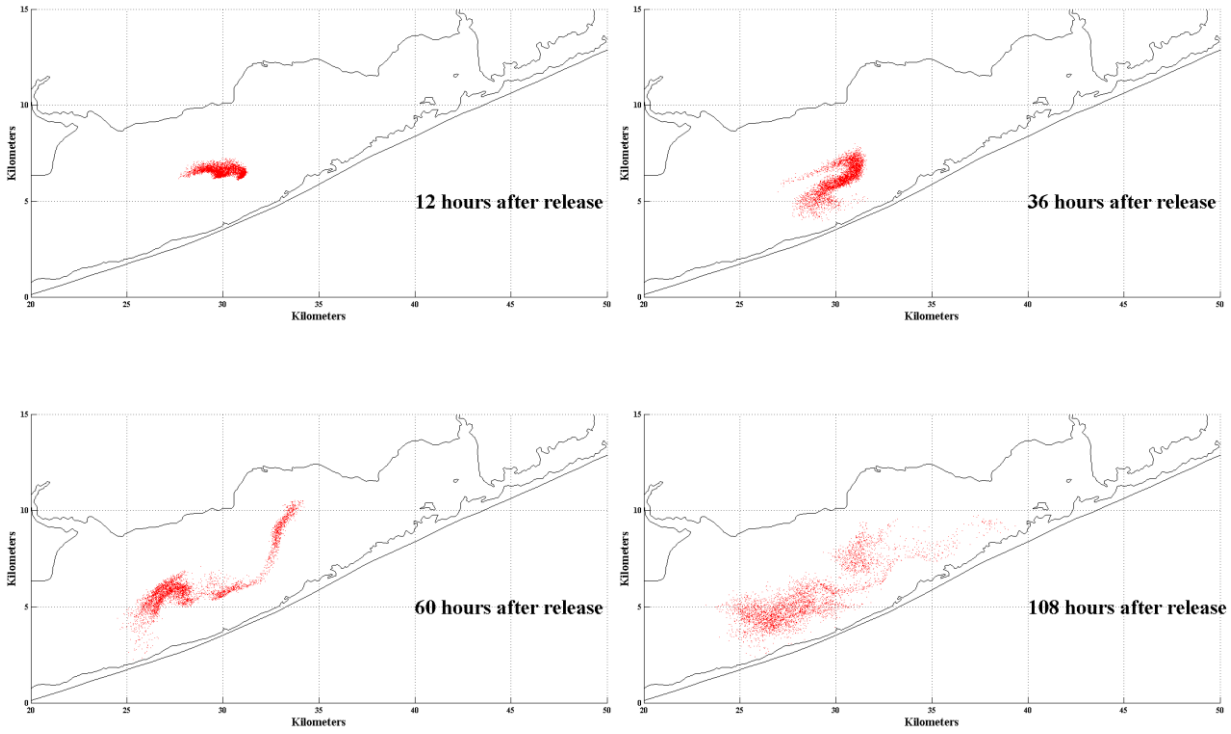

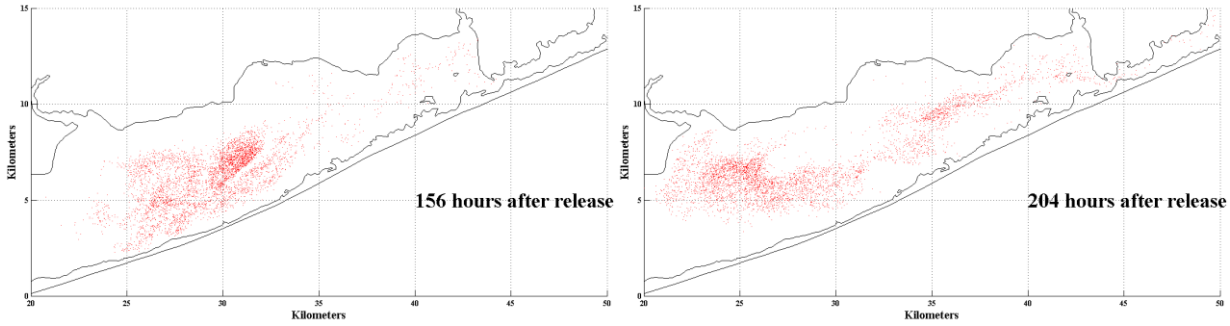


Figure 4.3 Spreading of particle patch #2

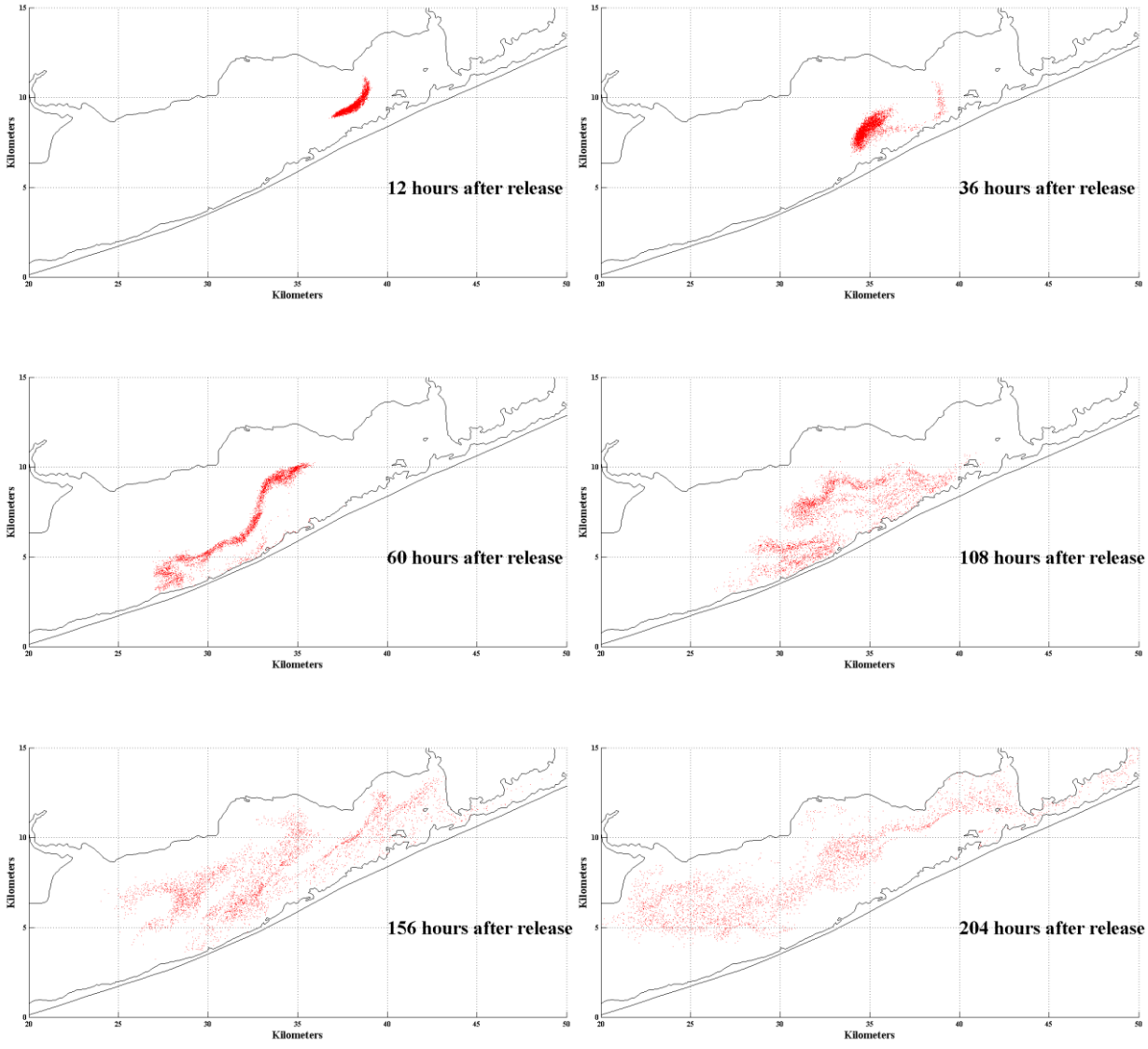


Figure 4.4 Spreading of particle patch #3

Release location of the fourth patch on the sloping bottom near Bellport Bay was only 0.5 km south of the third one, but its spreading pattern was substantially different from the previous three patches (Figure 4.5): this one was transported southward to Fire Island after an initial growth in longitudinal direction, and then spread along Fire Island before it was stretched into the belt-like shape across laterally over the lagoon 156 hours after the release, which was 96 hours later than previous patches, although after which its growth was similar (204 hours after release).

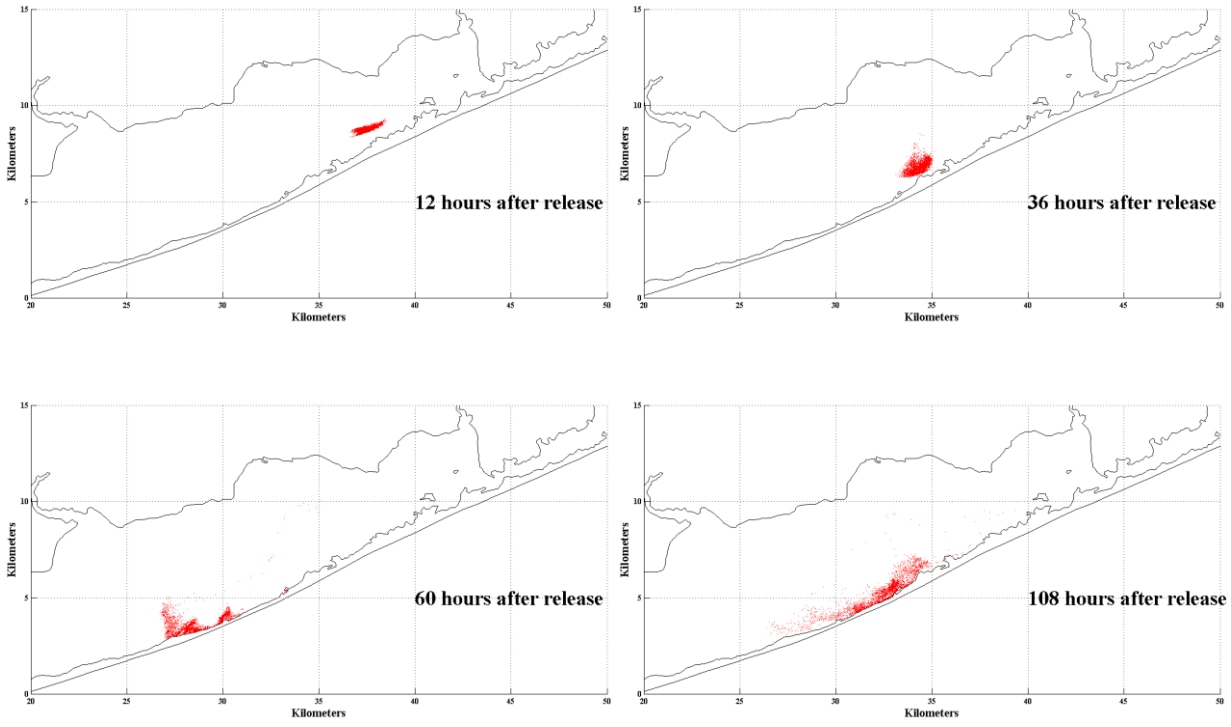

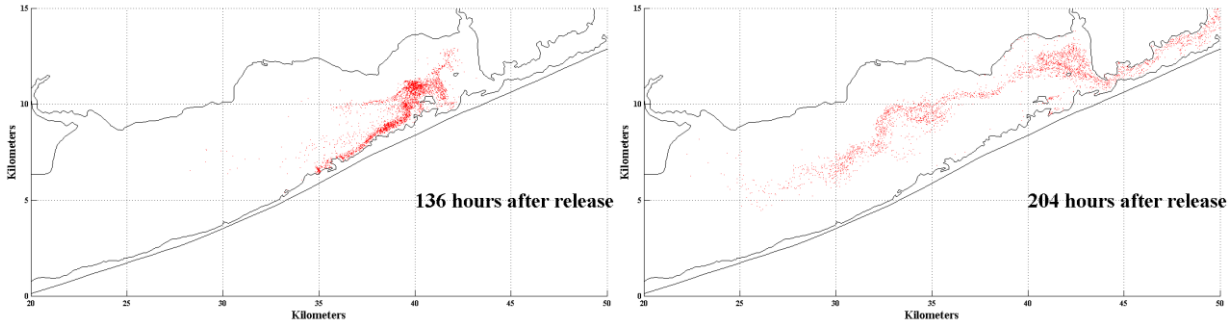


Figure 4.5 Spreading of particle patch #4

Based on the four particle patch releases, two typical spreading patterns were outlined in central GSB. The first three patches were released relatively close to the middle channel of the lagoon where they spread longitudinally during the initial 12 hours; the elongated patches then underwent longitudinally sheared lateral currents and were stretched into a belt-like shape extending over the lagoon in lateral direction; based on the further elongated patch, the horizontal mixing became more significant and areas covered by the particle patches increased steadily afterwards. The fourth patch was also released near the middle channel, but it was closer to the southern shoal than the previous ones, so during early period of the simulation this patch was trapped along the Fire Island and spreads mainly in longitudinal direction until the eastern end of the patch reached into Bellport Bay and transported northward; after this lateral expansion the patch started to receive the influence of currents near the middle channel and to spread in a similar pattern to the other three ones.

## 4.2 Quantification of particle patches dilution and spreading

### 4.2.1 Overall dilution of particle patches

The dilution process of each particle patch was examined by calculating the patch's 'normalized mean concentration' through the simulation. The particle 'concentration' in each FVCOM model element is defined as number of particles divided by this element's volume:

$$C(i,t) = \frac{N(i,t)}{V(i,t)} \quad (4.1)$$

$$V(i,t) = A(i) \cdot [H(i) + \zeta(i,t)] \quad (4.2)$$

where N($i$,$t$) is the number of particles hosted by element $i$ at time $t$, A($i$) and H($i$) are surface area and mean water depth of element $i$, and $\zeta(i,t)$ is the water elevation relative to mean water level at time $t$. To calculate the 'mean' particle concentration $C_{mean}$ at each time step, elements with particle concentration higher than 5% of the observed maximum for this time step were included and their values were averaged. For the purpose of a consistent measure of mean concentration among all particle patches, each patch's mean concentration through the simulation was normalized by its initial concentration before it was diluted:

$$C_{norm}(t) = \frac{C_{mean}(t)}{C_0} \quad (4.3)$$

Dilution processes of the four particle patches are shown in Figure 4.6. During the initial 20 hours after release, the dilution rates of all four patches were all high but also vary among patches. The first and second patches were similar whose concentration dropped below 10% within the initial period and kept at much slower dilution rates until the concentrations became almost constant (10% - 15% of initial mean concentration); their releasing locations were around section 1 in the central lagoon with bigger water depth and cross-section area, although patch 1 was in middle deep channel while patch 2 was above sloping bottom, they are both driven into the deep channel within hours and started to spread in both longitudinal and lateral directions; due to the lagoon bathymetry their dispersion in lateral direction was restricted so that the concentration decreases in a slower rate than the classical $t^{-1}$ function for 2-D spreading. The third patch had much lower initial dilution rate compared with patch 1 and 2 due to its shallower release location with smaller lateral dimension and subsequently even more restricted spreading, and its concentration reduced to approximately 22% 20 hours after the release, but it kept being diluted at a substantial rate after the initial period when it is transported to more central region and the concentration felt to 6% at hour 40 and 2.5% at hour 60 and kept relatively constant afterwards. Patch 4 had the weakest initial dilution among all patches and at 20 hours after the release its concentration was still 40% of the initial one and stayed around 20% from hour 50 to 120 before it decreased to

6%; this could be explained by the fact that it was trapped along Fire Island and did not have noticeable lateral expansion until about 136 hours after release.

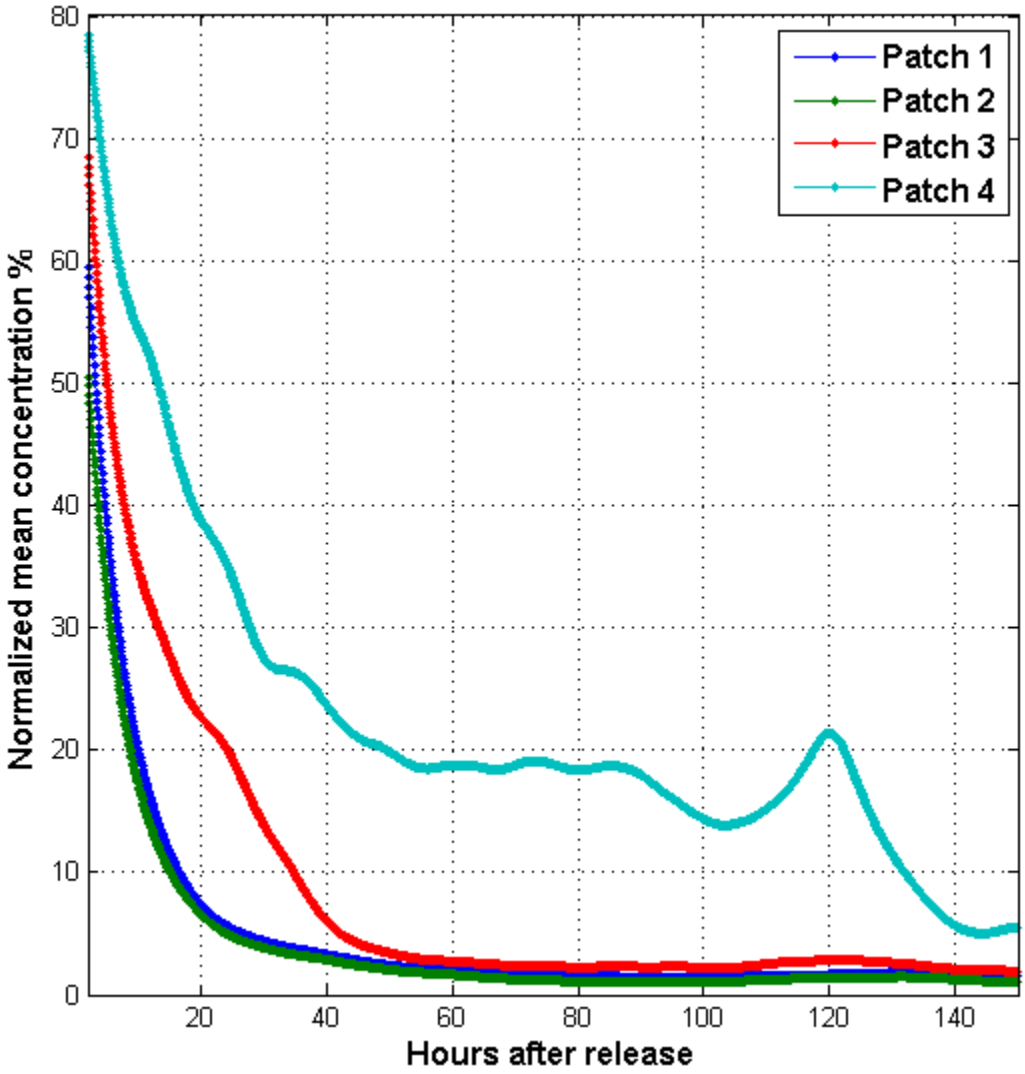


Figure 4.6 mean concentration (%) of all 4 patches as a function of time after release (start at 2 hours after release)

### 4.2.2 Lateral spreading

The lateral spreading could be represented by the second moments of the particle patches in lateral direction at each time step *t*:

$$y'^2 = \frac{\sum_i y(i)^2 \cdot C(i) \cdot V(i)}{\sum_i C(i) \cdot V(i)} - \bar{y}^2 \quad (4.4)$$

where *i* is the index of FVCOM model elements with normalized concentration larger than 5% of the maximal one at the same time step, *y* is the lateral coordinate of the element center, V is the element volume, *C* is the normalized concentration, and $\bar{y}$ is the first moment of the patch in lateral direction defined as:

$$\bar{y} = \frac{\sum_i y(i) \cdot C(i) \cdot V(i)}{\sum_i C(i) \cdot V(i)} \quad (4.5)$$

Given the second moment in lateral direction, the effective lateral dispersion rate can be determined by its time rate of change (Fischer 1979):

$$K_y = \frac{1}{2} \cdot \frac{dy'^2}{dt} \quad (4.6)$$

Time series of the second moments in lateral direction of all the four particle patches are shown in Figure 4.7. Patch 1 and 3 had rapid growth in lateral direction during the first 80 hours after the release, but this was not due to lateral dispersion but the influence of longitudinal sheared lateral currents on the elongated patches (Figure 4.2 and 4.4), and as an evident, their lateral 2nd moment decreased during the following 60 hours due to the further elongation in longitudinal direction (Figure 4.8) and the variation of the patches' orientation. After this period of

‘contraction’, the 2nd moment in lateral direction of patch 3 kept oscillating around a constant mean value, which meant the patch had dispersed substantially in the lateral direction and the local bathymetry started to restrict its extension, and the oscillation was caused by the variation of the patch’s orientation due to the lateral sheared longitudinal currents; the one of patch 1 also had similar oscillation but its value had another rapid increasing starting at 180 hours after the release, this was due to the fact that part of the patch moved into wider region to the west (Figure 4.2). Patch 2 had a steadier lateral expanding throughout the whole simulation period, which reflected its relatively constant orientation and less stretching by sheared currents in lateral direction (Figure 4.3). The period during which patch 4 was trapped along the Fire Island is reflected by the 2nd moment: it kept at a low value until 120 hours after the release and started to increase after that due to lateral dispersion; it oscillated around a relatively low mean value because part of the patch went through the Smith Point channel to the east and the bathymetry constrained its growth in lateral direction.

Based on the discussion above, the mean lateral dispersion rates were calculated by equation (4.6) and trends of the 2nd moment during the whole simulation for patch 1, 2, and 3 and from 120 after the release towards the end of simulation for patch 4 (Figure 4.7).

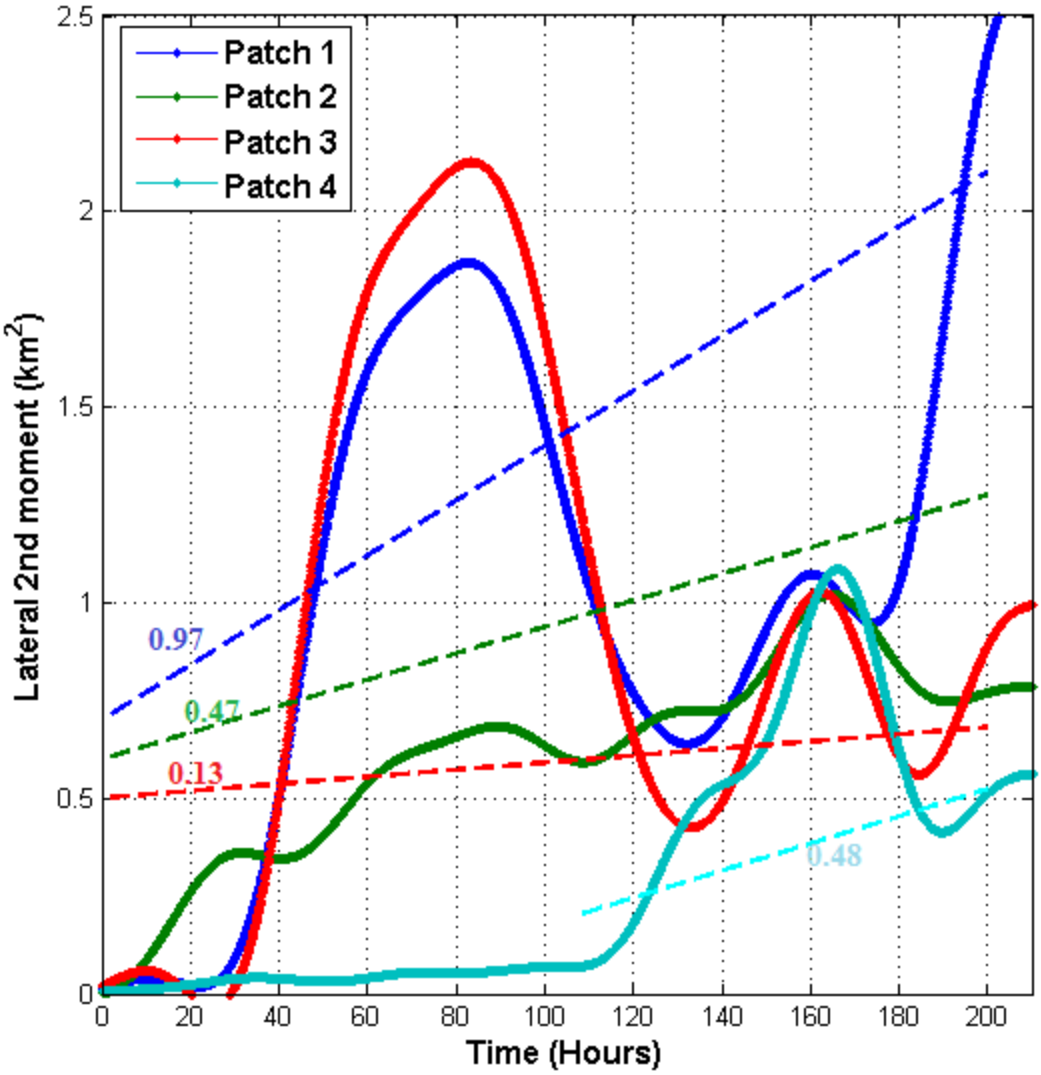


Figure 4.7 moment in lateral direction of the patches

### 4.2.3 Longitudinal spreading

Longitudinal spreading and dispersion rate were determined by the method similar to the lateral ones:

$$\bar{x} = \frac{\sum_i x(i) \cdot C(i) \cdot V(i)}{\sum_i C(i) \cdot V(i)} \quad (4.7)$$

$$K_x = \frac{1}{2} \cdot \frac{dx'^2}{dt} \quad (4.8)$$

The 2nd moments in longitudinal direction of the four patches are shown in Figure 4.8. One common feature of the spreading of the patches was that periods of expansion were followed by periods of contraction, and this pattern was due to the fact that the lateral dispersion was not quick enough to mix up the distorted patch under the influence of lateral sheared longitudinal currents, so the distortion was reduced when the direction of lateral shear reversed (Figure 4.2-4.5). Based on the trends of 2nd moment of patch 1 and 2, these two patches both had two longitudinal spreading periods with different paces. During the first 100 hours after release, they spread at relatively low rates (7.3 $m^2/s$ for patch 1 and 15.9 $m^2/s$ for patch 2) because the lateral coverage of both patches are limited; after hour 100, the lateral extension of the patches covered the area with substantial lateral-sheared longitudinal currents (Figure 4.2, 4.3), thus the dispersion rates increased significantly to 61.6 $m^2/s$ (patch 1) and 37.3 $m^2/s$ (patch 2) attributing mainly to the lateral shear dispersion. Compared with patch 1 and 2, patch 3 had steadier longitudinal spreading rate after the short initial period (hour 0 - 30), this is due to narrower cross-section near its releasing position and the lateral shear of currents occurred in a smaller lateral distance (Figure 4.4) so that the patch experienced the lateral shear dispersion even its size was small. Patch 4 was trapped within a

narrow area during the first 120 hours of the simulation so very little lateral shear dispersion occurred and the longitudinal spreading rate was very low (2.0 $m^2/s$); after hour 120 part of this patch was transported to the middle area of Bellport Bay and the spreading rate increased under the influence of lateral shear dispersion.

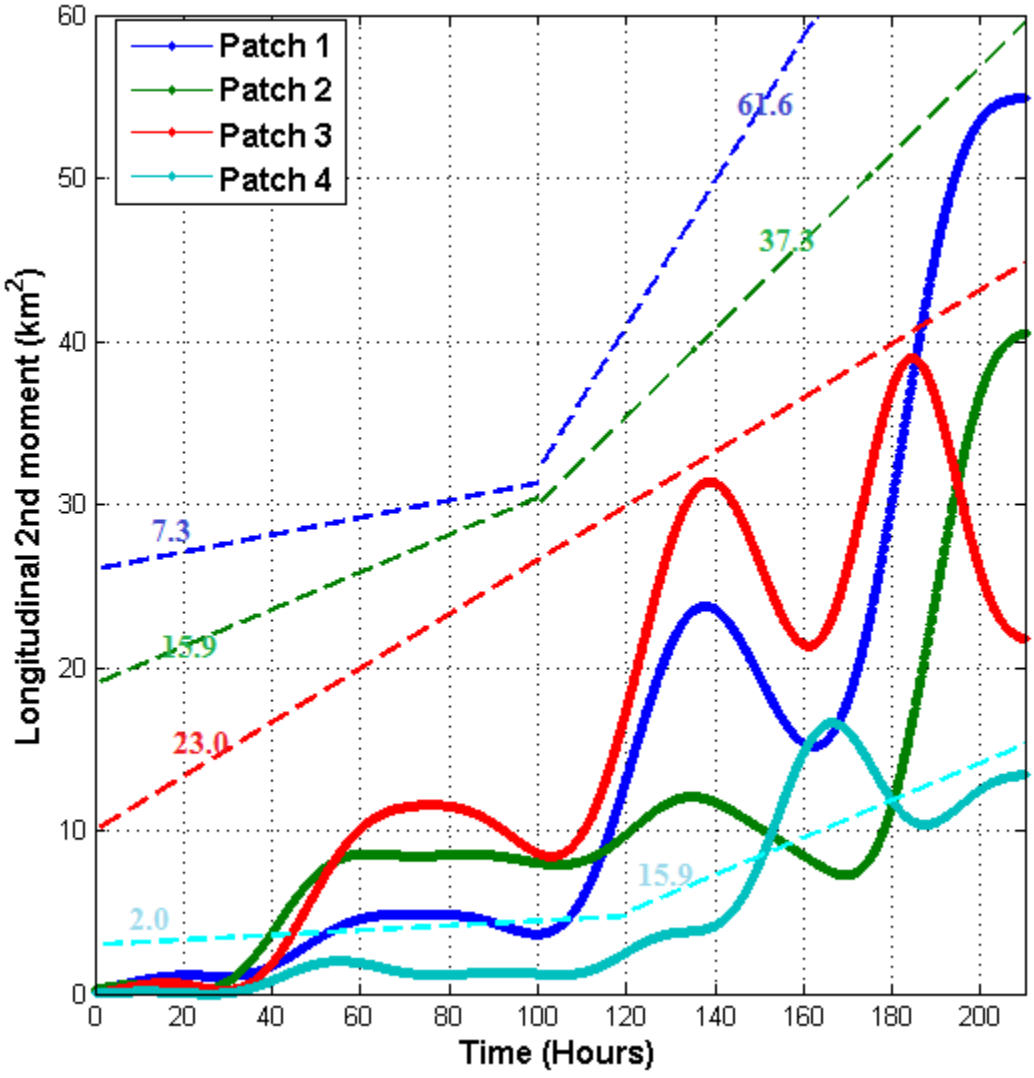


Figure 4.8 2nd moment in longitudinal direction of the patches

## 4.3 Analysis of the longitudinal dispersion rates

### 4.3.1 Vertical shear dispersion

Bowden (1965) demonstrated that the horizontal dispersion $K_x$ due to the combined effect of vertical shear and vertical mixing could be calculated by:

$$K_x = -\frac{1}{H}\int_0^H u'(z)\int_0^z \frac{1}{K_z(z)}\int_0^z u'(z)dzdzdz \quad (4.9)$$

at given location where $u'(z) = u(z) - \frac{1}{H}\int_0^H u(z)dz$ is the deviation from the depth-average velocity, $K_z(z)$ is the vertical eddy viscosity, and H is the water depth; both u' and $K_z$ are depth-dependent.

Rates of wind-driven vertical shear dispersion in longitudinal direction at different locations (Figure 4.9) were calculated by substituting vertical profiles of longitudinal velocity and vertical eddy viscosity into equation (4.9), and the results are shown in Figure (4.10). Generally speaking the vertical shear dispersion at all locations were weak (less than 1 $m^2/s$) so it only explained the very initial period (hour 0 - 30) of the longitudinal spreading and after that all particle patches had much higher spreading rate. Locations in shallower area (2 and 4) had much stronger vertical shear dispersion that those in deeper middle channel (1 and 3) due to stronger vertical shear in longitudinal velocities (Chapter 3). Despite the

different magnitudes, vertical shear dispersion had similar pattern for all the 4 locations, and this pattern was correlated with magnitude of wind speed (Chapter 3).

The vertical shear dispersion produced by tidal currents is ignored, because despite the comparable magnitude to wind-driven currents, the tidal currents are almost uniform in the vertical direction through the water column (Chapter 1).

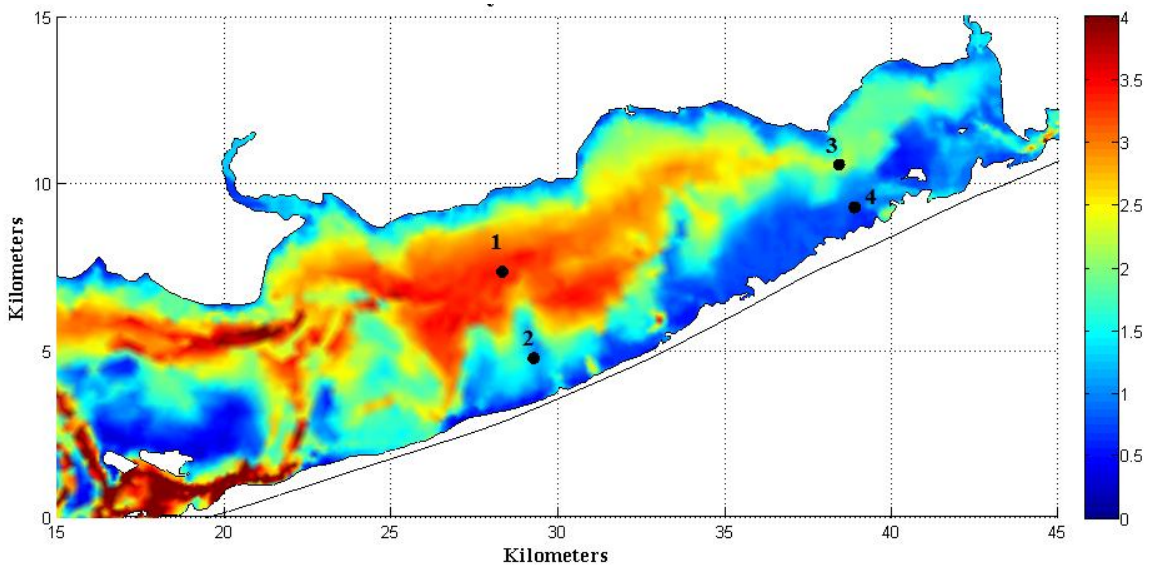


Figure 4.9 Locations of stations

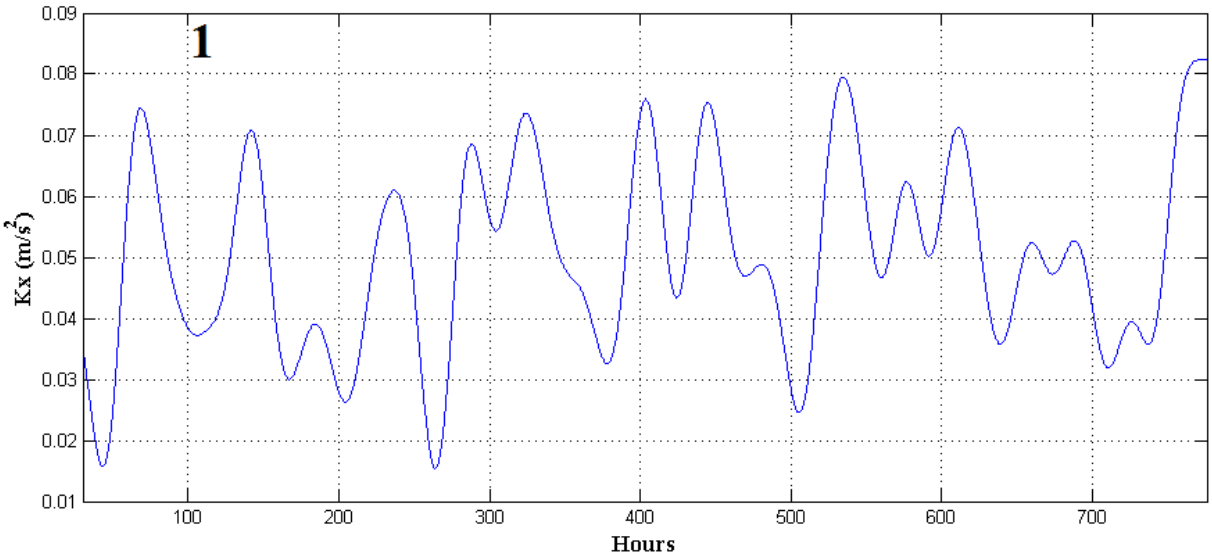
1
Kx (m/s2)
Hours
0.09
0.08
0.07
0.06
0.05
0.04
0.03
0.02
0.01
100
200
300
400
500
600
700

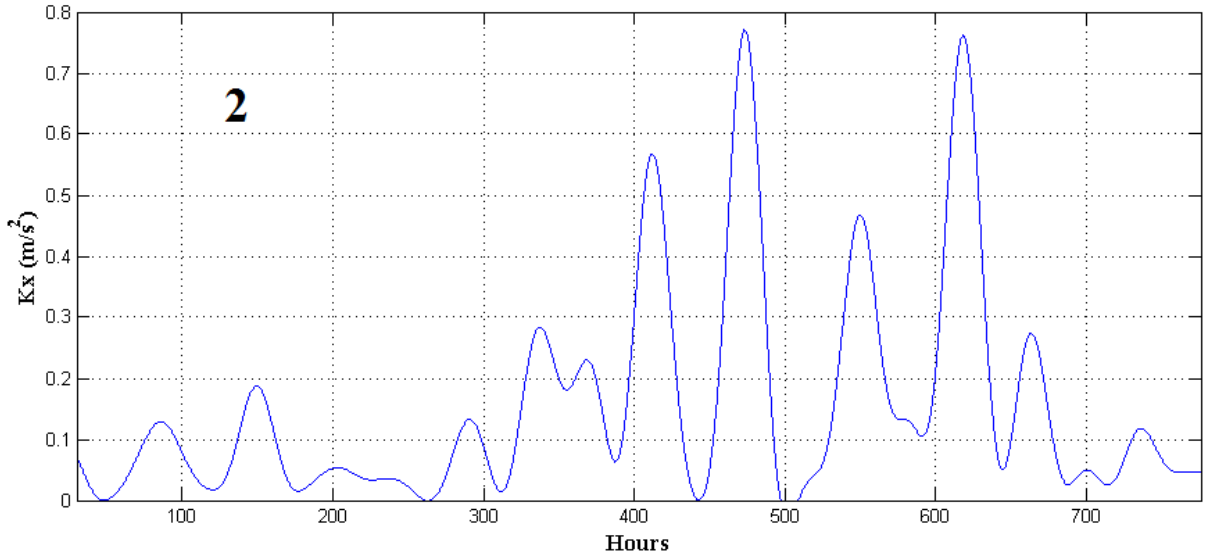
2
Kx (m/s2)
Hours
0.8
0.7
0.6
0.5
0.4
0.3
0.2
0.1
0
100
200
300
400
500
600
700

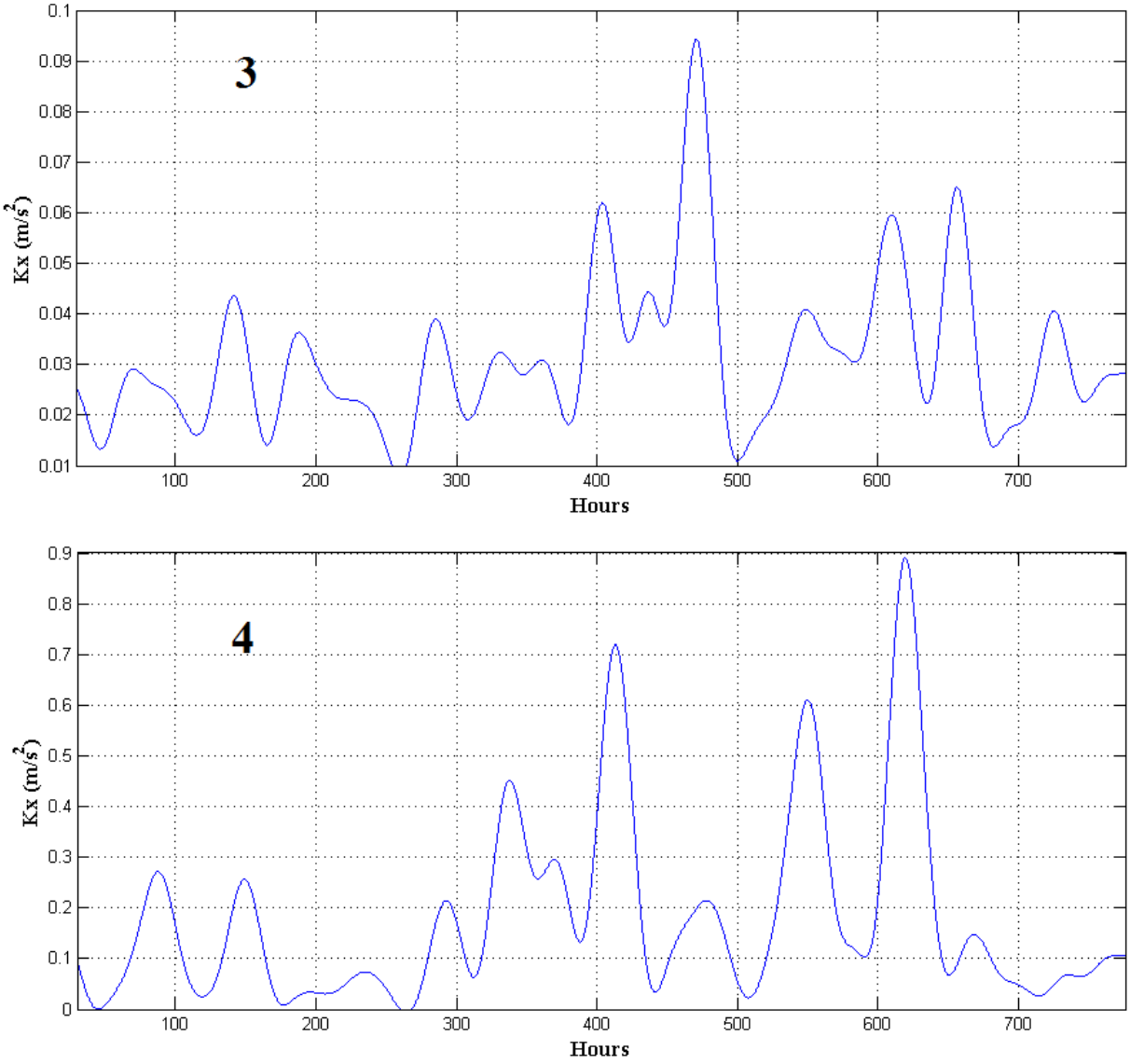


Figure 4.10 Time series of vertical shear dispersion in longitudinal direction at locations 1 – 4

### 4.3.2 Lateral shear dispersion in longitudinal direction

Calculation of lateral shear dispersion induced by the interaction of effective lateral mixing and lateral shear of longitudinal current is analogous to the one of vertical shear dispersion:

$$K_x = -\frac{1}{D}\int_0^D u'(y)\int_0^y \frac{1}{K_y(y)}\int_0^y u'(y)dydydy \quad (4.10)$$

where u' is the deviation calculated from the depth-mean velocity on given sections, D is the lateral width of the particle patch, and $K_y$ is the lateral dispersion rate. Based on the observation of particle simulations, time-averaged extension of particle patches were typically less than 1/3 of cross-section widths, thus 1/3 of the width of given sections was used as D.

The wind-driven lateral shear dispersion in longitudinal direction was calculated first using low-pass filtered velocities. On section 1 (Figure 3.1) the lateral dispersion rate estimated by the spreading of particle patch 1 (0.97 $m^2/s$) was used as the value of $K_y$, and the time-average value of calculated $K_x$ through the simulation was approximately 360.0 $m^2/s$. The similar calculation was applied to section 2 (Figure 3.1) with $K_y$=0.48 $m^2/s$ estimated from the spreading of particle patch 4, and the time-average was approximately 126.5 $m^2/s$. Rates of lateral shear dispersion in the longitudinal direction on both sections estimated by the classic Bowden's formula were much larger than the observed value from particle patch simulations (37.3 – 61.6 $m^2/s$ near section 1 and 15.9 – 23.0 $m^2/s$ near section 2), but it should be noticed that the Bowden's formula is only valid for steady sheared currents and for oscillatory currents the value is halved if the mixing time $T_M$ is much smaller than the oscillatory time scale T (Bowden 1965). The lateral mixing time scale in GSB was calculated as:

$$T_M = \frac{D^2}{10K_y} \quad (4.11)$$

where L is the lateral length scale as used for the lateral shear dispersion and $K_y$ is still the effective lateral dispersion rate estimated from particle patch spreading. Resulted $T_M$ for section 1 and 2 were 5.0 and 2.4 days which were comparable to the 2-7 days synoptic period T. Zimmerman (1986) studied the oscillatory shear dispersion and suggested the ratio R of oscillatory shear dispersion to the steady one with the same magnitude of shear was a function of $\frac{T}{T_M}$:

$$R = \frac{30}{\pi^2}\tau_v\{1-\tau_v[\coth(\frac{2}{\tau_v}) - \operatorname{csc} h(\frac{2}{\tau_v})]\} \quad (4.12)$$

$$\tau_v = \frac{K_y \cdot T}{D^2} = \frac{1}{10}\frac{T}{T_M} \quad (4.13)$$

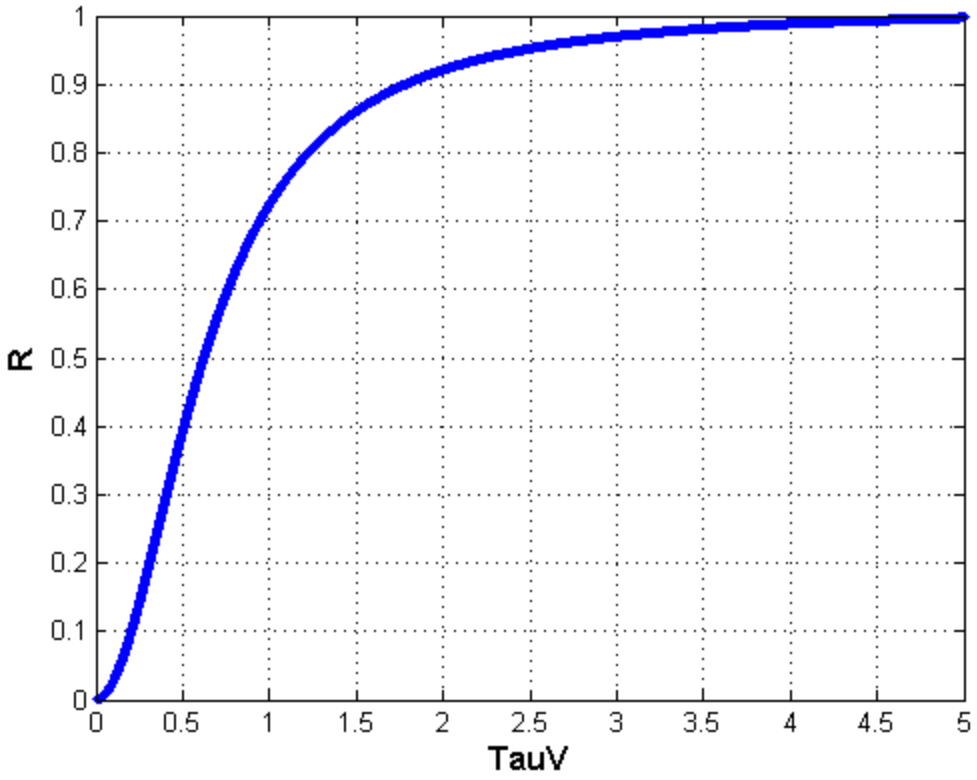


Figure 4.11 of oscillatory to steady lateral shear dispersion with the same shear magnitude

Taken 6 days as the value of T, the ratio R (Figure 4.11) for section 1 and 2 were approximately 0.04 and 0.14, thus the adjusted lateral dispersion were 13.9 and 18.0 $m^2/s$, which had the same order but smaller than the observed value.

Tidal currents are also oscillatory, so their contributions to lateral shear dispersion in longitudinal direction are calculated with the similar methods by using high-pass filtered (34 hours cutoff period) velocities. With $K_y$ = 0.97 and 0.48 $m^2/s$, the time-average value of calculated $K_x$ produced by tidal currents are 150.0 $m^2/s$ and 76.7 $m^2/s$ on section 1 and 2 separately according to Bowden's formula. The dominant tidal constituents in GSB is $M_2$ so the oscillatory time scale of tidal

currents (T) is set to be 12.42 hours in equation (4.12) which gives the values of ratio R $3\times10^{-4}$ and $1.3\times10^{-3}$ on section 1 and 2. The adjusted tidal lateral shear dispersion then are $4.5\times10^{-2}\ m^2/s$ and 0.1 $m^2/s$ which are much smaller and negligible compared to the wind-driven lateral shear dispersion.

Another contributor to the lateral shear dispersion in longitudinal direction was the steady shear currents. Substituting the mean flow (Chapter 3) on both sections into equation (4.10) gave 41.6 and 19.1 $m^2/s$ which were larger than the ones induced by the wind-driven shearing currents. For the oscillatory currents, when the mixing time was comparable or even longer than the oscillatory period of wind forcing, the lateral mixing did not keep pace with the distortion of particle patches, and the patches' shape restored as the wind direction reversed, which reduced the dispersion rate. The reversion did not occurred with the steady flow, so the mean flow induced stronger lateral shear dispersion although its magnitude was smaller than the wind-driven flow.

The combination of steady and oscillatory lateral shear dispersion (55.5 $m^2/s$ on section 1 and 37.1 $m^2/s$ on section 2) were close to the observed dispersion rate based on the spreading of particle patches, and the difference could be due to the fact that other locations in central GSB had slightly different

dispersion rate than the two sections studied here, and that the assumption of a uniform $K_y$ through a cross-section might not reflect the real lateral dispersion rate.

## 4.4 Analysis of the lateral dispersion rates

### 4.4.1 Vertical shear dispersion in lateral direction

The vertical shear dispersion in lateral direction $K_y$ was calculated based on vertical mixing rate $K_z$ and vertical velocity profile at locations 1- 4 (Figure 4.9) as:

$$K_y = -\frac{1}{H}\int_0^H v'(z)\int_0^z \frac{1}{K_z(z)}\int_0^z v'(z)dzdzdz \quad (4.14)$$

Results of vertical shear dispersion in lateral direction are shown in Figure 4.12, like the ones in longitudinal direction, they oscillated throughout the simulation and had substantial correlation with the wind velocity (Figure 3.11). The time-averaged dispersion rates ranged from approximate 0.03 to 0.1 $m^2/s$ and the values were much smaller than the observed rates from the spreading of particle patches in nearby areas. Thus like the longitudinal dispersion, the lateral dispersion could not be explained by the vertical shear dispersion only and the horizontal shear needed to be examined.

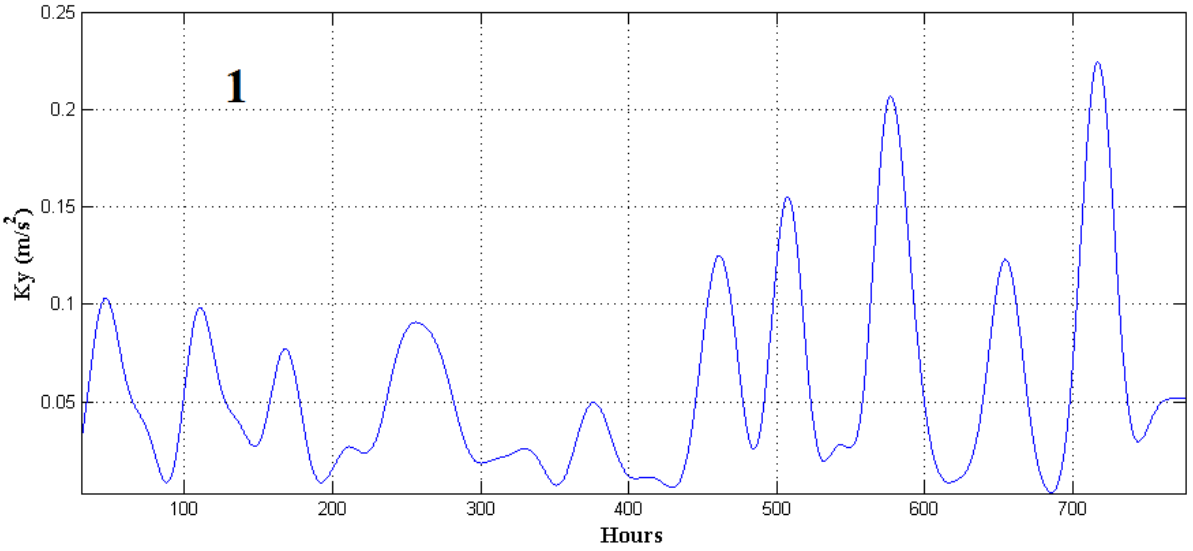
1
0.25
0.2
0.15
0.1
0.05
Ky (m/s²)
100
200
300
400
500
600
700
Hours

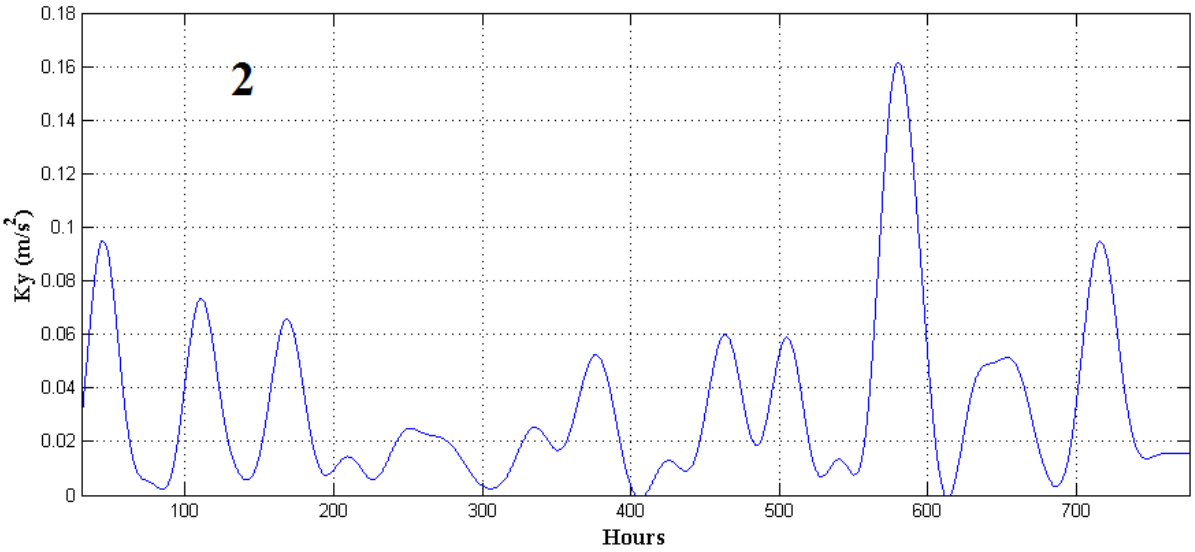
2
0.18
0.16
0.14
0.12
0.1
0.08
0.06
0.04
0.02
0
Ky (m/s²)
100
200
300
400
500
600
700
Hours

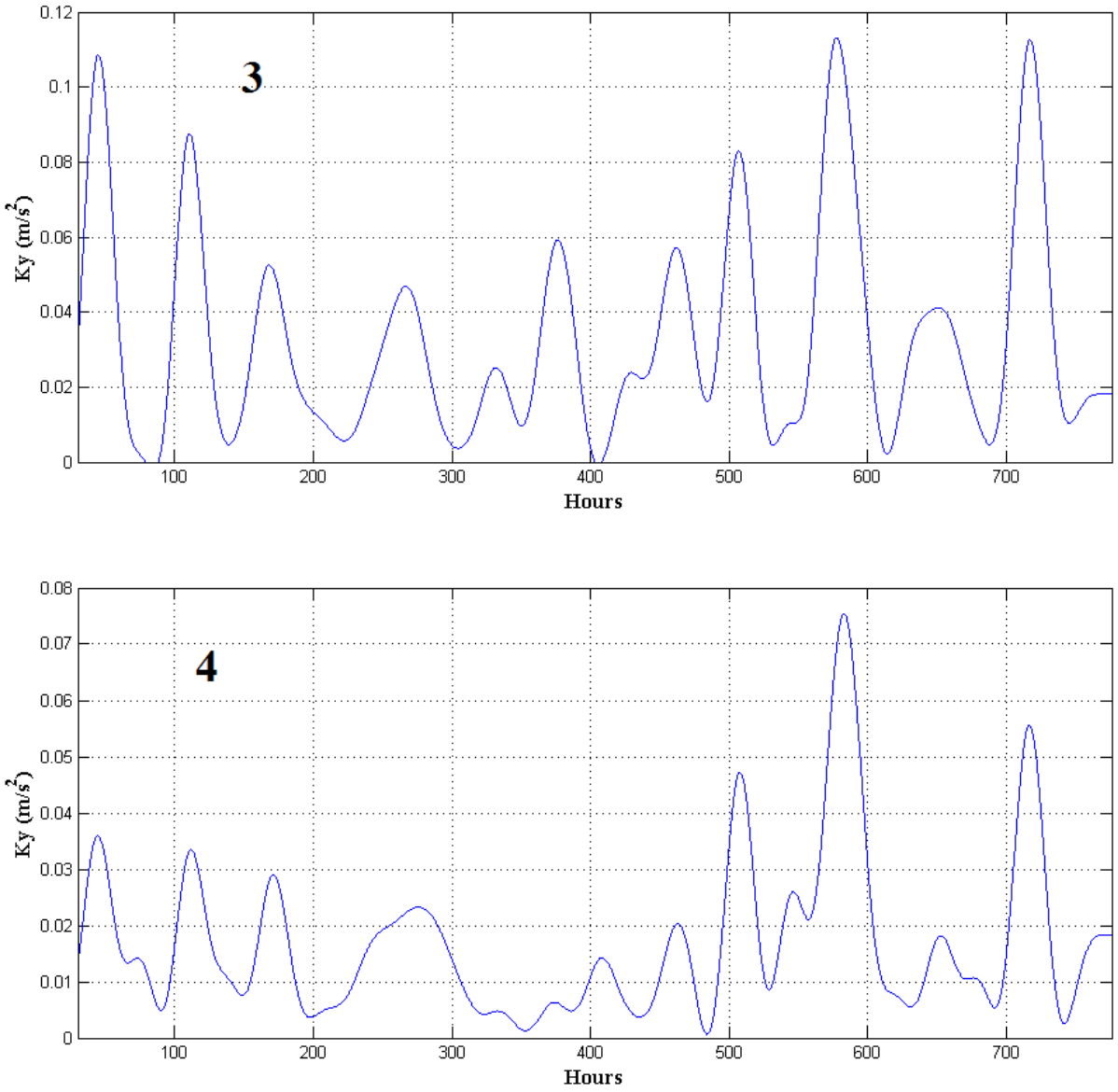


Figure 4.12 series of vertical shear dispersion in lateral direction at locations 1 – 4

### 4.4.2 Longitudinal shear dispersion in lateral direction

The lateral currents sheared in longitudinal direction and interacted with the longitudinal mixing to produce longitudinal shear dispersion in lateral direction, and its rate was calculated by:

$$K_y = -\frac{1}{L}\int_0^L v'(x)\int_0^x \frac{1}{K_z(x)}\int_0^x v'(x)dxdxdx \quad (4.15)$$

where L is the length of a section in longitudinal direction on which the shear dispersion was calculated. Unlike H and D in the calculations of vertical and lateral shear dispersion, the definition of L was complicated by the highly varying locations of particle patches. To make an approximate estimation, a section as shown in Figure 4.13 was selected to represent a typical patch location and longitudinal coverage.

For the oscillatory longitudinal shear dispersion, the model output (Chapter 3) depth-averaged lateral current velocity on the section was used to calculate v' in equation (4.15), and 60 $m^2/s$ was used as the effective longitudinal mixing rate. The time averaged result was 2.2 $m^2/s$. As in the oscillatory lateral shear dispersion, the ratio R as a function of synoptic period T and longitudinal mixing time $T_M$ was calculated using equations (4.12) and (4.13). The mixing time $T_M$ calculated using the section length L and $K_x$ = 60 $m^2/s$ was 2.2 days which resulted in R = 0.16. Thus the value of adjusted oscillatory longitudinal shear dispersion was 0.36 $m^2/s$.

For the steady longitudinal shear dispersion, the residual depth-averaged current velocity was utilized and the longitudinal mixing rate was kept the same as in the calculation of the oscillatory one. The resulted value of steady shear dispersion was 0.36 $m^2/s$ which was similar to its oscillatory counterpart. The total

dispersion rate induced by the longitudinal shear was 0.72 $m^2/s$ which was close to the value estimated by the spreading of nearby particle patches. Again, due to highly variable location and longitudinal extension of the patches, this only gave a first order estimation of how longitudinal variation of lateral current velocity could enhance the lateral dispersion efficiency.

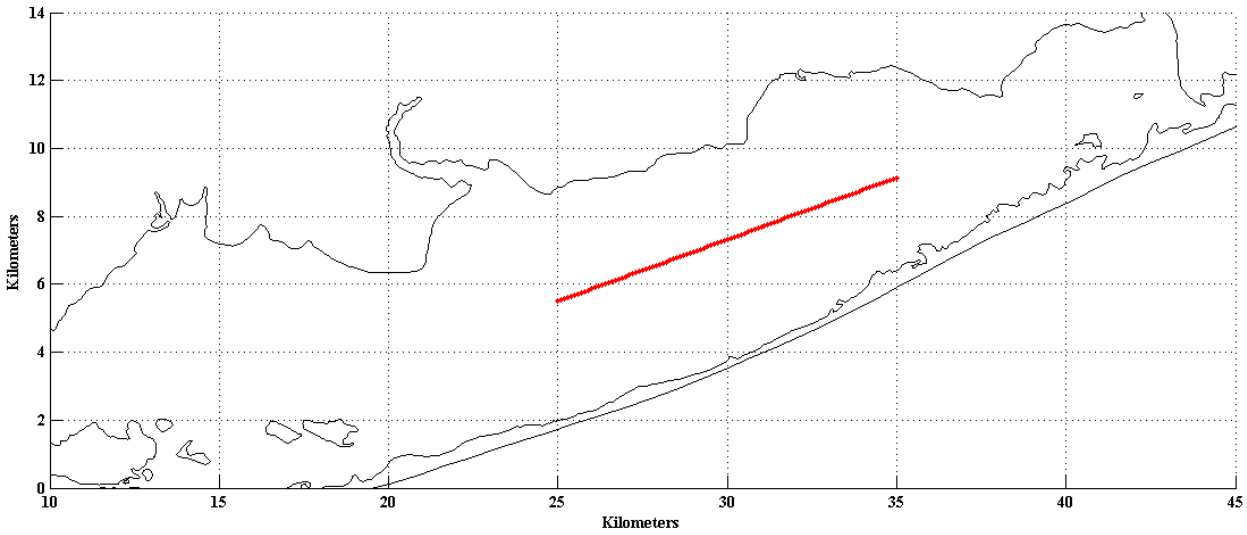


Figure 4.13 Section on which the longitudinal shear dispersion was calculated

## 4.5 Summary

In this chapter, horizontal dispersion rates in both longitudinal and lateral directions within central GSB were estimated based on spreading of particle patches released in multiple locations. The values were 0.13-0.97 $m^2/s$ for the lateral dispersion and 15.9-61.6 $m^2/s$ for the longitudinal dispersion depending on the initial position of the patches. The dispersion rates were analyzed by two mechanisms: vertical and horizontal shear dispersion. Due to the limit in water

column depth, the values of vertical shear dispersion were much smaller than the effective dispersion rates of the patches. Oscillatory currents in central GSB induced much stronger horizontal shear dispersion in both longitudinal and lateral directions, but because of the long horizontal mixing time, their ratio were adjusted by R; and together with the steady sheared currents, the total horizontal shear dispersion rates explained the effective dispersion of particle patches very well. In central GSB, horizontal (lateral or longitudinal) shear dispersion was the major mechanism of the horizontal mixing, and the oscillatory and steady currents were equally important for this process.

# Chapter 5 Residence time and inner-lagoon connectivity

## 5.1 Residence time pattern of central GSB

Lagrangian particles were released uniformly to the surface of central GSB in a spatial resolution of 0.2 km (Figure 5.1) at hour 435 which is at the beginning of a northwestward wind event (Figure 3.3 and 3.11), and were driven by the simulated flow field from FVCOM for 36 days. Residence time distribution was calculated by the method of first passage time (Aikman and Lanerolle, 2005) from the particle tracking information. First passage time for given particle is the time when it crosses the lagoon boundary for the first time after the releasing, and this time is considered as the residence time of the associated particle initial position.

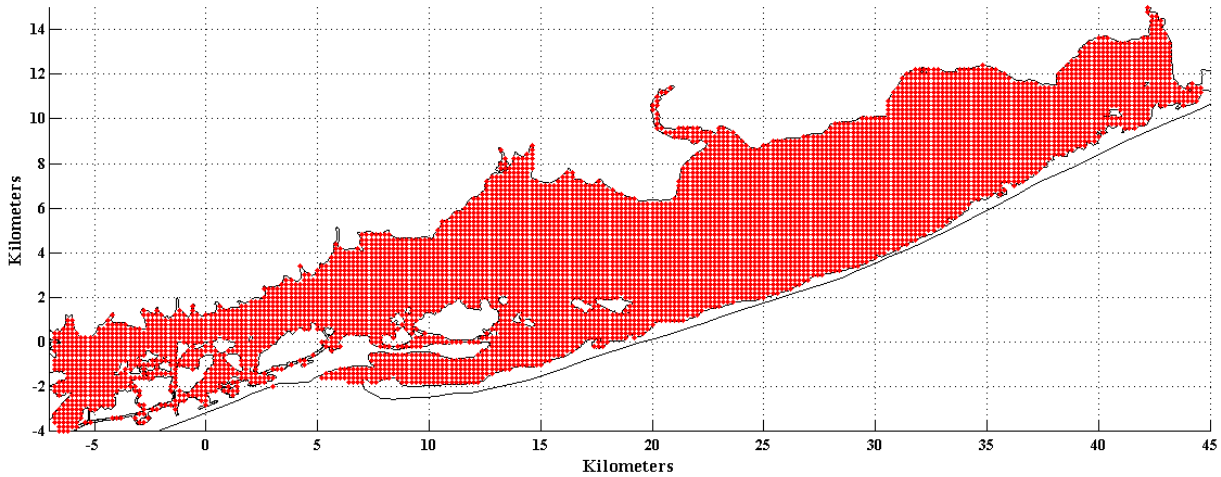


Figure 5.1 Initial positions of Lagrangian particles

Residence time in central GSB calculated by the first time method is shown in Figure 5.2. Generally the residence time in central GSB was long and the value in most part of the lagoon exceeded 600 hours (25 days), especially in the central area

which had residence time over 800 hours. In regions near the inlets (Fire Island Inlet and Smith Point channel), residence time was much shorter (less than 100 hours). Trajectories of particles released in different locations explained the spatial distribution of residence time (Figure 5.3): the particle released closed to Fire Island Inlet was transported quickly to the coastal ocean through the inlet under relatively strong longitudinal currents in this area (Chapter 3); the particle released far from both inlets oscillated within the lagoon under the influence of both winds and tides, the excursion of its trajectory was much smaller compared to the length of the lagoon, so during the simulation it failed to leave central GSB. Due to the limited simulation length, the maximal residence time is 36 days, and those particles never left the lagoon were assigned with this maximal value but their real value could be much larger.

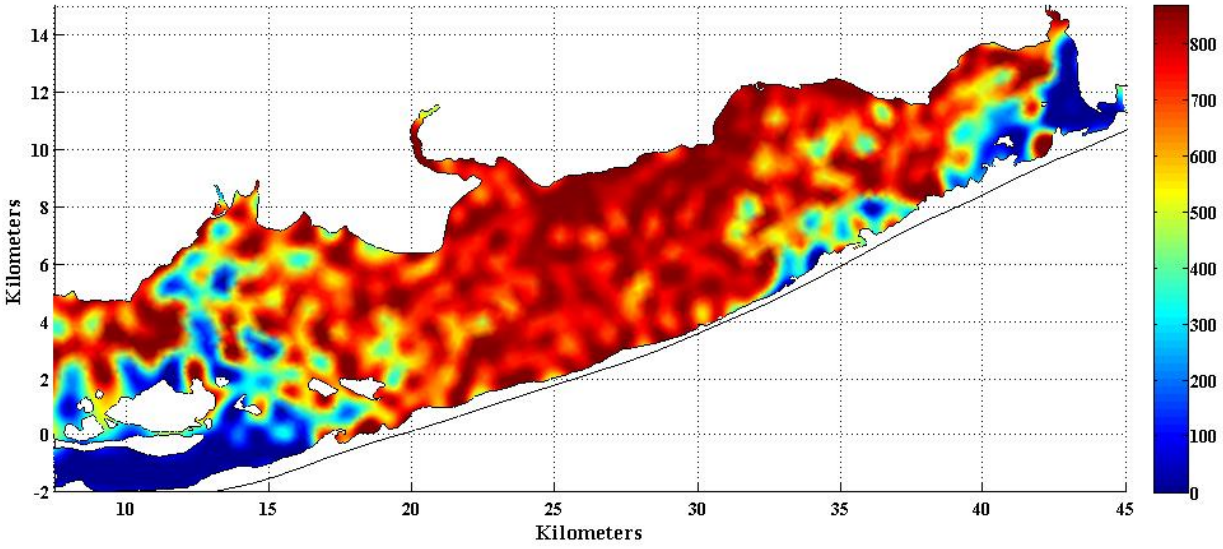


Figure 5.2 Residence time in central GSB (hours)

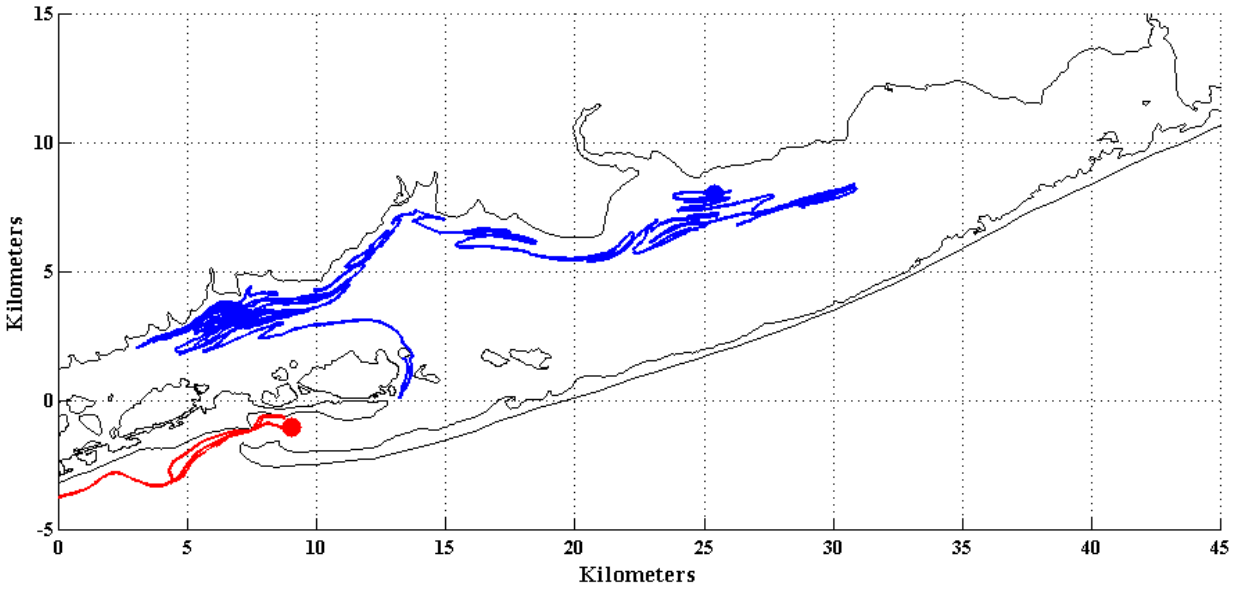


Figure 5.3 Trajectories of Lagrangian particles

The flushing of central GSB was restricted by the limited lagoon-coast exchange, but according to the particle trajectories (Figure 5.3) transport and mixing processes within the lagoon were still robust. Thus to analyze the inner lagoon movement, central GSB was partitioned into 8 compartments according to the topography character and the first passage times of particles within each compartments were calculated regarding to boundary of the compartment instead of the entire lagoon. Partitioning and residence time distribution within each compartment are shown in Figure 5.4. Because of the reduced domain size, particles spent much shorter time to cross boundaries, and the average residence time over the lagoon was 56.7 hours. Due to the onset of westward wind at the beginning of the particle release, the western part of each compartment had the shortest residence time (less than 24 hours), and areas with larger residence time

were typically located in the eastern parts (compartment 2, 3, 4, 7, and 8). Residence time was short over the entire compartment 1 due to its small size. In compartment 5 and 6, residence time was also short on the southeast corners where particles entered other compartments to the south.

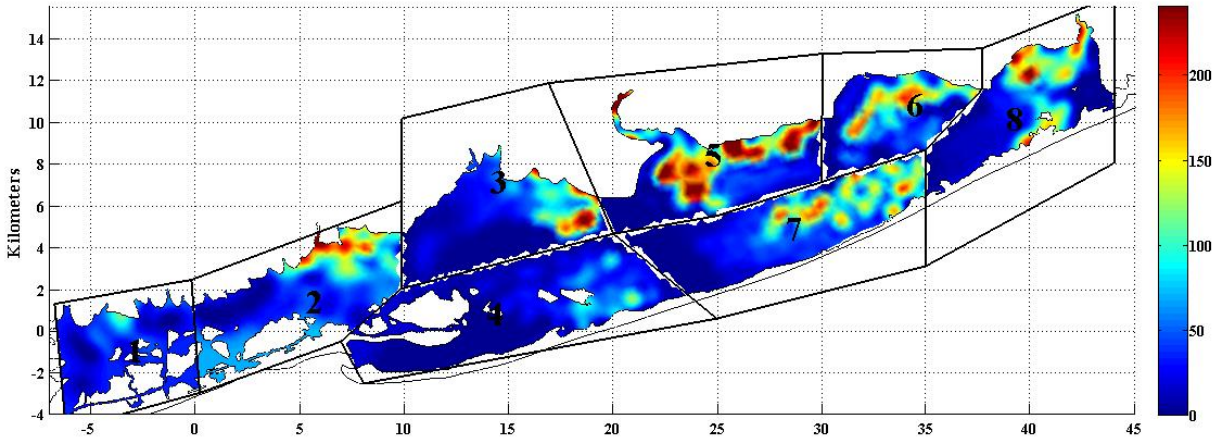


Figure 5.4 Residence time (hours) in compartments of central GSB under tidal and realistic wind forcing

To demonstrate the influence of wind forcing on inner-lagoon transport and mixing processes, Lagrangian particle simulation was applied based on tide-only flow field from FVCOM simulation and the residence time was calculated related to the same compartments (Figure 5.5). Unlike the realistic wind case, in each compartment the residence time increased from eastern and western boundaries to central areas due to the more symmetric longitudinal current generated by tides. The overall residence time was longer when the wind forcing was not included: the average residence time increased from 56.7 hours to 66.0 hours and approximately half of the lagoon had residence time longer than 100 hours.

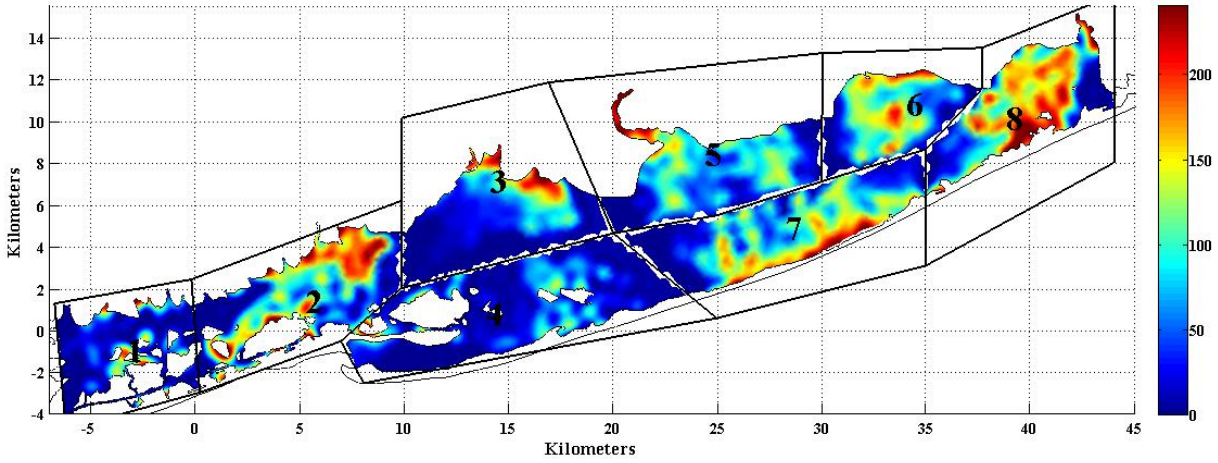


Figure 5.5 time (hours) in compartments of central GSB under tidal forcing only

## 5.2 Connectivity within central GSB

First order Markov Chain was applied to study connectivity among compartments within central GSB. Thompson et. al. (2002) described the details about the first order Markov Chain and applied it to a tide-dominant embayment. This method allows statistically characterizing the connectivity process by specification of a transition matrix alone, and the transition matrix (P) could be determined by considering each of its elements as a conditional probability:

$$P_{ij}(t) = prob\{X(t+1) = j \mid X(t) = i\} \quad (5.1)$$

where X(t) is a random variable indicating the host compartment of a particle at time step t, i and j represent compartments ($i, j \leq 8$ for central GSB). The conditional probabilities were estimated by counting number of particles in each compartment at current and next time step:

$$P_{ij}(t) = \frac{n_{i\to j}(t \to t+1)}{n_i(t)} \quad (5.2)$$

where $n_{i\to j}(t \to t+1)$ is number of particles moving from compartment i to j during the time interval between step t and t+1, and $n_i(t)$ is total number of particle in compartment i at the beginning of step t.

Transition probabilities were calculated first for the tide-only case with semidiurnal time interval, and time series of some elements are shown in Figure 5.6. Mean values of the transition probabilities as functions of time were from 0.01 to 0.03, and the standard deviations were approximately 0.006. For the rest elements in the transition probability matrix the standard deviation were also small compared to the mean values, thus the transition probabilities were relatively constant through the simulation and it could be assumed that the stationarity of Markov Chain was satisfied. The one single transition probability matrix for the stationary first order Markov Chain was calculated by taking the time-averaged value of every element through the simulation, and it is shown in Table 5.1. Elements on the diagonal show probabilities that a particle would stay in the compartment where it was at the beginning of each time step, thus show how 'restrictive' a given compartment could be. The most restrictive one was compartment 8, and the probability was over 94% that a particle started within it would stay. It could be explained by the fact that the circulation in this area

(Bellport Bay) formed a gyre which prevented particles moving very far in longitudinal direction, and its exchange with Moriches Bay to the east was limited by the width of Smith Point Channel. Compartment 2 was also restrictive (probability a particle would stay was over 91%), and it was caused by the marshes which hindered the particle movement so that the excursions of most particles were less than its longitudinal length. The least restrictive compartment is 1, and the chance a particle left this compartment after one time step was over 20% due to its small longitudinal length. The major receiving region of particles from 1 was compartment 2. The second least restrictive one is compartment 4. The strong currents near the Fire Island Inlet brought particles to the north (6.4% to compartment 3) and the east (5.4% to compartment 7); it also had exchange with the coast through the inlet, and 3.6% of its particles left the lagoon every time step.

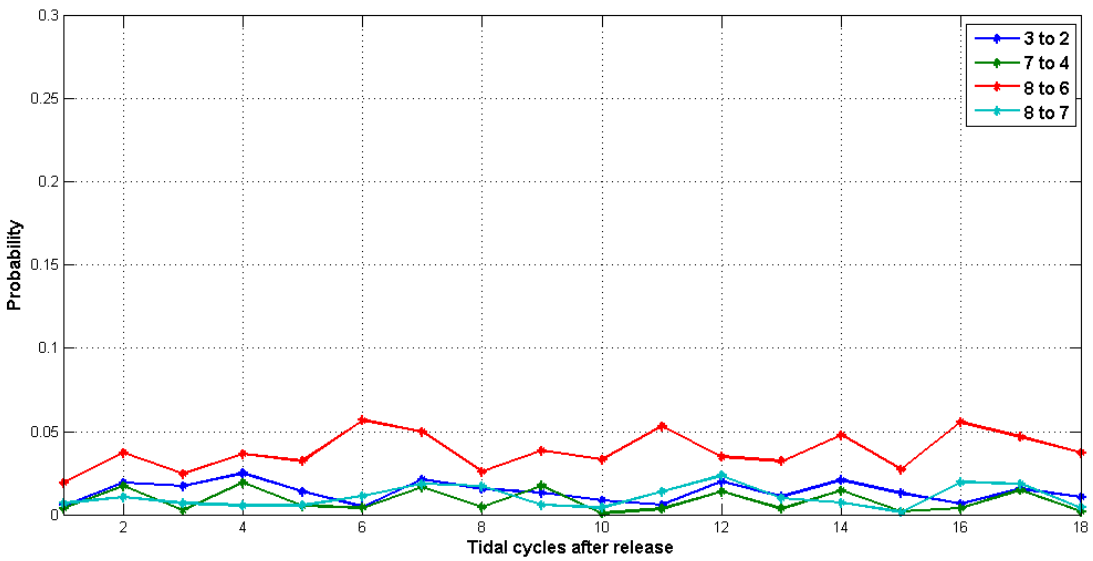


Figure 5.6 Transition probabilities of tide-only Lagrangian particle simulation

| Compartments | 1 | 2 | 3 | 4 | 5 | 6 | 7 | 8 | 9 |
|---|---|---|---|---|---|---|---|---|---|
| 1 | 79.43 | 17.42 | 0.00 | 0.00 | 0.00 | 0.00 | 0.00 | 0.00 | 3.15 |
| 2 | 1.19 | 91.27 | 2.31 | 5.03 | 0.00 | 0.00 | 0.00 | 0.00 | 0.2 |
| 3 | 0.00 | 1.37 | 89.11 | 9.30 | 0.22 | 0.00 | 0.00 | 0.00 | 0.00 |
| 4 | 0.00 | 0.52 | 6.44 | 83.77 | 0.23 | 0.00 | 5.43 | 0.00 | 3.61 |
| 5 | 0.00 | 0.00 | 3.45 | 0.07 | 85.21 | 2.98 | 8.29 | 0.00 | 0.00 |
| 6 | 0.00 | 0.00 | 0.00 | 0.00 | 2.73 | 86.78 | 6.18 | 4.30 | 0.01 |
| 7 | 0.00 | 0.00 | 0.14 | 0.83 | 8.24 | 4.33 | 86.10 | 0.36 | 0.00 |
| 8 | 0.00 | 0.00 | 0.00 | 0.00 | 0.00 | 3.82 | 1.06 | 94.59 | 0.53 |
| 9 | 0.00 | 0.00 | 0.00 | 0.00 | 0.00 | 0.00 | 0.00 | 0.00 | 100 |

Table 5.1 Transition probability (%) matrix for the tide-only Lagrangian particle simulation (indices on the rows are for original compartments and ones on the columns are for receiving compartments, compartment 9 represents the outer box where, by assumption, particles do not leave after entering)

Based on the given transition probability matrix, the Markov first passage time was applied to estimate the flushing efficiency of each compartment:

$$\mu_{ij} = 1 + \sum_{k \neq j} P_{ik} \mu_{kj} \quad (5.3)$$

where $\mu_{ij}$ is the time it takes for a particle in compartment i to move to compartment j for the first time. Thus the flushing time for each compartment could be estimated using the first passage time to the ocean from this compartment. Now besides the 8 compartments within central GSB, the coastal ocean was added

as the 9th compartment, and the flushing time for compartment i is equivalent to first passage time $\mu_{i9}$. The flushing time calculated by this approach is listed in table 5.2. Compartment 1 had the shortest flushing time, but instead of to the ocean, particles in this compartment were most possibly 'flushed' to the lagoon area to the west, so this time could not be considered as a valid flushing time. Compartment 4 had a flush time of 85.5 days which was the result of its direct exchange with the ocean through Fire Island Inlet, and at the same time, its nearby regions (compartment 2 and 3) could connect to the ocean indirectly via compartment 2, thus had relatively short flush time also. Flush time for compartment 5-8 was longer than 120 days because the distance from these regions to the Fire Island Inlet was longer than the excursions of particles and the exchange with Moriches Bay was limited.

| Compartments | 1 | 2 | 3 | 4 | 5 | 6 | 7 | 8 |
|---|---|---|---|---|---|---|---|---|
| Flushing Time | 78.92 | 90.22 | 91.60 | 85.51 | 120.18 | 126.86 | 123.70 | 123.54 |

Table 5.2 Flushing time (first passage time to the ocean) in days

As indicated by Figure 5.6, uncertainties existing in the computing of transition probabilities by taking time-average values. To evaluate the uncertainties, bootstrapping methods were applied and the matrix of transition probability uncertainties is shown as Table 5.3. Generally the uncertainties are much smaller

than the corresponding transition probabilities, thus the stationarity is satisfied in the tide-only case.

| Compartments | 1 | 2 | 3 | 4 | 5 | 6 | 7 | 8 | 9 |
|---|---|---|---|---|---|---|---|---|---|
| 1 | 8.53 | 8.40 | 0.00 | 0.00 | 0.00 | 0.00 | 0.00 | 0.00 | 2.35 |
| 2 | 0.79 | 1.64 | 0.92 | 1.13 | 0.00 | 0.00 | 0.00 | 0.00 | 0.00 |
| 3 | 0.00 | 1.66 | 3.00 | 2.60 | 0.00 | 0.00 | 0.00 | 0.00 | 0.00 |
| 4 | 0.00 | 0.34 | 2.75 | 4.04 | 0.33 | 0.00 | 1.45 | 0.00 | 3.08 |
| 5 | 0.00 | 0.00 | 2.17 | 0.00 | 3.15 | 1.64 | 1.78 | 0.00 | 0.00 |
| 6 | 0.00 | 0.00 | 0.00 | 0.00 | 1.98 | 3.67 | 2.04 | 2.74 | 0.00 |
| 7 | 0.00 | 0.00 | 0.00 | 0.96 | 1.34 | 0.71 | 1.71 | 0.00 | 0.00 |
| 8 | 0.00 | 0.00 | 0.00 | 0.00 | 0.00 | 2.72 | 3.80 | 4.26 | 0.54 |
| 9 | 0.00 | 0.00 | 0.00 | 0.00 | 0.00 | 0.00 | 0.00 | 0.00 | 0.00 |

Table 5.3 Uncertainty (%) matrix of transition probability for the tide-only Lagrangian particle simulation

Transition probabilities over one semidiurnal tidal cycle for the wind-driven Lagrangian particle simulation was calculated by the same approach as the tide-only case, and part of the results are shown in Figure 5.7. Compared to the corresponding transition probabilities in the tide-only case, the magnitudes of transition probabilities increased significantly ranging from 0.03 to 0.1. This indicated the enhanced mixing and connectivity among compartments induced by the wind forcing. Another noticeable difference was the increased variability of the

transition probabilities as functions of time, and the largest standard deviation also reached 0.1 which was comparable to the mean value. Although the magnitudes were different, transition probabilities of 3 to 2, 7 to 4 and 8 to 7 had similar pattern: high during westward winds and low during eastward winds (Figure 5.8). Under westward winds, down-wind currents were westward in shallower water which extended over major part of boundaries between compartment 3 and 2, 7 and 4, as well as 8 and 7, thus the westward transport of particles made these transition probabilities high. When the winds turned to the east, particles were mainly driven to the east and the westward transport vanished, so the transition probabilities dropped to nearly zero. Boundary between compartment 8 and 6 included both middle deep channel and narrower northern shoal area, and currents in the shoal area was weak (Chapter 3). When the winds were westward (tidal cycle 0 - 7), small amount of particles were brought from compartment 8 to 6 by the weak down-wind westward currents; while during eastward wind, stronger up-wind westward currents in the deeper area transported more particles to compartment 6 from 8, so the pattern of transition probability from compartment 8 to 6 was reversed compared with the others.

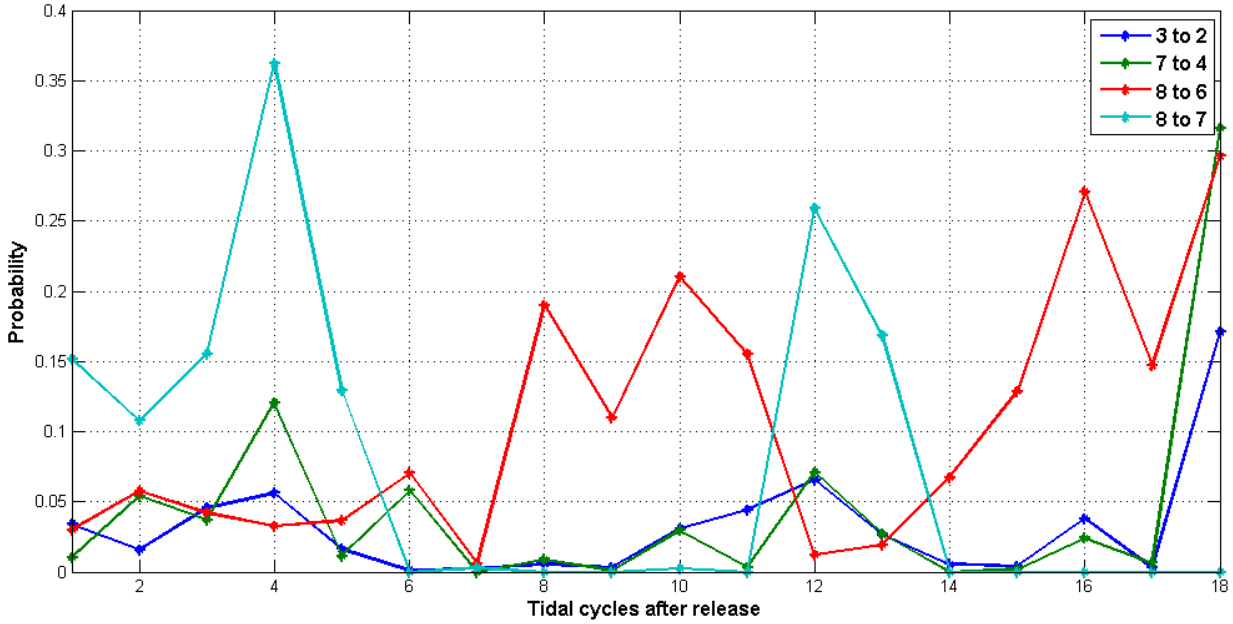


Figure 5.7 Transition probabilities of wind-driven Lagrangian particle simulation

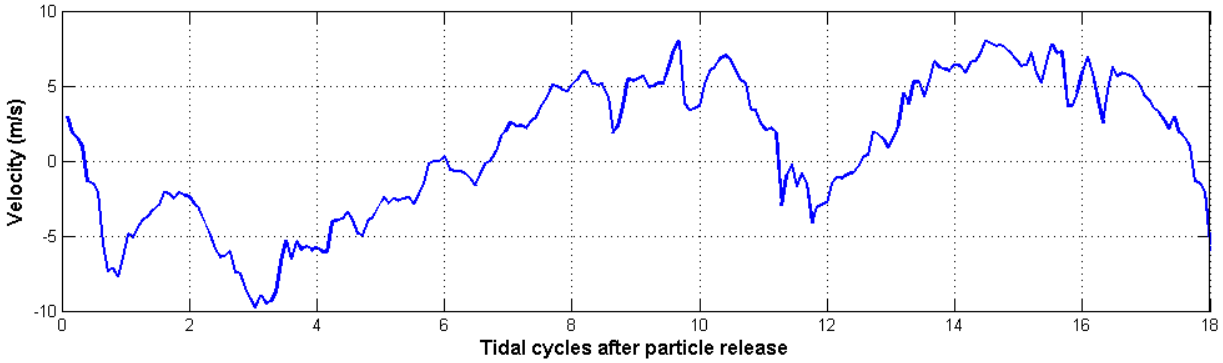


Figure 5.8 component of wind velocity during Lagrangian particle simulation

Under the influence of synoptic wind forcing, a period containing one wind event instead of a semidiurnal tidal period would be a more proper time interval for the discrete Markov Chain. An energy spectrum for the east component of the FVCOM wind forcing is shown in Figure 5.9. Peak of the wind spectrum was at 0.125 cycles per day corresponding to a period of 8 days. This period was used in the calculation of transition probabilities of the wind-driven Lagrangian particle simulation, and the results are shown in Figure 5.10. Mean values of the transition

probabilities were approximately from 0.1 to 0.17, and the standard deviations ranged from 0.01 to 0.07. Compared to the transition probabilities with semidiurnal time interval, the mean values in this case increased, but considering the values in this case were for a much longer period (8 days vs. 0.5 days), the mixing and connectivity were in fact reduced. The main reason for the difference between transition probabilities calculated based on the same particle simulation with different time interval is that: the lateral mixing time scale was comparable to the synoptic period (Chapter 4), so the reversible wind forcing would bring back particles traveled to another compartment but did not get mixed due to the long mixing time. This process occurred in a period of approximately 8 days, and the transition probabilities calculated using a semidiurnal time interval could not interpret this process, thus were not accurate.

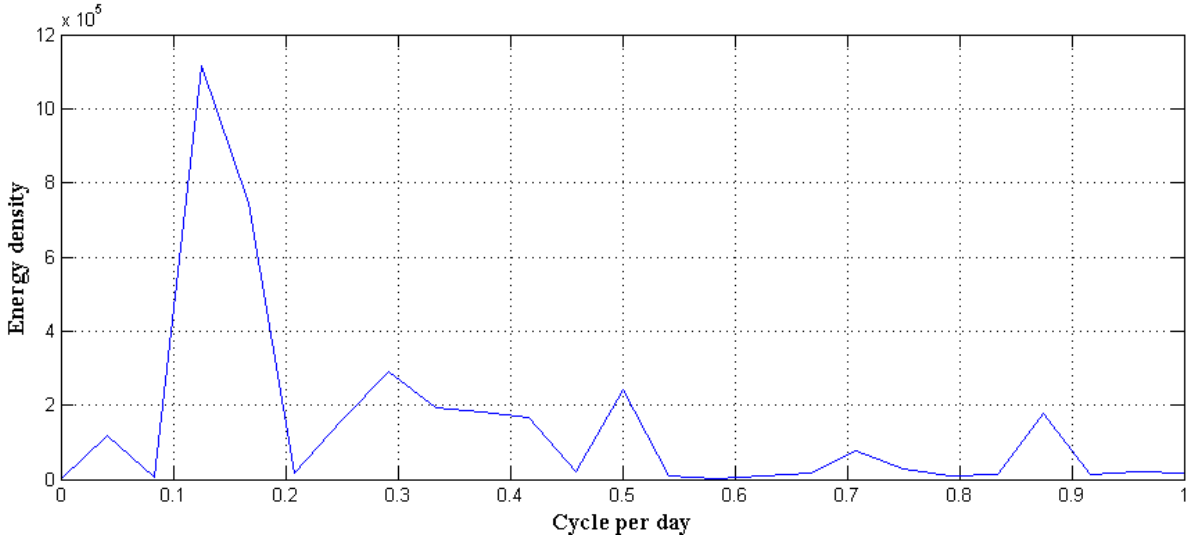


Figure 5.9 Spectrum of the east component of FVCOM wind velocity

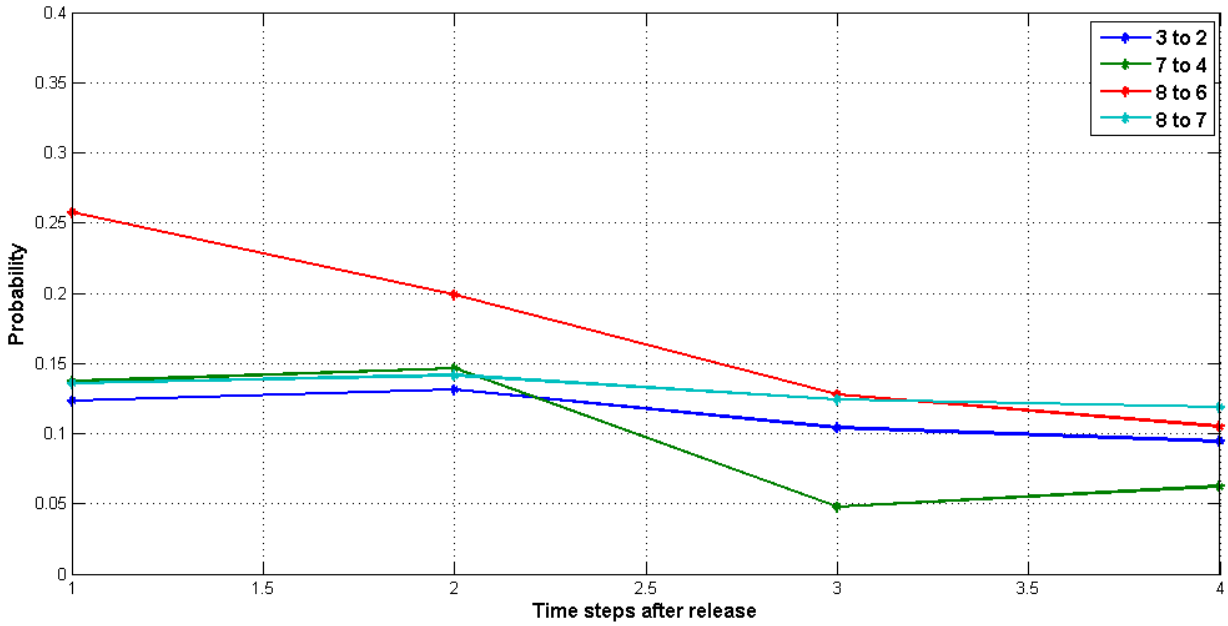


Figure 5.10 Transition probabilities of wind-driven Lagrangian particle simulation (8-day time interval)

## 5.3 Summary

Spatial pattern of residence time (first passage time) in GSB under the influence of realistic wind forcing was computed for both the whole GSB basin (figure 5.2) and for compartments (figure 5.4). First passage time relative to the whole basin boundary was generally long (over 600 hours) except for the regions close to the inlets. Residence time calculated for compartments with much smaller areas had significantly reduced value whose spatial average was 56.7 hours. The spatial pattern within compartments showed the dependence of residence time on the timing of release: the onset of westward wind at the beginning of the release made the residence time generally smaller in the western part of each basin.

Connectivity pattern in GSB was analyzed by first order Markov Chain. Under tide-only condition, transition probabilities over the time interval of a semi-

diurnal tidal period were fairly constant through the simulation, thus the Markov Chain was considered stationary. Based on the transition probability matrix, the most restrictive compartment was #8 within which the particle excursions were typically shorter relative to the compartment size; the least restrictive one was #1due to its smaller longitudinal extension. Flushing time of each compartment was calculated based on the transition probability matrix of Markov Chain, and ranged from 78.92 days (compartment 1) to 126.86 days (compartment 6). When the wind forcing was added to the experiment, magnitude of transition probabilities increased significantly which indicated the enhanced mixing and connectivity produced by the winds. On the other hand, variability of the transition probabilities increased also and the stationarity of Markov Chain was not satisfied with a semi-diurnal tidal period time step. Based on the spectrum analysis of the wind data, 8 days was chosen as the new time interval according to which the transition probabilities were recalculated. The values were relatively constant, but the actual mixing and connectivity were weaker. This reduction in mixing could be explained by the reversed transport of particles within this new, larger time interval since the horizontal mixing time scale was comparable to the synoptic wind period.

## Future Works

In this research, the current structures, especially vertical and lateral current shears under the influence of synoptic period wind forcing are studied. Based on the current structures, theory of shear dispersion is applied to analyze numerically simulated particle patch spreading and is proven valid. Also based on the particle tracking simulations, spatial pattern of residence time and inner lagoon connectivity forced with and without winds are analyzed.

Future works in this research may include:

1. The influence of wind waves on the current structures and further the effective horizontal dispersion in GSB. Wave-current interaction in a coastal lagoon modified wind-driven circulation through the enhanced effective drag coefficient (Signell et. al., 1990), and this influence is more significant in areas with sloping bottom. As a part of the ongoing GSB monitoring system, the surface wave is measured by the ADCP near buoy GSB#1, and this observation will benefit our understanding of wind waves in GSB.

2. Other metrics relating closely to the residence time pattern, inner-lagoon connectivity, and the oscillatory characters of particle movement will be computed and the influence of wind forcing on these metrics will be analyzed, such as

tortuosity which measures the ratio of displacement to the total traveling path length of a particle:

$$D = \sum_{t=2}^{T} \sqrt{(x_i - x_{i-1})^2 + (y_i - y_{i-1})^2}$$

$$L = \sqrt{(x_T - x_1)^2 + (y_T - y_1)^2}$$

$$\tau = 1 - \frac{L}{D}$$

where T, D, L, and $\tau$ are number of total time steps, total traveling path length, location displacement, and tortuosity of a particle separately.

3. For a choked coastal lagoon like GSB, the horizontal dispersion does a better job at explaining the inner lagoon connectivity than the residence time (Chapter 5), and this is because residence time is also dependent on the lagoon-coast exchange processes. In future, the lagoon-coast exchange will be addressed to gain a better understanding of residence time in GSB.

# References

Aikman, Frank III, Lanerolle, Lyon W. J., 2004. Report on the National Ocean Service Workshop on Residence/Flushing Times in Bays and Estuaries.

Bilgili A., Proehl J. A., Lynch D. R., Smith K. W., Swift M. R.. 2005. Estuary/ocean exchange and tidal mixing in a Gulf of Maine Estuary: A Lagrangian modeling study. *Estuarine, Coastal and Shelf Science*, Volume 65, Pages 607-624

Bokuniewicz, H. J., Schubel, J. R., 1991. The Origin and Development of the Great South Bay: A Geological Perspective. *The Great South Bay*, Pages 5-8, State University of New York Press.

Bowden, K. F., 1965. Horizontal mixing in the sea due to a shearing current. *Journal of Fluid Mechanics,* Volume 21, Part 2, Pages 83 - 95

Chen, C., H. Liu, R. C. Beardsley, 2003. An unstructured, finite-volume, three-dimensional, primitive equation ocean model: application to coastal ocean and estuaries. *Journal of Atmospheric and Oceanic Technology*, Volume 20, Pages 159-186

Cowen, R. K., C. B. Paris, A. Srinivasan, 2006. Scaling of connectivity in Marine Populations. *Science*, 311, 522

Csanady, G. T., 1973. Wind-Induced Barotropic Motions in Long Lakes. *Journal of Physical Oceanography,* Volume 3, Pages 429 - 438

Duval, D. I., 2008. Annual Cycle and Synoptic Variability of temperature in Great South Bay, NY. Thesis, School of Marine and Atmospheric Sciences, Stony Brook University

Fischer, H. B., E. J. List, R. C. Y. Kho, J. Imberger, and N. H. Brooks, 1979. *Mixing in Inland and Coastal Waters,* 483 pages, Elsevier, New York.

Geyer, W. R., Chant, R., and Houghton, R., 2008. Tidal and spring-neap variations in horizontal dispersion in a partially mixed estuary. *Journal of Geophysical Research*, Volume 113, C07023

Glorioso, P. and Davies A., 1995. The Influence of Eddy Viscosity Formulation, Bottom Topography, and Wind Wave Effects upon the Circulation of a Shallow Bay. *Journal of Physical Oceanography*. Volume 25, Pages 1243 – 1264.

Jia P. and Li M., 2012. Dynamics of Wind-driven Circulation in a Shallow Lagoon with Strong Horizontal Density Gradient. *Journal of Geophysical Research*. Volume 117, C05013.

Kjerfve, B. and Magill, K., 1989. Geographic and hydrodynamic characteristics of shallow coastal lagoons. *Marine Geology.* 88:187-199

Luettich, R. A., Hench, J. L., Fulcher, C. W., Werner, F. E., Blanton, B. O., and Churchill, J. H., 1999. Barotropic tidal and wind-driven larval transport in the vicinity of a barrier island inlet. *Fisheries Oceanography,* 8, 190-209

Mathieu, P., Deleersnijder, E., Cushman-Roisin, B., Beckers, J., Bolding, K., 2002. The Role of Topography in Small Well-Mixed Bays, with Application to the Lagoon of Mururoa. *Continental Shelf Research,* Volume 22, Pages 1379-1395

Okubo, A., 1968. Some remarks on the importance of the "shear effect" on horizontal diffusion. *Journal of the Oceanographical Society of Japan,* Vol. 24, No. 2, pp. 60-69

Pawlowicz, R., B. Beardsley, and S. Lentz, 2002. Classical tidal harmonic analysis including error estimates in MATLAB using t_tide. *Computers and Geosciences*, 28:927-937

Siegel, D. A., Mitarai, S., Costello, C. J., Gaines, S. D., Kendall, B. E., Warner, R. R., and Winters, K. B., 2008. The stochastic nature of larval connectivity among nearshore marine populations. *Proceedings of the National Academy of Sciences,* Vol. 105: 8974-8979

Signell, R. P., Beardsley, R. C., Graber, H. C., Capotondi, A., 1990. Effect of Wave-Current Interaction on Wind-Driven Circulation in Narrow, Shallow Embayments. *Journal of Geophysical Research,* Volume 95, No. C6, Pages 9671-9678

Swanson, R.L., R.E. Wilson and K. Willig, 2013. A synthesis of loadings, monitoring information, and impairments in the Western Bays. *Report for Battelle Memorial Institute and the New York State Department of State,* School of Marine and Atmospheric Sciences, Stony Brook University, Stony Brook, NY, pp 36.

Taylor, G., 1954. Dispersion of soluble matter in solvent flowing slowly through a tube. *Proceedings of the Royal Society,* 219:186-203

Thompson K. R., Dowd M., Shen Y., Greenberg D. A., 2002. Probabilistic characterization of tidal mixing in a coastal embayment: a Markov Chain approach. *Continental Shelf Research*, Volume 22, Pages 1603-1614

Visser, Andre w., 1997. Using random walk models to simulate the vertical distribution of particles in a turbulent water column. *Marine Ecology Progress Series.* Volume 158, Pages 275 – 281

Wong, K. C., Wilson, R.E. 1984. Observations of Low-Frequency Variability in Great South Bay and Relations to Atmospheric Forcing. *Journal of Physical Oceanography*. Volume 14, Pages 1983-1900.

Winant, C., 2004. Three-Dimensional Wind-Driven Flow in an Elongated, Rotating Basin. *Journal of Physical Oceanography*. Volume 34, Pages 462 – 476.

Wong, K. C, 1993. Numerical simulation of the exchange process within a shallow bar-built estuary. *Estuaries*, Volume 16, No. 2, Pages 335-345.

Wu, J. and Tsanis, I. K., 1995. Numerical study of wind-induced water currents. *Journal of Hydraulic Engineering*, 121:5(388)

Zimmerman, J. T. F. 1986. The tidal whirlpool: A review of horizontal dispersion by tidal and residual currents. *Netherlands Journal of Sea Research* Volume 20, Pages 133-154